DEVELOPMENT OF AN ADAPTIVE CONTACT MODEL FOR ANALYSIS OF WHEEL-RAIL IMPACT LOAD DUE TO WHEEL FLATS

JIAN JUN ZHU

A thesis

in

the Department

of

Mechanical Engineering

Presented in Partial Fulfillment of the Requirements
for the Degree of Master of Applied Science
at Concordia University
Montréal, Québec, Canada

November 2006

Library and
Archives Canada

Published Heritage
Branch

395 Wellington Street
Ottawa ON K1A 0N4
Canada

Bibliothèque et
Archives Canada

Direction du
Patrimoine de l'édition

395, rue Wellington
Ottawa ON K1A 0N4
Canada

Your file Votre référence
ISBN: 978-0-494-28947-1
Our file Notre référence
ISBN: 978-0-494-28947-1

NOTICE:
The author has granted a non-exclusive license allowing Library and Archives Canada to reproduce, publish, archive, preserve, conserve, communicate to the public by telecommunication or on the Internet, loan, distribute and sell theses worldwide, for commercial or non-commercial purposes, in microform, paper, electronic and/or any other formats.

The author retains copyright ownership and moral rights in this thesis. Neither the thesis nor substantial extracts from it may be printed or otherwise reproduced without the author's permission.

AVIS:
L'auteur a accordé une licence non exclusive permettant à la Bibliothèque et Archives Canada de reproduire, publier, archiver, sauvegarder, conserver, transmettre au public par télécommunication ou par l'Internet, prêter, distribuer et vendre des thèses partout dans le monde, à des fins commerciales ou autres, sur support microforme, papier, électronique et/ou autres formats.

L'auteur conserve la propriété du droit d'auteur et des droits moraux qui protège cette thèse. Ni la thèse ni des extraits substantiels de celle-ci ne doivent être imprimés ou autrement reproduits sans son autorisation.

In compliance with the Canadian Privacy Act some supporting forms may have been removed from this thesis.

While these forms may be included in the document page count, their removal does not represent any loss of content from the thesis.

Conformément à la loi canadienne sur la protection de la vie privée, quelques formulaires secondaires ont été enlevés de cette thèse.

Bien que ces formulaires aient inclus dans la pagination, il n'y aura aucun contenu manquant.

Canada

Reproduced with permission of the copyright owner. Further reproduction prohibited without permission.

ABSTRACT

DEVELOPMENT OF AN ADAPTIVE CONTACT MODEL FOR ANALYSIS OF WHEEL-RAIL IMPACT LOAD DUE TO WHEEL FLATS

JIAN JUN ZHU

The discontinuities in surface profiles of railway wheels, commonly known as wheel flats, are known to impose excessive impact loads at the wheel-rail interface. Such impact loads can cause premature fatigue and failure of the vehicle-track system components, and impede the operational safety. The safe and cost-effective operations of railways thus necessitate continuous monitoring and control of impact loads induced by wheel defects. In this dissertation research, an adaptive wheel-rail contact model is developed to predict contact geometry and impact force as a function of flat geometry, speed and normal load. The model employs radial contact springs and could simulate for either single or multiple wheel flats. Unlike the commonly used Hertizan nonlinear models, adaptive model predicts the contact geometry involving either total or partial contact in the presence of a wheel defect in the contact patch. The proposed contact model is integrated to a roll plane model of vehicle and a three-dimensional flexible track model to derive a coupled vehicle-track system model. The vehicle is modeled as a six-DOF lumped mass system including carbody, bolster, sideframe, wheelset, and primary and secondary suspensions. The track system model considers two parallel Timoshenko beams periodically supported by lumped masses representing sleepers. The rail-pad and ballast are also included through linear visco-elastic elements. Central finite difference technique is employed to solve for the coupled partial and ordinary differential equations of motion for the continuous and discrete system models, respectively.

The dynamic response of the wheel-track system is initially investigated under a constant moving load to examine validity of the model and the numerical method. The impact force response of the adaptive contact model in the presence of a single wheel flat revealed reasonably good agreements with available measured data. This agreement was better than that provided by the well-known Hertizan nonlinear point contact model. The results further revealed that discrete sleeper supports act as sources of excitations. The results attained from the parametric study revealed that the normal load, speed and flat size are the primary factors that affect magnitudes of impact forces, while the suspension parameters show only minor effects. Some of the parameters of the track system also revealed important effects on magnitudes of impact force. The coupled vehicle-track system is further analyzed to derive the impact force properties for different wheel flats, operating speeds and loads. The analyses were also performed for single as well as two flats within the same or two opposite wheels of a wheelset. The results suggested that magnitudes of impact forces attributed to the second flat were strongly affected by responses to the preceding flat. The resulting peak impact force may be either higher or lower than that caused by a single flat, depending upon flats geometry, relative coordinates of the flats and operating speed. The results further suggest that the length of a flat, which is regarded as the removal criteria by AAR and Transport Canada, is not sufficient for cases involving either single or multiple flats.

ACKNOWLEDGEMENTS

The author would like to thank his co-supervisors Dr. A. K. W. Ahmed and Dr. S. Rakheja for providing the opportunity for this research, for their continued intellectual guidance, encouragement and financial support throughout the course of this research. Special thanks are due to CN for initiating the research topic of this dissertation.

The author also wishes to thank members of the faculty and staff of CONCAVE (Concordia Center for Advanced Vehicle Engineering) Research Centre, Department of Mechanical and Industrial Engineering, Concordia University for their time and assistance during the course of this work. The author is thankful to all the friends and colleagues for their help and valuable discussion.

The author would like to express his thanks for the patience, sacrifice, encouragement and support to his wife. Sincere thanks also go to the author's father and other family member in China for their preserving support. Finally the author wishes to mention his son whose innocent demands made this work somewhat tougher, but who provided a lot of enjoyment during the completion of the thesis.

TABLE OF CONTENTS

CHAPTER 1

INTRODUCTION AND LITERATURE REVIEW

CHAPTER 2

AN ADAPTIVE WHEEL-RAIL CONTACT MODEL

CHAPTER 3

DEVELOPMENT OF THE VEHICLE-TRACK SYSTEM MODEL AND NUMERICAL METHOD

CHAPTER 4

MODEL VALIDATION AND RESPONSE OF VEHICLE-TRACK SYSTEM

CHAPTER 5

IMPACT LOAD DUE TO SINGLE WHEEL FLAT

CHAPTER 6

IMPACT LOAD DUE TO MULTIPLE WHEEL FLATS

CHAPTER 7

CONCLUSIONS AND RECOMMENDATIONS

LIST OF FIGURES

LIST OF TABLES

NOMENCLATURE

A	Cross-sectional area of the rail (m^2)
a	Sleeper span (m)
C	Damping coefficient of vehicle suspension in simple lumped mass vehicle-track model (N.s/m)
C_1	Damping coefficient of primary vehicle suspension (N.s/m)
C_2	Damping coefficient of secondary vehicle suspension (N.s/m)
C_b	Damping coefficient of ballast (N.s/m)
C_p	Damping coefficient of rail-pad (N.s/m)
C_H	Hertizan contact coefficient ($N/m^{3/2}$)
D_f	Depth of flat (mm)
E	Elastic modulus of rail (GN/m^2)
F	Radial contact force (N)
F_i	Support force of ith sleeper (N)
F_n	Normal component of radial contact force (N)
f	Variation of wheel radius (m)
G	Shear modulus of the rail material (GN/m^2)
h	Distance between the wheel center and the contact patch center (m)
I	Second moment of area of rail (m^4)
J_b	Mass moment of inertia of bolster ($kg.m^2$)
J_w	Mass moment of inertia of wheelset ($kg.m^2$)

j	Sequence number of time step
K	stiffness of vehicle suspension in simple lumped mass vehicle-track model (N/m)
K_1	Stiffness of primary vehicle suspension (N/m)
K_2	Stiffness of secondary vehicle suspension (N/m)
K_b	Stiffness of ballast (N/m)
K_p	Stiffness of rail-pad (N/m)
K_H	Linear Hertizan contact spring stiffness (N/m)
K_w	Radial contact spring stiffness (N/m.radian)
K	shear coefficient of rail
k	Sequence number of CFDM grid of rail or position step
L	Total length of track considered in track model
L_b	Distance between left and right secondary suspension in bogie (m)
L_s	Lateral distance between two rail supports or sleeper length (m)
L_w	Distance between left and right wheel bearing center (m)
l_e	Length of contact patch (m)
l_f	Length of flat (mm)
$\mathrm{m_b}$	Mass of bolster (kg)
$\mathrm{m_{sf}}$	Mass of sideframe (kg)
$\mathrm{m_s}$	Mass of sleeper (kg)
$\mathrm{m_t}$	Mass of track in simple lumped mass vehicle-track model (kg)
$\mathrm{m_w}$	Mass of wheelset (kg)
$\overline{m}$	Mass of rail of unit length (kg/m)

n	Number of sleeper-spans considered in track model; number of grids within one sleeper-span
N	Number of sleeper
N_1, N_2	Shape function used to interpolate the contact force and displacement of the position between the grid points
P, P_c, P_l, P_r	Wheel-rail contact force, subscript represents left or right side(N)
P_a	Longitudinal force applied on rail (N)
P_o	Static wheel-rail contact force (N)
R_i	Instantaneous radius of the wheel at the position α_i (m)
R_w	Nominal wheel radius (m)
r	Radius of gyration of the rail cross-section (m)
t	Time (s)
Δt	Time step
Δu	Overlap between wheel and rail (m)
V	Vehicle speed (km/h)
W	Carbody weight (kg)
X_w	Coordinate of contact point along the rail originate from left fixed end (m)
x	Horizontal coordinate of an arbitrary point within the flat curve (m); coordinate used to define the point on rail (m)
Δx	Grid or position step of rail
y	Distance from the k^{th} grid point to the contact point between k^{th} and $(k+1)^{th}$ grid point
z_b	Displacement of bolster (m)
z_{is}	Displacement of ith sleeper (m)

z_r, z_R	Displacement of rail at contact point (m)
z_{sf}, z_{sfl}, z_{sfr},	Displacement of sideframe, subscript represents left or right side (m)
z_w,	Displacement of wheelset center (m)
z_{wl}, z_{wr}	Displacement of wheel center, subscript represents left or right side (m)
α, α_i	Angle of an arbitrary point within contact zone (°)
α_f, α_r	Front and rear wheel-rail contact angle (°)
α_w	Wheel-rail contact patch angle for perfect wheel profile(°)
β	Angle between the reference line and wheel radius (°)
β_o	Angle between the reference line and wheel flat center line (°)
φ	Half op the angle of the total flat length (°)
φ_b	Roll displacement of bolster (radian)
φ_s	Roll displacement of sleeper (radian)
φ_w	Roll displacement of wheelset (radian)
γ	Angle of wheel rotation (°)
θ	Rotational displacement of Timoshenko beam (radian)
ω	Angular speed of wheel rotation (radian/s)
ε	Tolerance of iteration in finding contact patch
δ_c	Wheel-rail contact deformation at the contact patch center or overlap (m)
δ_i	Elemental radial deflection of the radial spring in wheel-rail contact zone (m)
δ_o	Static wheel-rail overlap (m)

CHAPTER 1

INTRODUCTION AND LITERATURE REVIEW

1.1 INTRODUCTION

The dynamic response and operational safety performances of a railway vehicle are strongly dependent upon the vertical dynamic wheel-rail interactions. Such interactions, associated with the rolling contact, are known to be highly nonlinear due to flexibility of the contacting bodies and nonlinear stiffness property attributed to geometry effects, referred to as the Hertzian contact stiffness. The complexity of the vertical dynamic interaction of rolling contact increases manifolds, whenever a small scale unevenness of the wheel or rail surfaces is present. Such surface defects tend to yield high frequency interaction forces between the wheel and the rail, which further depend upon many factors, such as the vehicle speed, axle load and defect size [1]. Heavy haul and high speed railway trains commonly exhibit various wheel rail interface defects, caused by material fatigue, block brakes, locked brakes, etc. Wheel flats are commonly observed wheel rim surface defects, which may be typically 50 mm long or exceed 100 mm [2].

The wheel defects generally form a discontinuity in the wheel-rail rolling contact patch and cause high magnitude impact forces. The magnitudes of the impact forces tend to be considerably large when high axle loads are involved as in the case of heavy haul railways or for high speed trains. The large impact loads between the wheel and the rail may cause damages to the track and vehicle structures, leading unscheduled service interruption or even derailment in extreme cases, which could pose serious safety risks and operational cost to the railway industry.

The operational safety of the railway can be enhanced through timely detection of wheel rail defects, and through better understanding of the initiation and propagation of defects. Dynamic response analyses of the coupled vehicle-track system to the excitations arising from irregularities and defects, such as rail joints and surface defects, can provide considerable insight into the magnitudes of resulting impact loads and their adverse effects. A study of dynamic wheel-rail interaction necessitates accurate characterization of the contact between the wheel and the rail, which is known to be quite complex, particularly when the interface defects are present [3, 4]. Moreover, the flexibility of the infinitely long track system, and strong coupling between the vehicle and the track, require consideration of a detailed track model with dynamic properties of essential components of the coupled system. Developments in reliable analytical tools for analysis of the coupled vehicle-track system can help predict impact loads induced by wheel rail defects, and thereby permit for timely detection and removal of defective elements. Studies conducted during the past half century have evolved into various analytical models for predicting impact loads [4].

A number of monitoring systems have also been commercially developed for detecting the wheel rail defects [5, 6]. Reported studies have employed a wide range of linear and nonlinear rolling contact models, and vehicle component models. Many studies, however, have suggested that the reported methodologies cannot predict wheel-rail impact load induced by many types of wheel rail defects with sufficient accuracy in the entire speed range [7]. Furthermore, it has been suggested that the monitoring systems do not permit for detection of the size of the defects [8]. The vast majority of the analytical models have employed Hertzian nonlinear point contact theory, which is often used to describe contact behavior of two cylinders, to simulate wheel-rail vertical interactions. A few studies have shown that this theory yields an underestimation of impact forces at low speeds, and an overestimation of impact forces at high speeds [2, 9].

This dissertation research concerns with development of a nonlinear and adaptive contact model to attain a better prediction of the impact forces caused by wheel flats. An analytical model of the coupled vehicle-track system is developed by integrating a roll plane model of the vehicle system and a three-dimensional model of the flexible track system. Central finite difference method (CFDM) is employed to analyze the vehicle track vertical interactions. The proposed CFDM can easily adapt for varying track lengths (number of sleeper-spans), and number of elements between two consecutive sleepers. Dynamic responses of the coupled vehicle-track system are analyzed at the left and right track-wheel interfaces in the presence of either single or multiple wheel flats. The factors affecting wheel rail impact loads due to single flat are thoroughly investigated. The impact loads due to two flats on a single as well as two wheels of a wheelset are evaluated and compared with those derived from a single flat.

1.2 REVIEW OF RELEVANT LITERATURE

The analyses of dynamic wheel-rail interactions necessitate appropriate considerations of dynamic characteristics of vehicle components, rolling contact, interface defects, dynamic deformation of the flexible rail and supporting components, coupled vehicle-track system dynamics, etc. The relevant reported studies are thus reviewed and discussed in the following sections to build the essential background and to formulate the scope of this dissertation research.

1.2.1 Wheel Defects

Railway wheel defects are generally attributed to imperfections caused during operation, manufacturing, alignment and fixation. The wheel defects have been described by many types such as flat, shelling, spalling, shattering, corrugation, roughness, eccentricity, etc. These defects are generally referred to as Out-Of-Round (OOR) [10]. The causes and consequences of OOR, experimental detection of wheel-rail impact loads due to OORs, mathematical models to predict the wheel rail impact loads due to OORs and criteria for removal of OOR wheels, etc, have been thoroughly discussed in a comprehensive review presented by Nielsen and Johansson [10]. This study concluded that despite considerable research effect on the causes and consequence of OOR, far more effects are desirable to enhance our understanding of the OOR relevant problems, such as estimation of cost associated with vehicle and track maintenance related to common OORs, development of improved simulation models of the vehicle-track system, improvement of wheel removal criteria for common OORs, and investigation of the influence of vehicle track properties on the development of OOR and induced impact loads. Daniel and Lonsdale [31] analyzed the data compiled by the AAR (Association of American Railroads) on the wheelset removal for 1999 and concluded that the rim shattering, slid flat, shelling and tread build-up are most common wheel defects in the North American railroads. Apart from these, the wheel cracks are also a commonly encountered type of wheel defects primarily attributed to manufacturing flaws. All these defects contribute to the development of high magnitude forces at the wheel-rail interface.

The industry generally follows a standard practice to remove the defective wheels on basis of monitoring and detective measurements that may depend upon the type of defects. Among the various wheel defects, the wheel flats are commonly encountered and widely studied [12]. This type of defect dominates the dynamic wheel-rail interactions and remains the primary concern of the industry. Such defects generally arise when the brake are applied to the wheel. The application of brakes may cause the wheel to lock-up and slide along the rail without rolling. This sliding usually causes severe wear of the wheel tread surface in contact with the rail, leading to the formation of a flat spot called the "wheel flat." It has been reported that wheel flats of 50 mm long are typically encountered and may exceed 100 mm long [2]. AAR recommends that a wheel with a flat exceeding 50.8 mm(2 inches) or over in length or two or more adjoining spots each spanning 38.1mm (1.5 inch) or over in length should be replaced from service to ensure safe and economic operation of the railroad [13].

Wheel shelling is a term normally used to describe the loss of flakes of material from the wheel tread as a result of initiation and growth of fatigue cracks from an internal defect in the wheel rim [14]. Guagliano and Vergani [14] reported that shelling is caused by contact fatigue, which causes the micro-cracks originated by an internal pre-existing defect to propagate tread until the crack approaches the free surface. A section of the wheel tread may separate from the rim, making the wheel unserviceable. Excessive drag braking produces heat in the wheel that can cause its steel to soften and thereby becoming more prone to fatigue [10]. In North American railway service, wheel shelling is also called shattering [11]. The AAR-CAR data suggests that in 1999, the shattered rims accounted for 0.059% of all the wheel removals [11].

Wheel spalling is another type of defect that has been associated with the rolling contact fatigue [10}. The thermal stress developed in the wheel may cause wheel surface cracks and loss of material flakes from the wheel tread. Such defects thus appear as some small spots within localized regions on the wheel tread. The thermal cracks may also arise due to formation of the hard and brittle martensite that is developed owing to heating and rapid cooling of the wheel tread during and after braking [10]. Such defects are also referred to as shelling by AAR-CAR [11].

Another type of defect related to the wheel tread surface is corrugation that is described by small amplitude surface undulations with a broad spectrum of wavelength [15]. It can occur on the surface of both the wheel and the rail. The surface corrugation phenomenon has been observed and studied for over 100 years. The mechanisms leading to its formation and development, however, have not been completely quantified. Sato *et al.* [16] investigated the corrugation phenomena and concluded that the problem of surface corrugation becomes more serious under high speed and axle load. Different studies have attributed the surface corrugation defects to different sources. Liu et al. [17] suggested that non-uniform wear could cause surface corrugations, while Morys [18] concluded that small derivation in wheel radius caused within the manufacturing or maintenance tolerance, yields considerable variations in the normal force developed at the wheel-rail interface, which may contribute to surface corrugations. Another study by Petersson [19] suggested corrugations are prone to appear on block-braked wheels. Studies by Ishida et al. [20] concluded that lateral creepage forces, rail joints and the higher proportions of lateral force in relation to the vertical force may contribute to formations. This type of defect has attracted relatively more attention in recent years.

Apart from the above-stated fatigue, wear and brake induced defects, the wheel surface roughness [53], characterized by micro peaks and troughs also contributes to high magnitude and high frequency normal contact force. The micro-roughness may at times exhibit a periodic pattern [21]. The circumferential wavelength of wheel roughness is in the order of magnitude of 1mm, while the roughness amplitude is of the order of 10 μm [10].

Misalignments in the fixation of the wheel during profiling or re-profiling can also lead to wheel eccentricity, which can cause high magnitude of vertical contact force. The high frequency and high magnitude wheel-rail contact forces caused by wheel defects in general contribute to the material fatigue and initiation of fatigue cracks [54]. Dynamic rolling contact can aggravate the contact fatigue and enlarge the cracks. Galliano and Vergani [14] suggested that wheel cracks occurring underneath the tread surface always lead to wheel shelling, while the surface cracks can result in spalling.

The wheel and rail defects contribute considerably to development of abnormal vertical contact force at the rolling contact interface. The magnitude of such force strongly depends on the nature of defects. The discontinuous nature of the wheel flats induces high magnitude impact loads at the wheel-rail contact surface and thereby aggravates further fatigue of the wheel and rail, and other components of the coupled vehicle-track system. Since this dissertation research concerns the wheel flat type of defects, the reported studies on such defect are thoroughly reviewed and discussed in the following subsections.

1.2.2. Wheel Flats

Wheel flats are very common type of wheel defects, which are primarily caused by the braking of wheel when the applied braking force exceeds that the available wheel rail friction can support. Such defects are thus known to initiate and propagate when the brakes are poorly adjusted, frozen or defective [10]. Moreover, such defects have been attributed to wheel rail surface properties when the surface friction in a localized region becomes quite low [10]. Contaminations on the rail, such as leaves, grease, frost and snow, may aggravate the problem. Snyder and Stone [22] investigated the formation and growth mechanisms associated with wheel flats and concluded that the formation of wheel flats can occur with or without the formation of tread defects. Jergeus et al. [23] performed experiments on a full-scale railway to study the flat formation conditions under different wheel loads, train speeds, sliding durations and coefficients of friction. The study concluded that a wheel flat occurs rapidly at the beginning of sliding, while further sliding tends to increase the flat size at a slower rate.

Owing to the formation mechanism, it is quite common for a single wheel to develop more than one flats. Moreover, multiple wheels of a vehicle may exhibit single or multiple flats. Application of a large magnitude brake force that causes the lock-up of either one or more wheels on a single car, may also contribute to formation of flats on the other wheels of the same car. The lack of adequate friction within localized zones also causes wheel lock-up and intermittent sliding and rolling of the wheels, which can contribute to the formation of more than one flats on one wheel [10].

Wheel flats, whether single or multiple, induce high magnitude impact force at the wheel-rail interface due to discontinuities in the rolling contact. Such forces not only aggravate fatigue of the wheels, rails and other components, but may also lead to bearing failure. In extreme circumstances, the dynamic interaction between wheel and rail may lead to derailment [1]. A vast number of studies have investigated the influence of wheel flats on the dynamic responses of the coupled vehicle-track system [1, 12, 24]. These studies have invariably concluded that the presence of a wheel flat in the rolling contact affects the railroad performance in a highly adverse manner.

In an attempt to control the adverse effects of such defects and ensure smooth and safe operation of the railroads, the railway organizations have proposed threshold values of the wheel flats [13, 25, 26]. A wheel with a flat exceeding the threshold value must be replaced from service. The threshold values have been normally proposed on the basis of flat size. Alternatively, railroads in North America and Western Europe have employed track-side impact force detectors for monitoring impact loads caused by defective wheelsets. The impulsive impact force induced by a wheel flat is thus considered as an important determinant value of a defect.

The threshold values for the wheel flats can be classified in three categories on the basis of the measure used: (i) length of the wheel flat; (ii) depth of the wheel flat; and (iii) length of the wheel flat coupled with the induced impact force. Transport Canada safety regulations [25] require that a wheel with a slid flat spot exceeding 63.5 mm in length can not be placed or continue to be in service. The regulations also stipulate that a wheel with two adjoining flat spots, each exceeding 50.8 mm in length, must also be removed from service. According to AAR Rule 41-Section A [13], a wheel should be replaced if the peak impact force approaches 400kN (90,000 pounds). Cars cannot be placed or continue to be in service if a wheel exhibits: (i) a slid flat approaching or exceeding 50.8mm in length; or (ii) two or more adjoining spots, each approaching or exceeding 38.1mm in length. The railway organizations in China [26], Sweden [6], United Kingdom [27], Australia [28] and other countries have also established similar threshold values for wheel flats.

The removal criteria for defective wheels are based on the damage potential of the wheel flat, mostly the magnitude of the impulsive impact force induced by the flat [13]. It is generally agreed that the impact force developed at wheel-rail interface is most significantly affected by the flat size, and that the wheel flat length and depth are correlated through the wheel radius for a fresh wheel flat [1]. However, the results attained from parametric studies suggested that the influence of flat depth on the magnitude of the impact load is greater than that of the flat length [1, 9]. The wheel loads, train speed and the elastic properties of track also influence the magnitudes of the impact force [1].

Owing to the important influences of various design and operating factors on the flat induced impact forces, a number of studies have expressed concerns on the validity of the proposed /standardized threshold values for the removal criteria [10, 30]. A vast number of studies have thus investigated the nature of the wheel flat induced impact forces using analytical models of varying complexities [1, 24, 29]. The vast majority of these studies consider only a single flat. A few recent studies have also investigated effects of a wheel flat on the force response of the neighboring wheel [12]. These studies have invariably shown that the magnitudes of impact forces are influenced by many design and operating factors apart from the flat size, such as speed, wheel load, vehicle suspension properties and track flexibility. Although the wheel removal criteria based upon the flat size and impact force may be acceptable when a single flat is present, the dynamic interactions due to several flats have not been thoroughly investigated.

In order to investigate the impact loads due to wheel flat, different wheel flat models have been developed to describe the geometric profiles of the wheel flats. Considering that a wheel flat is initiated by wheel sliding on the rail, the initial flat is thus modeled as a chord, referred to as "fresh flat" or "chord flat" model [1, 2, 12, 31, 32], as shown in Figure 1.1. The variation in wheel radius (*f*) due to a chord flat can be easily obtained from the geometry. Makoto and Takumi [31] evaluated the induced impact forces due to different models and concluded that the chord flat model always overestimates the magnitude of wheel-rail impact load.

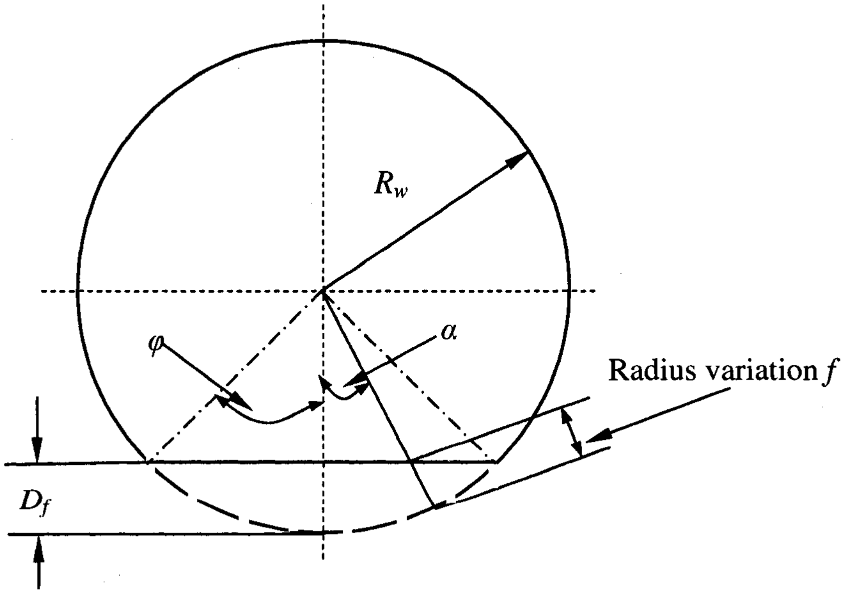

Figure 1.1: A chord model of the wheel flat

For a chord flat model, the variation in the wheel radius due to a flat can be described by the following equation:

$$f = R_w - \frac{R_w - D_f}{\cos\alpha}, \qquad -\varphi < \alpha \leq \varphi \tag{1.1}$$

Where R_w is the nominal wheel radius, D_f is the flat depth, α is the angle of an arbitrary point within the flat zone or the cord and φ defines the angle of the chord as shown in Figure 1.1.

The chord model may accurately describe a fresh flat. The ends of a fresh flat, however, quickly assume a rounded profile. Rounded flat or haversine flat is thus used to describe the geometry, as shown in Figure 1.2. The model employs a cosine function to describe the variations in the wheel radius due to the flat [1, 2, 12, 32, 33, 34], such that:

$$f = 0.5D_f\left[1 - \cos\left(\frac{2\pi x}{l_f}\right)\right] \tag{1.2}$$

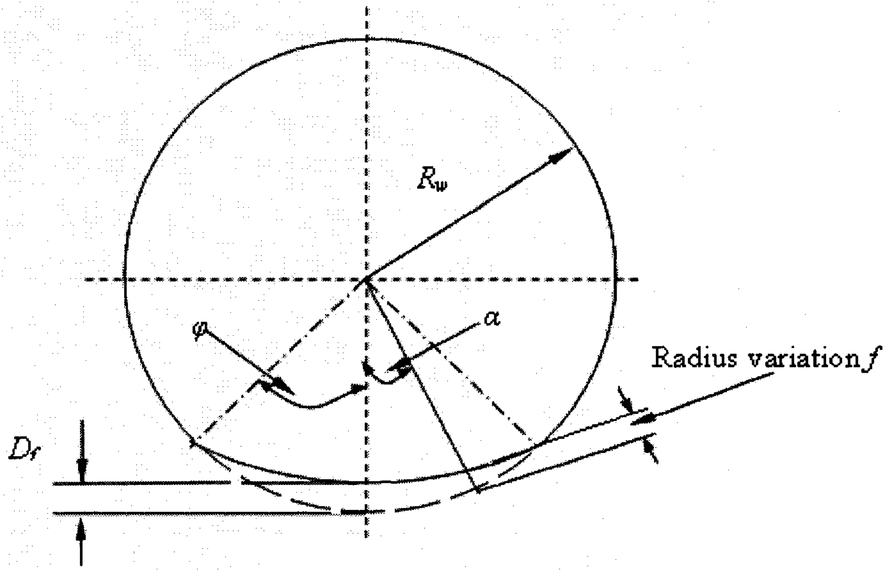

Figure 1.2: A haversine model of the wheel flat

Where x is the horizontal coordinate of an arbitrary point within the flat curve and l_f is the flat length.

A haversine flat model closely describes the flat geometry and the resulting impact force responses generally show good agreements with the experimental data [1, 31]. However, the real shape of wheel flat is neither a purely chord shape nor a purely haversine shape. A flat is generally a combination of a cosine shape at the two ends and a chord shape in the middle section. Makoto and Takumi [31] developed a combined flat model including a chord and rounded sections to analyze the dynamic wheel rail interactions. The model however, did not offer notable advantages over the haversine flat model. Their results from combined flat model revealed reasonably good agreement with the data in terms of the magnitudes of impact forces, while considerable difference were observed in the waveform of the contact force.

1.2.3 Modeling and Simulation Methods

The studies on the effects of wheel flats have been mostly performed through analytical modeling and simulation techniques. Owing to the challenges associated with the measurement systems, only a few studies have attempted to measure the impact force response due to wheel flats [9, 35]. A number of models have been developed in the past few decades for analyses of wheel rail vertical interactions. These simulation models focus on either the wheel-rail interactions alone or the coupled vehicle-track system. Ahmed *et al.* [36] has presented a thorough review of the reported models. While the reported models differ most significantly in modeling assumption, complexities and component properties, the coupled vehicle-track system model generally employ a common structure. Such models generally consist of four major components, as shown in Figure 1.3. These include: (i) a vehicle model; (ii) a track model; (iii) a wheel rail contact model; and (iv) a wheel flat/defect model, which has been reviewed and discussed in the previous section. The geometric irregularities at the wheel-rail interface, i.e., wheel flats, serve as the input to the contact model, while the dynamic displacements of the wheel and the rail are taken as generalized outputs. The dynamic displacement responses are subsequently related to dynamic contact forces at the wheel-rail interface.

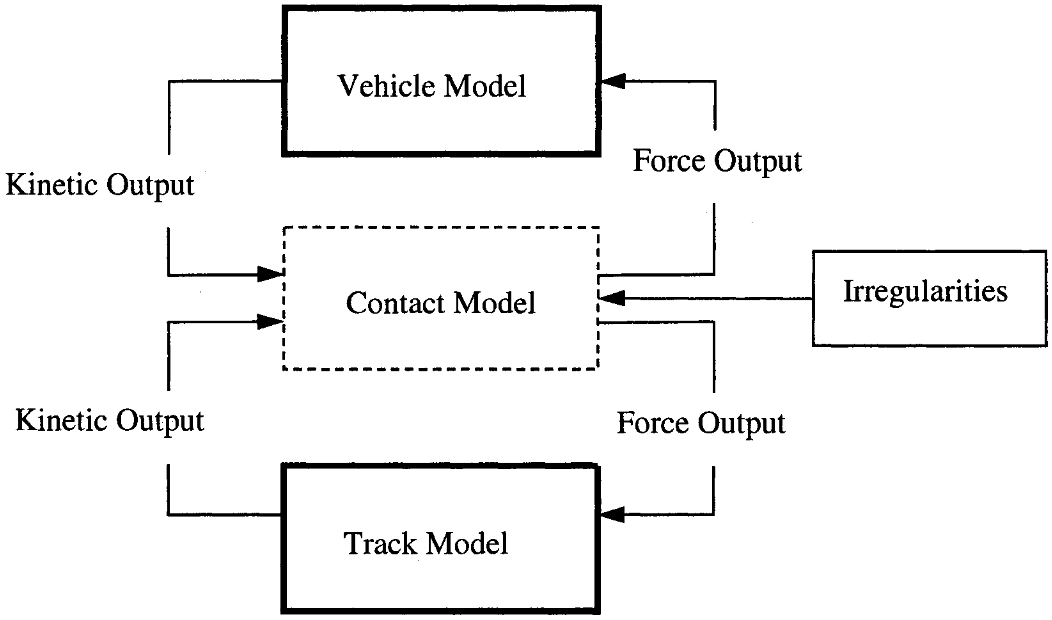

Figure 1.3: A generalized coupled vehicle-track system modeling scheme

The vast majority of the reported coupled vehicle-track models are plane models, derived upon consideration a single rail and assuming symmetry of the coupled system [2, 9, 18, 37, 38]. Vertical and pitch dynamic responses are thus evaluated to study the effects of wheel flats on the contact force developed at the contact of the defective and adjacent wheels. The contributions due to the roll motions of the wheelsets and the bolster (car body) are assumed to be small. The effects of the wheel flats on the opposite wheel and track are thus not evaluated. A few studies have developed three-dimensional models of the vehicle-track system incorporating the two rails and the roll dynamics to investigate the interactions for the asymmetric vehicle track systems [32, 39, 34, 40]. The reported models have been developed using a wide range of simplifying assumptions, contact models and component properties. The sub-models of the coupled system are described in following sections.

1.2.4 Vehicle Model

The vehicle models integrate various components of the vehicle, namely, the wheelset, bogie, the car body and the primary and secondary suspensions. The natural frequency of the car body is generally considered to be significantly lower than that of the dynamic contact force due to the wheel OOR defects, such as flat, spalling, shelling and corrugation [15, 37]. The contributions due to the dynamics of the components of the vehicle located above the primary suspensions are thus considered to be small [15]. Relatively simple models consisting of unsprung mass and primary suspensions alone have thus been widely adopted to study the effects of wheel OOR defects [2, 9, 31]. The reported models also range from simple one dimensional (1-D) model representations to highly complex three-dimensional (3-D) formulations. While the 1- and 2-D models are considered to be adequate for analyses of the vertical responses of the symmetric vehicle-track system due to wheel rail defects, the 3-D models permit for analyses of the non-uniform wear and asymmetric response of the vehicle-track system in vertical as well as lateral direction. These models, grouped under 1-, 2-, 3-D models, are briefly described below.

One-Dimensional Models

The simplest vehicle model is a single DOF one-dimensional model which employs rigid mass representation of the unsprung mass (wheelset and accessories) [9, 33, 41, 42]. The vehicle components above the wheelset are modeled using two different approaches. Nielsen et al. [37, 41] represented these components by a dead weight *W*, while neglecting the contributions due to suspension deflections and properties, as shown in Figure 1.4. The model, however, incorporated a contact spring between the unsprung mass and the track. This simple model has been applied in a number of published studies concerned with dynamic wheel-rail interactions [9, 37, 43], and is considered is insufficient for evaluating the effects of vehicle suspensions on the impact loads caused by a wheel flat. Makoto and Takumi [31] modified this model by introducing the vehicle suspension, as shown in Figure 1.5, to include the effects of suspension deflection and properties. The components above the wheelset, however, were regarded as a dead weight exerted on the wheelset as in the Nielson's model.

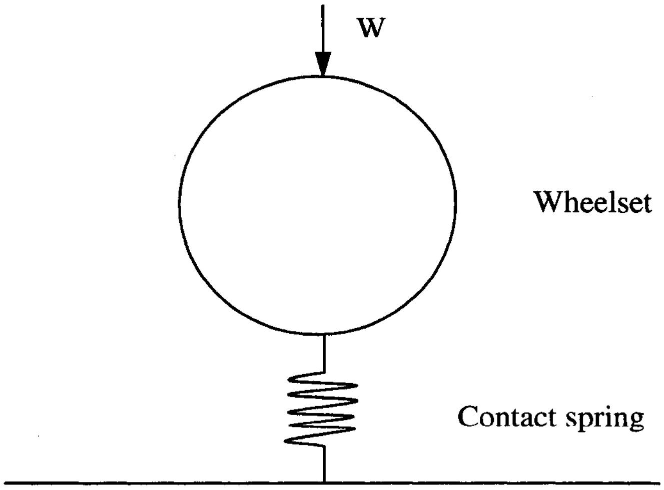

Figure 1.4: A single DOF one-dimensional model of the vehicle proposed by Nielson et al. [37, 41]

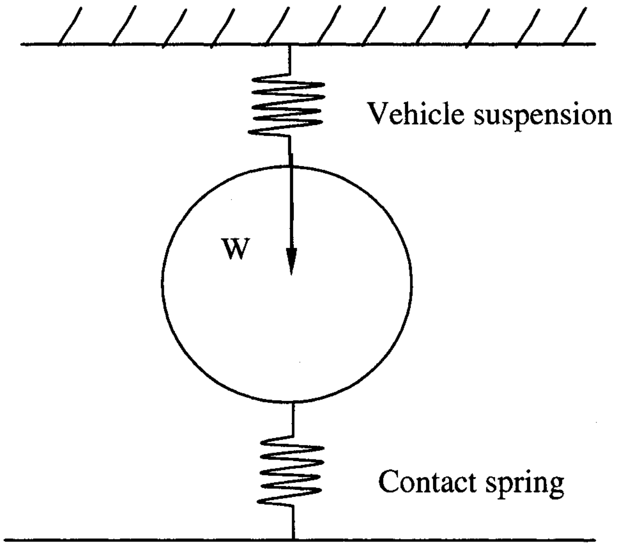

Figure 1.5: A single DOF one-dimensional vehicle model with suspension proposed by Makoto and Takumi [31]

Both the models are considered to be sufficient for investigating the influence of wheel rail irregularities on the track system. The contributions due to resonant response of the vehicle system, however, can not be considered. Moreover, such models do not permit for analyses of the dynamic forces exerted on the vehicle components due to the wheel rail interactions. Furthermore, the contribution due to pitch and roll responses of the vehicle, and the defect on the response of other wheels could not be evaluated.

Jin et al. [38] proposed a two-DOF one-dimensional vehicle model as shown in Figure 1.6. This model employs a single wheelset, the suspension and a lumped sprung mass representative of the components above the wheelset. The model considers linear stiffness (K_c) and damping (C_c) properties of the suspension. The model permitted for analyzing the effect of carbody and suspension on the wheel-rail impact loads, while the pitch and roll dynamic responses could not be evaluated. Moreover, the dynamic forces response between the vehicle components, e.g., bearing and side frame, could not be obtained.

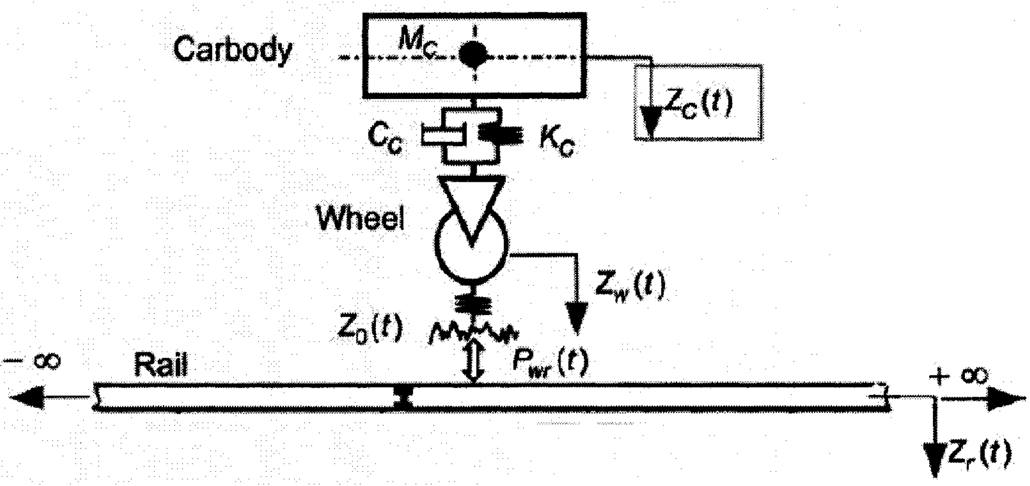

Figure 1.6: Two-DOF one dimensional vehicle model with carbody and suspension [38]

Two-Dimensional Models

Two-dimensional or in-plane models have been most widely formulated and applied for studies on wheel-rail interactions. The vast majority of these models have been developed to incorporate the pitch-plane dynamics [1, 24, 35, 37], while little efforts have been made to study the contributions due to roll dynamics of the railroad. A roll-plane model would also permit for the study of effect of defects within the opposite wheels. Nielsen and Igeland [37] developed a four-DOF pitch-plane model of the vehicle including vertical motions of two wheelsets, vertical and pitch motions of the side frame (bogie), as shown in Figure 1.7. The carbody was represented by a force ($M_o g$) applied on the bogie, while each wheelset was represented by an unsprung mass. Cai [24] applied this model to simulate the vehicle-track interactions in the presence of wheel defects. This model was considered to be sufficient for the study of dynamic responses of the wheelsets and the bogie. The dynamic responses of bolster (or carbody), however, can not be investigated, while the important contributions of the secondary suspension are not considered.

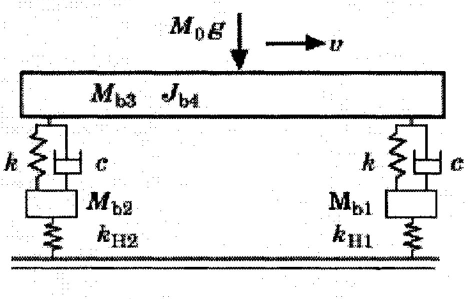

Figure 1.7: Four-DOF two-dimensional vehicle model [24, 37]

A typical two-dimensional vehicle model is also been formulated to the vehicle with five-DOF [1]. This model consists of half bogie and a quarter of the car body weight. The bogie includes half the bolster, one sideframe and two half wheelsets, as shown in Figure 1.8. The DOF include vertical and pitch motions of the sideframe; and vertical motions of the bolster and two wheelsets. Such a model would be sufficient to study the vertical and pitch dynamic responses of the vehicle and dynamic coupling between the two adjacent wheels in the presence of wheel rail defects. The coupling between the leading and trailing bogies, however, could not be examined, while the contributions due to roll dynamic response of the wheelsets and bolster (carbody) are ignored.

Zhai [35] extended the 5-DOF pitch plane model to a 10-DOF pitch plane model of the vehicle by including the entire carbody and two bogies, as shown in Figure 1.9, to study the dynamic loads on the tracks due to turnout, rail joint, wheel flats and bridge-subgrade transition sections. The model takes the pitch motion of car body into account, and can be effectively used to study dynamic interactions between the leading and trailing bogies. The model, however, may be more complex and most likely unnecessary since the effect of one bogie on the other is known to be negligible in view of vehicle-track dynamic interactions.

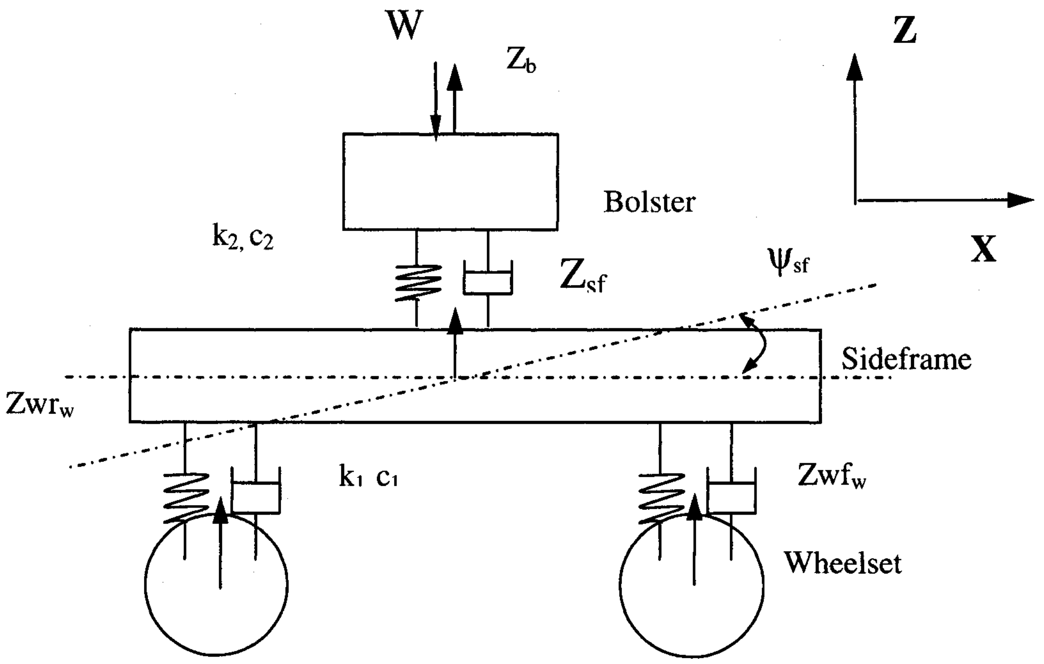

Figure 1.8: A typical two-dimensional five-DOF pitch plane vehicle model [1, 12]

All of the reported pitch plane models assume symmetric of both the vehicle loading and the vehicle-track structures, and linear properties of the vehicle components except for the wheel rail contact zone. These models may be considered sufficient to study the pitch dynamic couplings between the wheelsets, or between two bogies, but can not account for the roll motions of the vehicle components, such as the wheelsets, bolster and the car body. Moreover the contributions due to defects on the wheels rolling on the other rail can not be evaluated. Furthermore, the pitch plane models do not permit for analyses of the lateral motions of the vehicle and lateral interactions between the vehicle and the track system.

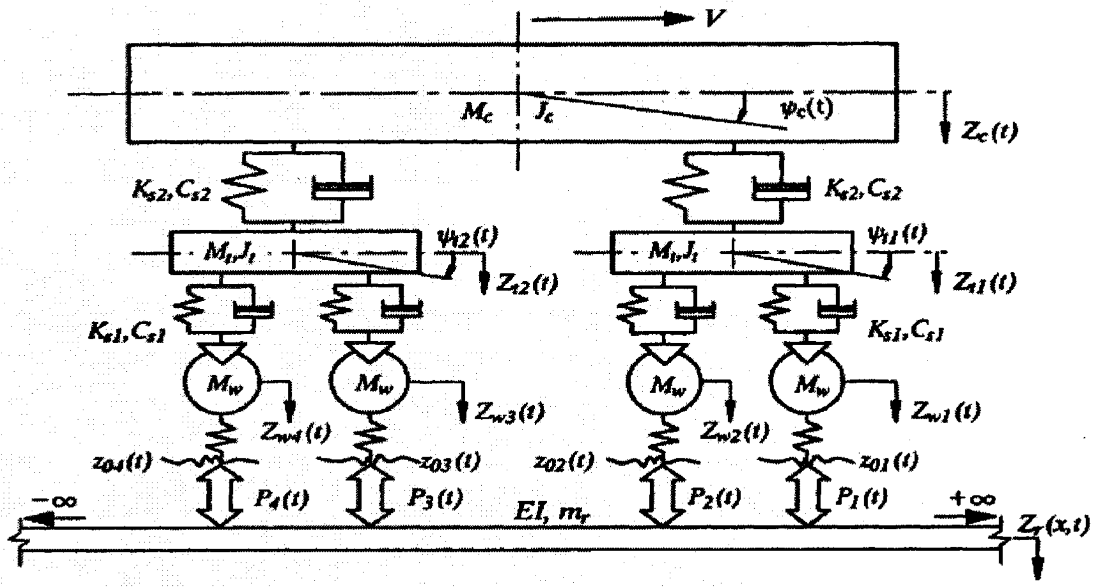

Figure 1.9: Two-dimensional 10-DOF pitch plane vehicle model [29, 35]

Three-Dimensional Models

Alternatively, a number of comprehensive three-dimensional vehicle models have been developed in recent years. In order to study the influences of asymmetric loading and asymmetric properties, a 3-D model including 10-DOF for the vehicle system has been developed [32]. The model, referred to as the "half car" model, is shown in Figure 1.10. The vehicle in such a model is generally represented by half car or an entire bogie including bolster (car body), sideframes and wheelsets. The DOF generally include: the vertical and roll motion of each of the wheelsets and the bolster (carbody); and vertical and pitch motions of the two sideframes.

The above 3-D vehicle model may be combined with an appropriate track model to study the effects that the wheel-rail interactions from one side of the track have on the other side. Such a model would further permit for analyses of the influences of many asymmetric factors, such as loading which is generally asymmetric in practice. Such a model can also be employed to study the lateral dynamic responses and the dynamic coupling between the lateral and vertical motions. The interactions between the leading and the trailing bogies, however, can not be examined.

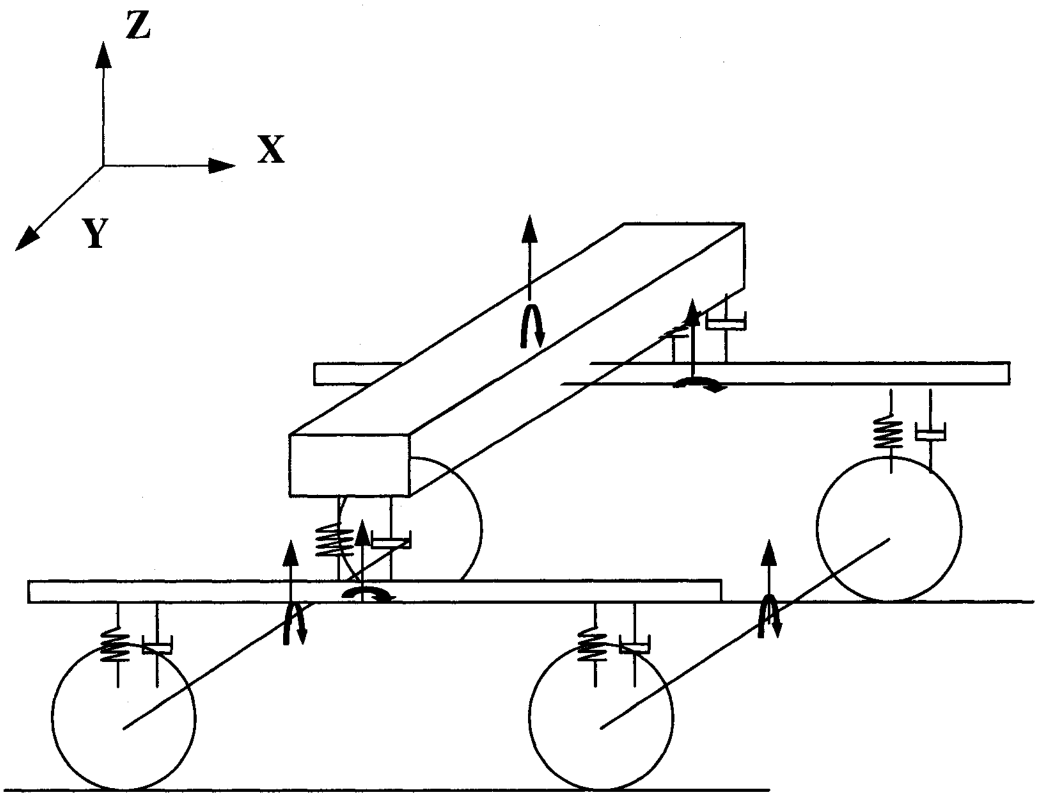

Figure 1.10: A typical 3-D ten-DOF vehicle model [32]

Comprehensive models of the entire vehicle system with large number of DOF have also been formulated and applied to study the system response to interface irregularities. Sun et al. [34] developed a 37-DOF model for the vehicle with primary suspension and 15-DOF model for the three-piece-bogie vehicle without the primary suspension to study the lateral and vertical dynamics of the wagon-track system. Such a model is considered quite adequate for investigation of the dynamic couplings between the leading and the trailing bogies, between two sides of vehicle, and between lateral and vertical motions of the vehicle-track system. Such a model can also permit for analyses of contributions due to pitch and roll motions of carbody. The model, however, yields total of 2077 differential equations of motion describing the dynamic vehicle-track system, and is considered to be computationally quite complex [34].

The 3-D vehicle system models generally assume that the components with the exception of the suspension are rigid masses and the elasticity of the components is neglected. This assumption would yield notable errors in response due to the effect of the wheelsets' elasticity on the dynamic coupling between the two sides of vehicle-track system. Such a model thus can not be used to study the propagation of the wheel OOR defects [18, 44].

In order to study the growth of the OOR wheel defects, such as corrugation, three-dimensional finite element (FE) models have also been developed [18, 34, 44]. In FE models, the wheelsets shaft are considered as elastic beams and the FEA is applied to study the effect of wheelsets elasticity on the non-uniform dynamic wear between the wheels and the rails. Besides FE vehicle models, a number of multibody dynamic vehicle models have also evolved in recent years to study the response of the vehicle to various excitations [45].

1.2.5 Track Model

As in the case of vehicle system, an array of track models has also evolved in the past few decades. Dahlberg [46] presented a comprehensive review of studies on dynamics of railway track system, including the construction, function and the dynamic properties of the railway track. Cai [24] summarized the simulation approaches used for analyses of track dynamics and responses. The analytical modeling of the track system is far more complex than that of the vehicle system. This is mostly attributed to the elasticity of the track system, which must be represented by a continuous system coupled with discrete and lumped-parameter components. Among the track system components, rail is the most important one, which is invariably modeled as a continuous beam structure with elastic support.

The dynamic deflection of the rail under a moving load is governed by two basic theories. The first one is the Bernoulli-Euler beam theory or simple beam theory, which is applied widely to study the deflection responses of the rails [18, 29, 35, 38]. This beam theory does not take into account the effect of shear distortion and rotational inertial of the beam structure under vibration. The dynamic response obtained by this theory is not appreciable enough when the depth-span ratio of the beam is small, the vibration frequency is high and the ratio of beam stiffness to that of the supporting foundation is small. Alternatively, the Timoshenko beam theory has been widely used to account for the effects of shear distortion and rotational inertia of the beam under high frequency vibration [2, 9, 31, 32, 33, 34, 37, 40, 41, 44].

A track model invariably involves sub-models of different layers with the support structure. Different track models have been development over the past decades that include considerable numbers of layers. In the early years, a single layer track model was used where the track was treated as an infinite beam (rail) on an elastic foundation and subject to a moving load [42, 47, 48]. Such models involved many simplifying assumptions and thus the deficiencies, namely: (i) sleeper mass and bending flexibility were neglected; (ii) detailed dynamic behavior of the track components could not be obtained; (iii) the contributions due to discrete rail supports from individual sleeper were neglected since these supports were replaced by a uniform underlying foundation.

Consequently, two-layer models of the track have been developed to include rails, sleepers, rail pads, ballast and the subgrade [1, 9, 15, 24, 37]. Figure 1.11 illustrates a typical two-layer planar track model which has been widely used to study dynamic wheel-rail interactions [2, 9, 18, 33, 37]. In these models, the rail is modeled as a continuous beam supported on discrete supports. The sleepers are modeled as lumped masses, and the rail pads and ballast are represented by spring and damping elements. The subgrade is considered to be rigid. The study conducted by Zhai [29] concluded that the wheel-rail impact force form two-layer track model was almost identical to that derived from a more complex three-layer track model. The low frequency component of the interaction force (second peak value in the contact force in the presence of a flat) estimated from the two-layer track model, however, was judged to be relatively higher, while the acceleration due to the ballast could not be obtained.

Alternatively, three-layer track models have been formulated where the ballast is modeled as a massive mass [38]. Such models can be employed to study the dynamic response of the track ballast, but the ballast parameters are generally difficult to be verified. It has been suggested that the two-layer track models are not sufficient for the study of the acceleration and impact forces inside ballast due to the wheel-rail interactions [29]. Makoto and Takumi [31] set up a five layers track model where ballast is divided into three different layers coupled through damping and spring elements. This model permitted to analysis the response of ballast at different position to the excitation at wheel-rail interface.

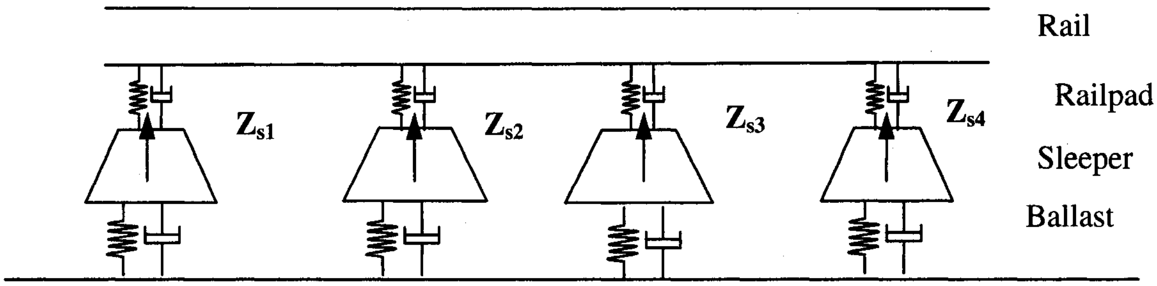

Figure 1.11: The two-layer plane track model

The dynamic wheel-rail interactions are most significantly influenced by the elastic track foundation. The track models generally employ two different foundation models: a **continuous elastic foundation** [2, 49] and a **discrete elastic support model** [17, 24]. A continuous elastic foundation model considers rails as beams on distributed elastic supports. Such continuous elastic foundation models simplify the complexities of the track support, and can not reflect the reality of the discrete characteristics of the sleeper supports. A continuous model thus can not yield the dynamic response of track with reasonably good accuracy at high frequency [1, 24]. A discrete elastic support model considers the rails as a beam seated on the discrete elastic supports [1, 2, 9, 32, 37]. Such a model thus reflects the discrete characteristics of the sleeper and yields reasonably good predictions of the vehicle-track dynamic interactions at high frequency [24, 29]. The dynamic responses of the coupled vehicle-track system to discrete supports as inputs can be effectively studied by this model. The entire track system is treated as a coupled system comprising several elements of the discrete elastic supports, which adds to the complexity of the model.

Two numerical methods are generally employed to solve for the vibration problems associated with the track system: generalized mode method and finite element method. Classical generalized mode method transfers the partial and ordinary differential equations set up in the natural coordinate system into the generalized mode coordinate system. By this approach, the partial differential equations, which describe the dynamic motion of continuous beams, are transferred into ordinary differential equations. Numerical methods, such as Raleigh-Ritz method, can thus be employed to study the dynamic responses of the track system. The accuracy of computation is determined by the total number of rail modes and sleeper bays taken into account. Jin et al. [38] used 100 rail modes and 100 rail sleeper bays in their study based on the Euler beam theory.

In recent years, finite element methods have been widely employed to carry out the study of track dynamics based on the Timoshenko beam theory [1, 2, 9, 32, 37, 40, 41, 44, 68]. Dong [1] created a detailed FE model to simulate for the track system in which the rail is modeled by an infinite long Timoshenko beam on discrete elastic supports, while the sleeper is represented by an Euler beam on a continuous elastic foundation. From the reported studies, it can be concluded that finite element method is a convenient tool for the analyses of the track based on both Euler and Timoshenko theory, while the generalized mode method can only be applied to the track model based on Euler theory.

The elastic properties of the track system have been incorporated in the vehicle-track models using linear and non-linear track models. Linear track models invariably comprise linear spring and viscous damping elements. Reported studies of the wheel-rail impact loads due to wheel defects have shown that the linear track models yield reasonable good agreements with measured peak contact force in the presence of wheel defects [1, 2, 32, 35, 38]. The linear track models have thus been mostly widely used in studies on wheel-rail interactions. The track, however, exhibits nonlinear elastic properties since the pad and ballast stiffness varies with applied load. Moreover, the adjacent sleeper may be lifted clear to the ballast under axle loads since the ballast cannot sustain tensions, which further contributes to nonlinear track properties [33, 41, 43]. Nielsen and Osczrsson [41] investigated the wheel-rail impact loads using linear and nonlinear models and concluded that a nonlinear track model yields higher magnitudes of impact loads than the linear track model in the low to middle-speed range. The measured value of the wheel rail impact force due to a wheel flat, however, was found to lie between the values obtained from the linear and nonlinear track models. Bother the linear and nonlinear models, however, resulted in similar magnitudes of wheel rail impact forces at higher speeds (>70km/h). Both the models result in impact forces larger than the measured data at high speed.

1.2.6 Contact Model

In vehicle-track interaction simulation, the wheel-rail contact model plays the most vital role and it couples the vehicle model with the track model. The obtained interaction force prediction ability of vehicle-track model, to a great extend, depends on the contact model. A number of theories have been applied to describe the wheel-rail dynamic contact in the past decades, and many contact models have evolved. Among these theories, the Kalker contact theory has been mostly used, which can account for elastic rolling contact effectively [50, 51, 52]. The vast majority of the contact models employed in the studies of lateral and longitudinal dynamics are based on this contact theory [50, 42]. The studies involving vertical vehicle-track dynamic interactions alone, however, employ Hertzian contact theory to describe the rolling contact between the wheel and the rail [2, 9, 37, 38].

The reported wheel-rail contact models can be generally categorized in three different types: (i) point contact model where the wheel and rail are connected via a single contact spring that may be either linear or nonlinear [2, 6, 33, 35, 37, 38, 40, 44]; (ii) multipoint contact model in which the contact length and contact overlap are taken into account [1, 32, 34]; and (iii) 3-D contact model, in which takes into account the contact penetration along the lateral and longitudinal directions [3].

Point Contact Model

The simplest and widely used wheel-rail contact model used in the study of vehicle-track vertical dynamics is the point contact model, consisting of a wheel, a rail and a contact spring between the wheel and the rail, as shown in Figure 1.12 [2, 33, 38, 44]. The contact spring can be either linear or nonlinear, which are based on Hertzian contact theory. Point contact models are applied assuming that the wheel-rail contact patch is very small so that the contact can be considered as a point.

The contact model employs Hertzian nonlinear contact theory, which considers the wheel and rail contact through a single non-linear spring. The contact force is determined from the following equation [1, 24]:

$$P = C_H \Delta u^{\frac{3}{2}} \tag{1.3}$$

Where Δu is the overlap between wheel and rail, which is is determined from the relative wheel rail penetration and wheel rail profile imperfections; and C_H is the Hertzian contact coefficient. This contact force relationship is widely used to determine the normal interaction force in wheel-rail contact simulation [2, 33, 35, 37, 38, 40, 44].

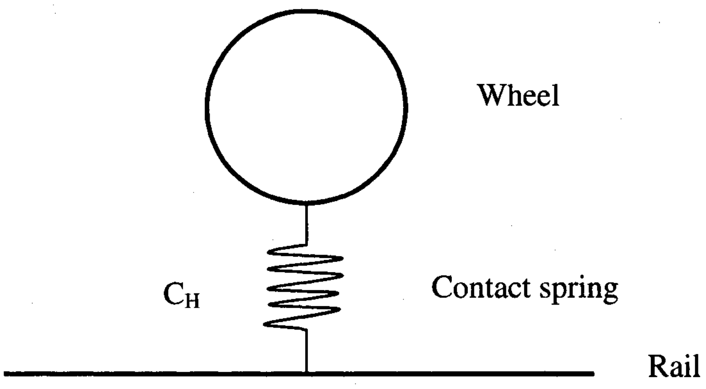

Figure 1.12: Point wheel-rail contact model

In early years, linear contact stiffness was used and evaluated corresponding to the static wheel load P_o. in order to simplify the computations, such that [1]:

$$k_H = \frac{\partial P}{\partial \Delta u} = 1.5 C_H \left(\frac{P_o}{\Delta u_o}\right)^{\frac{1}{3}} \tag{1.4}$$

Where P_o is the static wheel load and Δu_o is the wheel-rail overlap corresponding to the static wheel load.

Compared with the non-linear point contact model, the linear contact model employs a small and constant contact stiffness evaluated in the static state, and thereby always underestimates the dynamic wheel-rail contact force, especially in the presence of wheel rail defects.

In point contact models, the contact point is usually assumed to lie under the center line of the wheel, while the contributions due to the length of contact patch to the dynamic wheel rail interactions can not be estimated. Reported studies have concluded that the non-linear Hertzian contact model, incorporating linear track model, results in reasonably good agreement with the measured data in terms of wave pattern of the contact force, but it underestimates the impact force at low speeds and yields an overestimation of the force at high speeds in the presence of wheel flats [33, 41].

Multipoint Contact Model

Dong [1] proposed a multipoint contact model, where the contact region is represented by a patch comprising equal-spaced springs, as shown in Figure 1.13. Every spring element is linearized, and the elements are distributed along the longitudinal direction symmetrically about the wheel center line. The stiffness of each individual spring element is established based on the Hertzian contact theory [1], while the element deflection is determined from wheel rail profile.

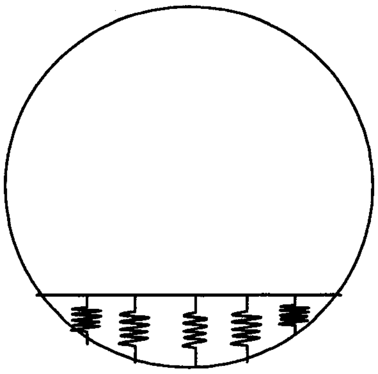

Figure 1.13 Multipoint wheel-rail contact model

Multipoint contact model takes into account the length of contact patch and the loss of contact as the wheel flat enters the contact zone. This model assumes uniformly distributed contact patch about the center line even if the wheel rail defects are present in the contact zone. Furthermore, the width of the contact patch is neglected and the non-uniform or partial wheel-rail contact along the longitudinal direction when wheel rail defects are located in the contact patch cannot be obtained. Sun [34] conducted an investigation of impact load due to wheel flat based on the multipoint contact model and the results showed that the impact force is overestimated at speed of 70 km/h.

3D Contact Model

The models mentioned above are all based on Hertzian contact theory, which assume that the wheel rail contact patch is elliptic. However, the work by Kolvalev et al. [35] showed that the contact patch shape is far from ellipse. A three-dimensional model was developed to account for the contact length and width. The comparison of the normal contact force obtained form this model with that from Hertzian contact theory revealed that the there is a notable difference of normal contact force between 3D and Hertzian contact models.

1.3 DISSERTATION SCOPE AND OBJECTIVE

With increasing train speed and haul loads, the potential problems caused by a wheel flat have become of greater concerns. A great deal of research efforts have thus been made. These studies have provided guidelines for acceptable limits of wheel flats for railway transportation industry to ensure safe and efficient operation. The vast majority of the efforts, however, focus on impact interactions due to a single flat. Although the presence of some multiple wheel flats have been widely noticed, only limited efforts have been made to quantify the influences of multiple flats. Some of the present removal criteria such as those outlined by AAR [13] and Transport Canada [25], provide guidelines on double wheel flats, while insufficient fundamental information exist in support of such guidelines. Furthermore, the presence of a flat on the surface of one wheel of a wheelset may induce high magnitude impact forces on the contact interface of the other wheel. The presence of flats in both the wheels of a wheelset may induce higher magnitudes of impact loads. The nature of such impact forces would depend upon the severity of flats and phase difference between the two flats, which have not been addressed in the literature. The high frequency of multiple wheel flats occurrences necessitates the investigation of wheel-rail impact load due to multiple wheel flats.

The primary objective of this dissertation research is aimed to development of an analytical model for describing the coupled vehicle-track system dynamics, which is essential to study the vertical interactions between wheel and rail, particularly in the presence of multiple wheel flats. In the coupled system, only the vehicle system is considered to be of primary concern, while a relatively simpler track model can be employed in order to simplify the computations. The specific objectives of this work are formulated as:

1. To develop an adaptive wheel rail contact model based on the radial spring assumption to compute normal component of wheel rail contact force with adequate consideration of asymmetric and partial contact as the defect enters the contact zone. It is anticipated that such model can avoid overestimation of wheel rail contact force induced by wheel rail defect at high speeds, as observed for various point contact models.
2. Develop a three-dimensional track system model using two Timoshenko beams supported by discrete elastic supports, where the sleepers are considered as rigid masses, and the rail pad and ballast as spring-damper elements.
3. Develop a two dimensional roll-plane vehicle model and integrate it with 3-D track model to study the interactions of two sides of the vehicle and track while taking into account the contributions due to roll motions.
4. Formulate a haversine model for single as well as multiple wheel flats to study the resulting impact forces.
5. Proposed a numerical simulation methodology for solving the coupled continuous and discrete system models.

6. Evaluate the impact load responses resulting from a single as well as multiple wheel flats, and the influence of a defect within one side of the vehicle-track system on the impact forces imposed of the other side.

1.4 ORGNIZATION OF THE THESIS

In chapter 2, an adaptive wheel rail contact model is developed. The formulations for the wheel-rail contact force are derived on the basis of the radial spring contact mechanism. The geometry of the wheel with a flat is defined and the radial spring stiffness of the wheel is established. A procedure for determining the wheel-rail contact patch in the presence of wheel rail defects is described. A simple lamped mass vehicle track interaction model is then developed and analyzed to demonstrate the validity of the proposed adaptive model against the well-established Hertzian non-linear point contact model.

In chapter 3, a roll-plane model of vehicle is developed together with a 3-D two layers linear discrete support track model. The two models are coupled through the proposed adaptive wheel-rail contact model. Central finite difference method (CDFM) is employed to analyze the coupled continuous and lamped mass dynamic system models.

In chapter 4, the dynamic interactions between the vehicle and the track system in steady-state are investigated to validate the proposed model and numerical method. The effects of the integration time step and length step of the CDFM on the responses of the vehicle-track system are thoroughly evaluated.

In chapter 5, the impact forces due to a single wheel flat are investigated. A thorough comparison of the results from the proposed model is undertaken with the data from the reported studies. A comprehensive parametric study is conducted to enhance an understanding of the roles of various design and operation factors affecting the impact loads induced by wheel flat.

In chapter 6, the impact loads due to multiple flats are investigated. The simulations are performed for two cases of multiple flats, namely, (i) two flats on one wheel; and (ii) one flat on each of the wheels in one wheelset. The results are discussed to highlight the influences of the multiple wheel flats and cross-coupling effects.

The highlights and major conclusions drawn from this study together with recommendations for the future work are finally presented in chapter 7.

CHAPTER 2

AN ADAPTIVE WHEEL-RAIL CONTACT MODEL

2.1 INTRODUCTION

The wheel-rail interaction forces have significant effect on dynamic behavior of the railway vehicle and track systems. The rolling contact mechanism is a complex problem and has attracted numerous investigations in the past few decades. In the mathematical modeling and simulation of railway vehicle-track dynamics, it is the contact model that couples the vehicle system and track system together. An accurate description of contact between the wheel and the rail is thus a necessary condition to obtain reliable simulation results for the vehicle-track system. The contact problem can be divided into two independent ones: normal or vertical contact and tangential contact problem. Tangential force between the wheel and the rail causes elastic local deformation in both wheel and rail in the contact area, which in turn causes the rolling velocity to differ from the circumferential velocity. Carter [50] was the first one to express this phenomenon in the form of creep hypotheses. Kalker's linear and non-linear rolling contact theories are most widely used in railway vehicle lateral and longitudinal dynamics [51, 52].

As discussed in chapter 1, the most widely used vertical contact model is based on Hertzian non-linear elastic contact theory, which describes the contact behavior of two cylinders. Such contact model is essentially a point contact model based on the assumption that the contact patch is very small [24, 55]. It is further assumed that the contact point lies on the centerline of the wheel. This is a reasonable assumption in modeling vertical contact forces between a perfect wheel and rail geometry. However, when there is a defect on the wheel or rail in the contact zone, the induced impact force predicted using Hertzian contact model may not be very reliable. A few studies have suggested that the Hertzian non-linear point contact model incorporating linear track model consistently underestimates wheel flat-induced impact loads at low speeds, while overestimates at high speeds [2, 41].

Multipoint contact model has also been proposed to predicted contact forces between wheel and rail with a defect such as a wheel flat [1]. Such a model, however, assumes that the vertical contact springs are discretely and symmetrically distributed about the vertical center line of wheel regardless of perfect or defective wheel and rail profile. In the wheel-rail vertical contact study [1], it has been shown that multipoint contact model estimates impact force very similar to that of Hertzian contact model. It is not difficult to visualize that in the presence of a defect, such as a wheel flat, the radial springs will not be symmetrically distributed about the vertical center line of wheel when the region with flat enters or leaves the contact area.

For the present investigation of impact forces due to wheel flats, an adaptive wheel-rail continuous contact model is developed to overcome the limitation of the published models described above. The proposed model considers the contact length, contact depth, and possible partial contact due to defective wheel/rail profile. This chapter presents the detailed derivation of the adaptive contact model and comparison of impact force response with that derived from Hertzian non-linear point contact model. This adaptive contact model is based on the concept of continuous radial springs uniformly distributed over an adaptive wheel-rail footprint, which has been successfully utilized in study of ground vehicle contact problems associated with pneumatic tires [56].

The adaptive wheel-rail contact model developed for vehicle dynamics neglects the lateral and longitudinal forces. It is also assumed that the contact patch is very small and it cannot exceed the flat length in a wheel. Due to conical or worn profile of the railway wheel, wheel radius at the contact point always varies as the wheel rolls along the track. It is however, assumed that such variations are very small irrespective of the wheel profile and any possible lateral motions.

2.2 DEVELOPMENT OF WHEEL-RAIL CONTACT FORCE (PERFECT WHEEL PROFILE)

The wheel-rail vertical interaction is represented by a set of continuous radially distributed springs that takes into account the stiffness of the wheel and the rail, as shown in Figure 2.1. As shown, the contact patch between points A and A_1 is designated by contact length l_e. The radially distributed springs are assumed linear, while the constant radial spring stiffness K_w, is defined as the magnitude of force required to produce unit angular deformation of the spring. The contact force is developed by radial interpenetration of the wheel into the rail. The elemental radial deflection, δ_i, at an angle α_i, leads to radial spring force dF as shown in Figure 2.2, such that:

$$dF = (K_w \delta_i) d\alpha_i \tag{2.1}$$

Where α_i is the angle between the vertical centerline of wheel plane and arbitrary contact point within the contact length.

The elemental radial deflection δ_i can be expressed as:

$$\delta_i = R_i - \frac{h}{\cos\alpha_i} \tag{2.2}$$

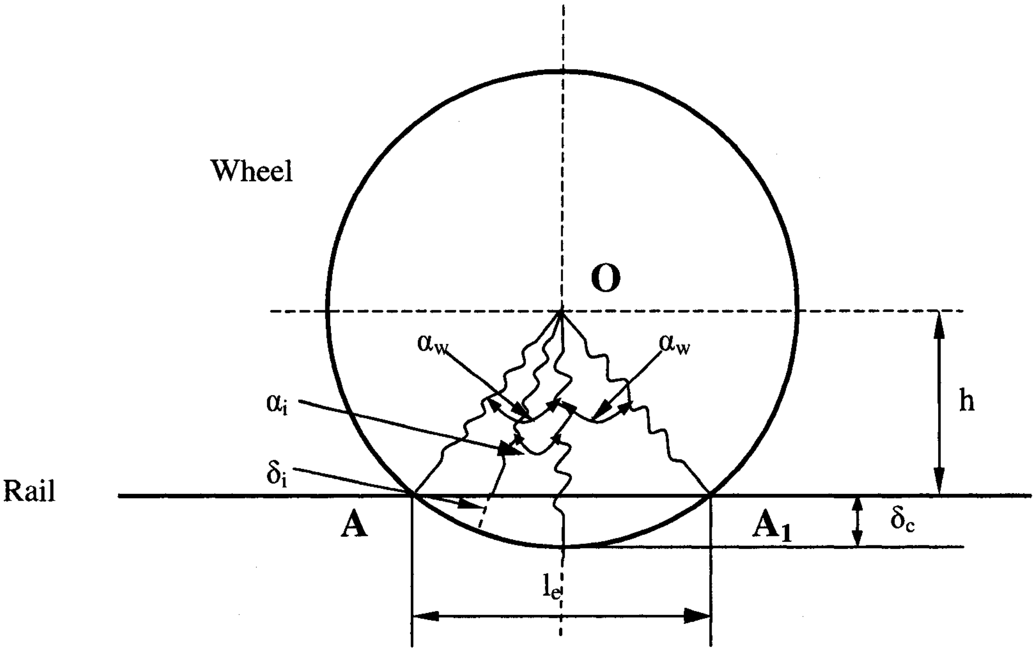

Figure 2.1Radial contact representation of wheel-rail interactions

Where h is distance between the wheel center and the contact patch center, given by:

$$h = R_w - \delta_c \tag{2.3}$$

Where R_w is nominal wheel radius and δ_c is wheel-rail deflection at contact patch center, or the wheel rail contact overlap.

The normal and tangential components of the contact force, shown in Figure 2.2, can be expressed as:

$$\begin{aligned} dF_n &= (K_w\delta_i \cos\ \alpha_i\ )d\alpha \\ dF_t &= (K_w\delta_i \sin\ \alpha_i\ )d\alpha \end{aligned} \tag{2.4}$$

Upon combining equations (2.2) to (2.4) and integrating over the entire contact patch ($-\alpha_w, \alpha_w$), the resultant wheel-rail normal contact force with perfect contact profile can be expressed as:

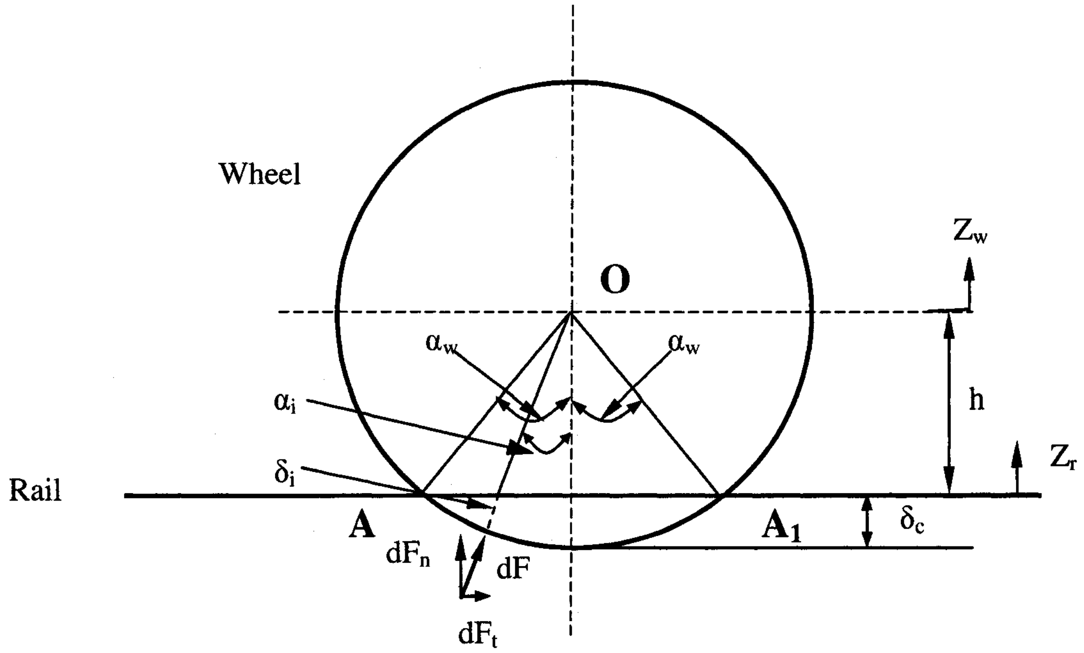

Figure 2.2: Elemental deflection and contact force dF

$$P = F_n = 2K_w R_w (\sin\alpha_w - \alpha_w \cos\alpha_w) \tag{2.5}$$

Where α_w is wheel-rail contact patch angle, which is defined as half of the angle formed by a line connecting wheel center to the front contact point, and a line connecting the wheel center to the rear contact point. A symmetric contact about the wheel center line is assumed for a defect free wheel. The contact angle can be expressed as:

$$\alpha_w = \cos^{-1}\left(\frac{R_w - \delta_c}{R_w}\right) \tag{2.6}$$

The contact overlap δ_c can be determined from wheel center displacement z_w and corresponding rail displacement z_r, such that:

$$\delta_c = \begin{cases} z_r - z_w & z_r - z_w > 0 \\ 0 & z_r - z_w \leq 0 \end{cases} \tag{2.7}$$

It is easy to see that when the overlap δ_c is equal to zero, the wheel contact angle is zero and the contact force, therefore, is zero. In this study, it is assume that the rail wheel vertical displacements (z_r, z_w) are equal to zero, when the wheel and the rail are just about to come in contact.

2.3 CONTACT MODEL WITH WHEEL FLATS

2.3.1 Development of Wheel-Rail Contact Force

As shown in Figure 2.3, the presence of a wheel flat could yield a contact patch that is asymmetric about the wheel centerline. For the contact patch defined by (α_f, α_r), combination of equations (2.2) to (2.4) and integration over the contact patch (α_f, α_r), yields resultant normal contact force as:

$$P = F_n = \int_{\alpha_f}^{\alpha_r} K_w (R_i - \frac{R_w - \delta_c}{\cos \alpha_i}) \cos \alpha_i d\alpha_i \tag{2.8}$$

Where δ_c can be calculated from equation (2.7); R_i is the instantaneous radius of the wheel at a position α_i; α_f and α_r are positions of the extreme front and rear contact point. In this study, it is assumed that the origin of contact angle is the vertical center line of wheel, and the angle is positive when measured counterclockwise from wheel center line.

Form equation (2.8), it can be seen that computation of wheel-rail contact force requires: (i) determination of instantaneous wheel radius R_i at any point of contact zone; (ii) determination of the contact patch, or front contact and rear angles (α_f and α_r) at every instant; and (iii) establishment of radial spring constant K_w.

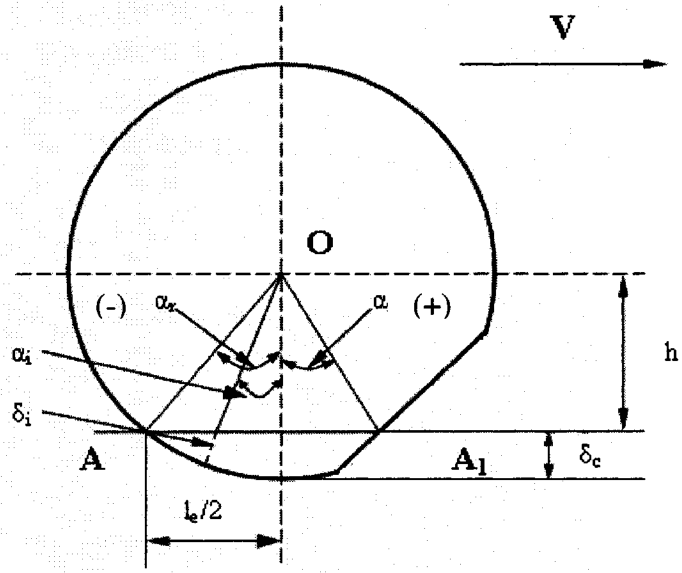

Figure 2.3: Deflection of an element of wheel-rail contact patch with defective wheel

2.3.2 Determination of Radius R_i at an Arbitrary Point on the Wheel Rim

In order to determine the radius of the wheel at any point, it is essential to derive relations describing the flat and its location around the wheel.

Description of Wheel Profile with Flat

The profile of a wheel with a flat can be described by its radius and corresponding angle β between a reference line and the radius, as shown in Figure 2.4. The flat is designated by line BB1 and the reference is chosen as the vertical line through wheel center. The initial position of the flat is described by the angle between the reference line and the wheel flat center line (β_o). The length of the flat is determined by arc angle φ, which represents half of the chord angle between OB and OB_1. For small a flat length, this arc angle can be expressed as:

$$\varphi=\frac{l_f}{2R_w} \tag{2.9}$$

Where l_f is the length of flat.

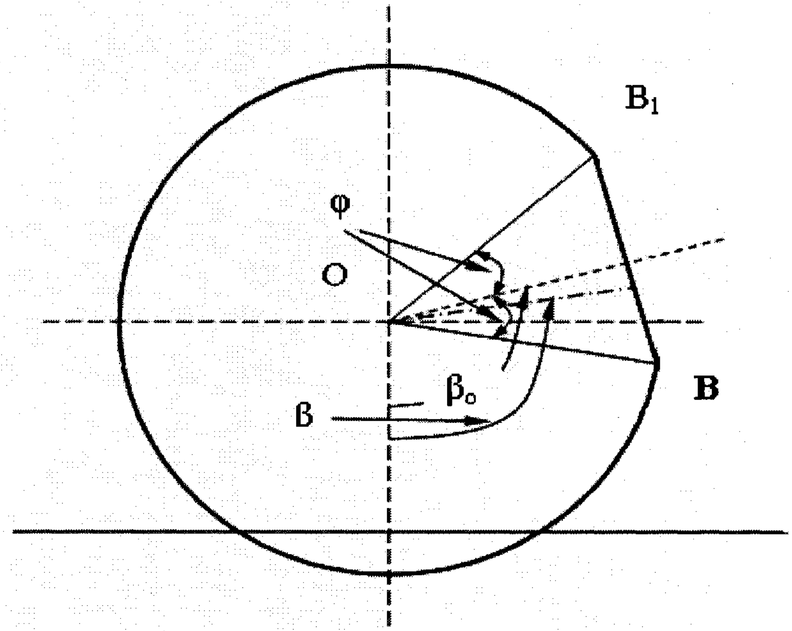

Figure 2.4: Wheel profile with a flat

The instantaneous radius of wheel at an arbitrary position can now be simply expressed as:

$$R_i = \begin{cases} R_w & 0 < \beta \leq \beta_0 - \varphi \;\; or \;\; \beta_0 + \varphi < \beta \leq 2\pi \\ R_w - f & \beta_0 - \varphi < \beta \leq \beta_0 + \varphi \end{cases} \tag{2.10}$$

Where f is variation in the wheel radius due to a wheel flat, and is dependent upon the type of flat being considered.

When the wheel flat is just formed, it looks like a chord. It is often referred to as "fresh flat" or "chord flat". The two ends of the "chord", however, become rounded with continued operation. The resulting profile is thus often described by a cosine function and usually called "rounded", or "worn", or "haversine" flat.

Chord Type Flat

For a fresh or chord type flat, *f* can be obtained from the geometry of the wheel profile, such that:

$$f = R_w - \frac{R_w - D_f}{cos(\beta - \beta_o)}; \qquad \beta_0 - \varphi < \beta \leq \beta_0 + \varphi \tag{2.11}$$

Substituting equation (2.11) into (2.10) yields following expression for wheel radius R_i at any point:

$$R_i = \begin{cases} R_w & 0 < \beta \leq \beta_0 - \varphi \ OR \ \beta_0 + \varphi < \beta \leq 2\pi \\ \dfrac{R_w - D_f}{cos(\beta - \beta_o)} & \beta_0 - \varphi < \beta \leq \beta_0 + \varphi \end{cases} \tag{2.12}$$

Where D_f is flat depth, and can be obtained from:

$$D_f = R_w - \sqrt{R_w^2 - \frac{l_f^2}{4}} \tag{2.13}$$

Haversine Type Flat

Wheel flat is often treated as a "haversine" flat to account for rounded ends of the "chord". The variations in the radius due to such a flat, *f*, can be described by [57, 58]:

$$f = 0.5 D_f \left[1 - cos(\frac{2\pi x}{l_f}) \right] \tag{2.14}$$

The depth of a haversine flat D_f can be estimated from if it is unknown [57]:

$$D_f = \frac{l_f^2}{16 R_w} \tag{2.15}$$

The distance between an arbitrary point on the flat and the front end of the flat, *x*, can thus be expressed in terms of angle *β*, such that:

$$x = \frac{l_f}{2} + (R_w - D_f) tan(\beta - \beta_o), \qquad \beta_0 - \varphi < \beta \leq \beta_0 + \varphi \tag{2.16}$$

The variation in wheel radius, f, can be finally evaluated by substituting equation (2.15) and (2.16) into (2.14). The instantaneous wheel radius can be then obtained as a function of position β by substituting f into equation (2.10).

As an example, the wheel radius as a function of wheel position β is shown in Figure 2.5. This result is obtained for a 100 mm long chord and haversine flat, nominal wheel radius $R_w = 0.4572$ m and $\beta_o = -90^\circ$.

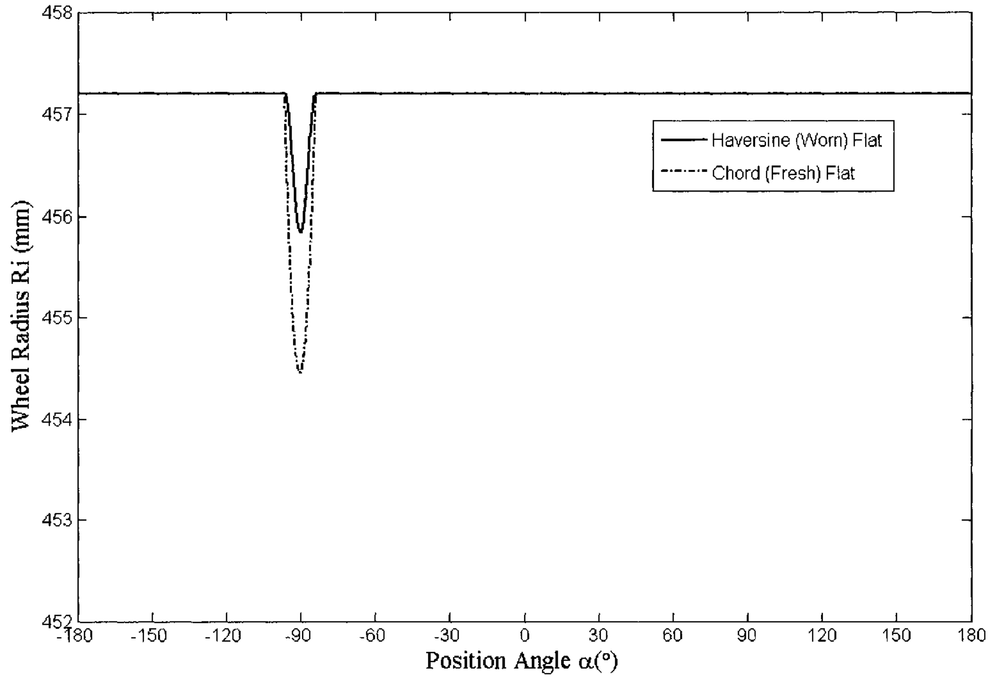

Figure 2.5: Changes in effective rolling radius of stationary wheel with a flat

The results, as expected, clearly show that the haversine formulation results in significantly smaller depth than that of chord flat for identical flat lengths. On the other hand, if a chord flat is first formed and then rounded with use, the depth of both flats will be nearly identical, while the rounded flat will be relatively longer. In this study, only haversine flat (rounded or worn flat) model is used to describe wheel defect with a given flat length and depth since this model is more commonly used, and such defect is more commonly observed in practice.

Instantaneous Position of a Flat on a Rotating Wheel

The position of the wheel flat with reference to a reference axis would vary as the wheel rotates. Figure 2.6 shows the flat position at an instant *t*, where the flat has shifted by an angle γ. For a constant forward velocity *V*, the angle γ can be expressed as:

$$\gamma = \omega t = \frac{V}{R_w} t \tag{2.17}$$

The corresponding new position of flat is then given by $\beta_o - \gamma$.

Equation (2.10) can now be expressed as a function of time to yield:

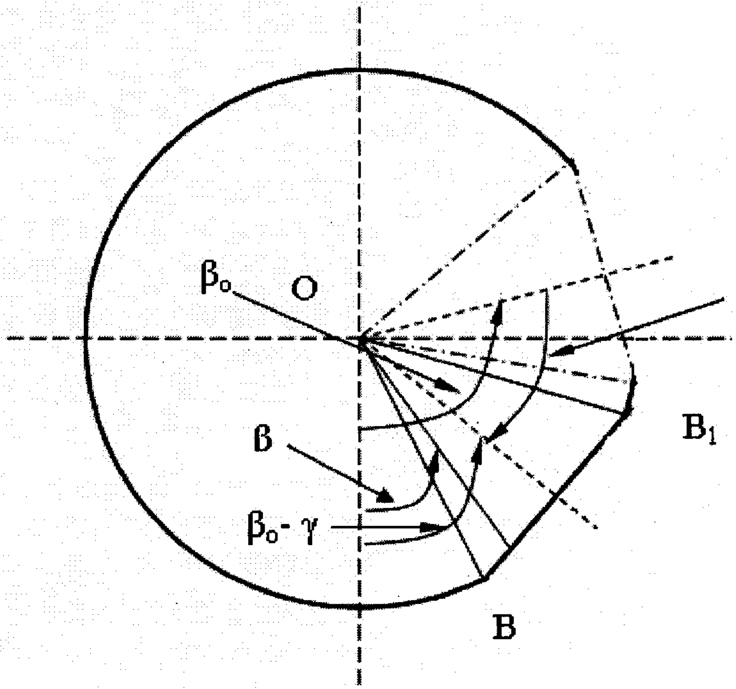

Figure 2.6: Flat position on a moving wheel

$$R_i(t) = \begin{cases} R_w; & 0 < \beta(t) \le (\beta_0 - \gamma(t)) - \varphi \;\; OR \;\; (\beta_0 - \gamma(t)) + \varphi < \beta(t) \le 2\pi \\ R_w - f(t); & (\beta_0 - \gamma(t)) - \varphi < \beta(t) \le (\beta_0 - \lambda(t)) + \varphi \end{cases} \tag{2.18}$$

For a chord type flat, equations (2.11) and (2.12) yield:

$$f(t)=R_w-\frac{R_w-D_f}{cos[\beta(t)-(\beta_o-\gamma(t))]} \tag{2.19}$$

$$R_i(t)=\begin{cases} R_w & 0<\beta(t)\leq(\beta_o-\gamma(t))-\varphi \;\; OR \;\; (\beta_o-\gamma(t))+\varphi<\beta(t)\leq 2\pi \\ \dfrac{R_w-D_f}{cos[\beta(t)-(\beta_o-\gamma(t))]} & (\beta_o-\gamma(t))-\varphi<\beta(t)\leq(\beta_o-\gamma(t))+\varphi \end{cases} \tag{2.20}$$

Similarly for a haversine type flat, *f* can be determined from equation (2.14) by substituting for *x(t)*, which is now a function of time and given by:

$$x(t)=\frac{l_f}{2}+(R_w-D_f)tan[\beta(t)-(\beta_o-\lambda(t))]; \quad (\beta_o-\gamma(t))-\varphi<\beta(t)\leq(\beta_o-\gamma(t))+\varphi \tag{2.21}$$

Radius of wheel with a haversine flat can now be determined as a function of time by substituting for *f* in equation (2.18). Figure 2.7 shows the variation in wheel radius at the contact patch center when rolling at a speed of 50 km/h. For this case the wheel and the flat are defined by: $R_w = 0.4572$ m, $l_f = 100$ mm, $D_f = 1.5$ mm and $\beta_o = 90°$.

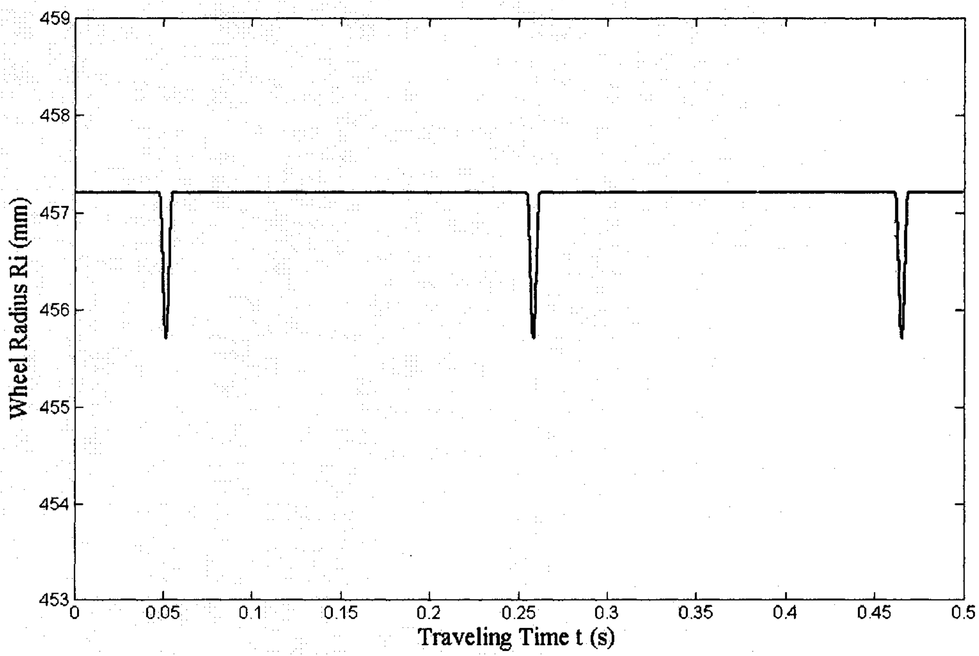

Figure 2.7: Changes in effective rolling radius of a moving wheel with a flat

2.3.3 Determination of Contact Patch

As illustrated earlier in Figure 2.3, a wheel flat would yield asymmetric contact geometry about the vertical wheel centerline. The analysis of this geometry involves identification of the wheel-rail contact patch, or the extreme front and rear contact angles (α_f, α_r) in the presence of a flat, as shown in Figure 2.8. The figure also shows the contact geometry for perfect wheel, which is described by angle $\pm\alpha_w$. The contact geometry is derived upon consideration of the displacements of wheel and rail, which yield overlap δ_c using equation (2.7). Furthermore, the instantaneous radius of wheel rim R_i is derived from equation (2.20). The positions of the front and rear contact point position (α_f, α_r) are derived from the corresponding radii $R(\alpha_f)$ and $R(\alpha_r)$, such that:

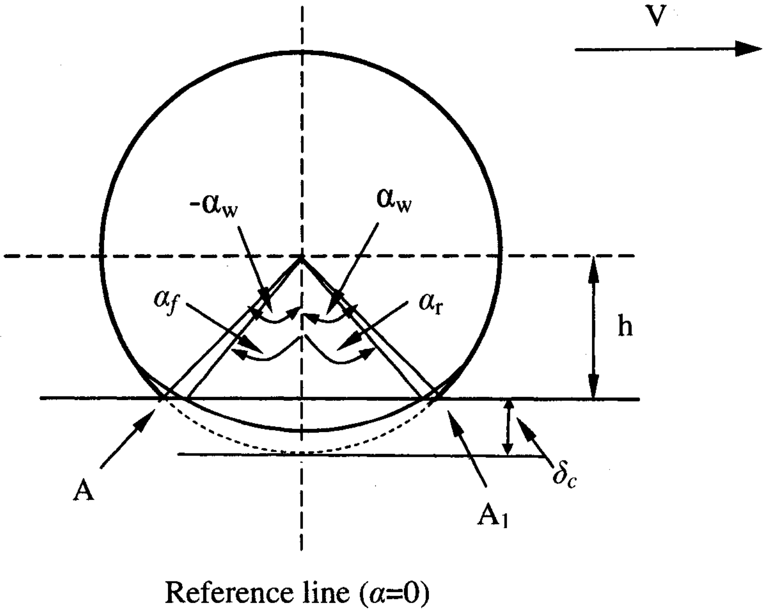

Figure 2.8: Identification of wheel rail contact patch (α_f, α_r) in specified co-ordinate system

$$\begin{aligned} R(\alpha_f)\cos(\alpha_f) &= R_w - \delta_c \\ R(\alpha_r)\cos(\alpha_r) &= R_w - \delta_c \end{aligned} \qquad (2.22)$$

Within the contact patch:

$$R(\alpha_i)\, cos(\alpha_i) > R_w - \delta_c \tag{2.23}$$

And outside the contact patch:

$$R(\alpha_i)\, cos(\alpha_i) < R_w - \delta_c \tag{2.24}$$

Above formulations suggest that an iterative approach can be adopted to derive the contact patch coordinates. Assuming a defective free wheel profile, contact patch angles are initially taken as $-\alpha_w$ or α_w. The wheel radii R_i at every point within α_w are computed until the extreme contact points are established using the above requirements. The program flow chart to establish the front contact point position is presented in Figure 2.9.

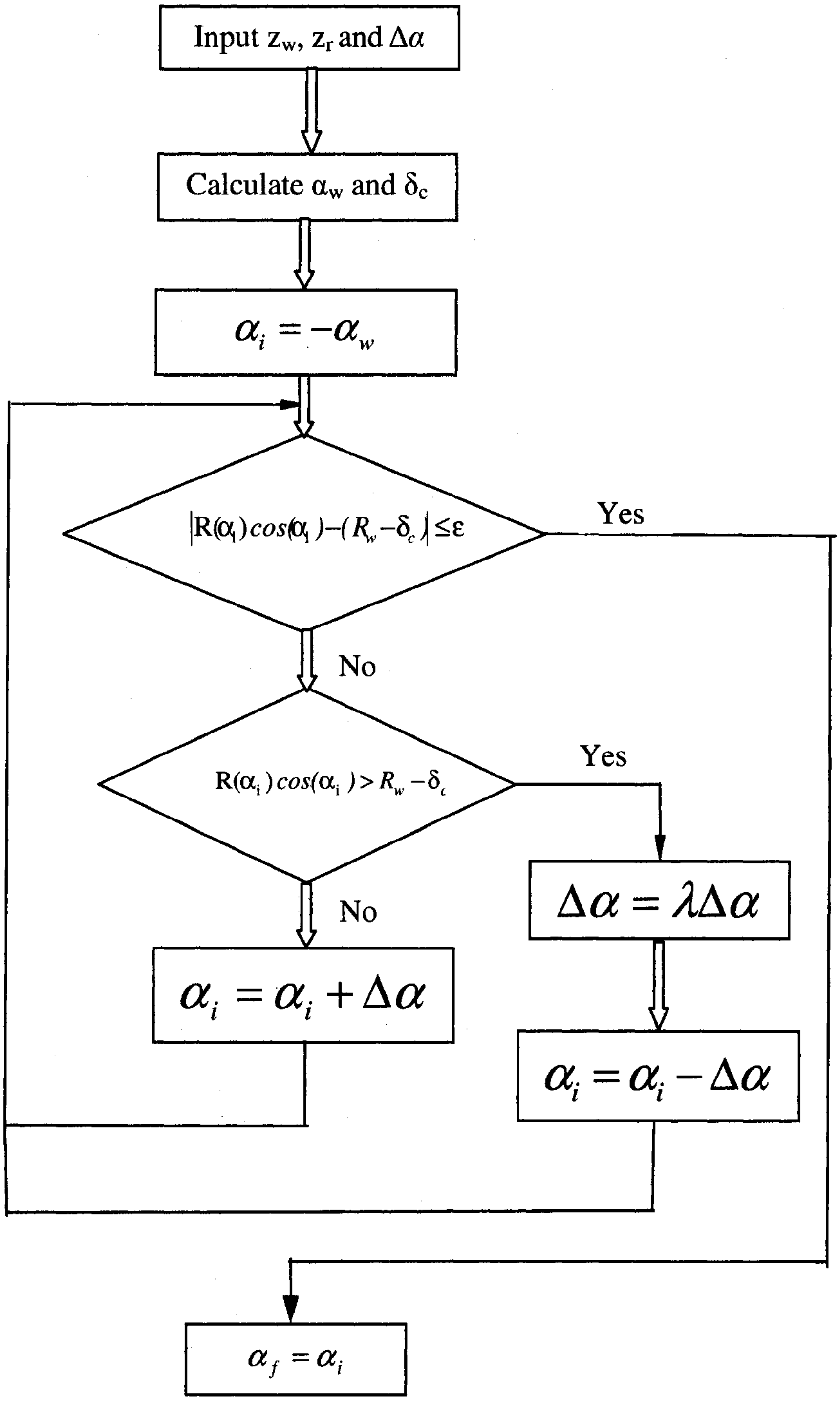

Note: ε is defined as error tolerance and λ is a real number less than 1.

Figure 2.9: Program chart to find front contact point

2.3.4 Establishment of Wheel-Rail Contact Radial Spring Stiffness

The effectiveness of the proposed adaptive contact model is largely dependent on the identification of reliable value of the radial spring constant K_w. Although experimental characterization would be desirable, an estimate of K_w may be obtained from analysis of wheel-rail interpenetration under a static load P_o. Rewriting equation (2.5), yields an expression for the stiffness K_w:

$$K_w = \frac{p_o}{2R_w(\sin\alpha_w - \alpha_w\cos\alpha_w)} \tag{2.25}$$

Where α_w can be determined from equation (2.6). The static wheel rail overlap δ_o should be ideally determined by experimentally measuring the static displacement of rail and wheel center, which is beyond the scope of the present investigation. Alternatively it can be derived from the Hertzian non-linear contact theory, which provides following relationship between applied load and wheel-rail overlap [24]:

$$P = C_H\delta^{\frac{3}{2}} \tag{2.26}$$

Where δ is the overlap between wheel and rail; and C_H is the Hertzian contact coefficient. The above relationship can also be applied to determine static overlap of wheel and rail, δ_o, by assuming the contact force as the static load P_o.

The proposed adaptive model was analyzed to determine force-deflection behavior of a defect-free wheel-rail interaction. The results are compared with that derived from Hertzian model in Figure 2.10. The results show that force-deflection relationship of the proposed adaptive contact model is very similar to that of the Hertzian non-linear point contact model. The contact force for the adaptive contact model was determined using equation (2.5).

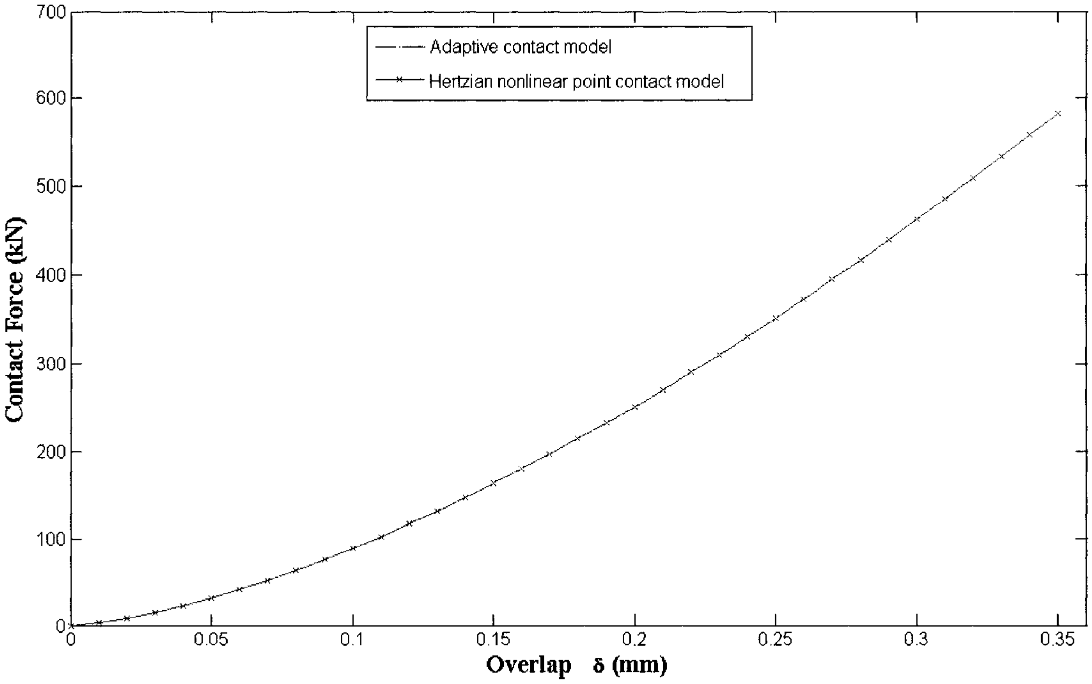

Figure 2.10: Relationship between vertical contact force and wheel rail overlap (Static load: $P_0 = 82$ kN; $C_H = 0.87\times10^{11}$ N/m$^{3/2}$; $R_w = 0.4572$ m)

2.4 COMPARISON OF ADAPTIVE AND HERTZIAN CONTACT MODELS

As discussed before, the proposed adaptive contact model takes partial or asymmetric contact into account when there is a defect in the contact zone. Other contact models, such as Hertzian point contact, calculate contact force based on symmetric contact assumption regardless of the geometry of defect in the contact zone. As pointed out in Chapter 1, Hertzian and multipoint contact models are shown to predict comparable force-time history and peak force characteristics [1]. In order to examine the adaptive contact model, a simple lumped parameter model of the vehicle-track system is considered. The vehicle-track model together along with adaptive rail-wheel contact model solved in the presence of a haversine flat is analyzed to derive impact force response.

2.4.1 Vehicle Track Model

The track system is modeled by a simple lumped mass supported by a lumped linear spring K_t and a viscous damping element C_t as shown in the Figure 2.11. The vehicle system is represented by a wheel coupled to the vehicle through a suspension spring (K) and damper (C). For this simple preliminary simulation, it is assumed that vertical motion of vehicle body is negligible, since its contribution to wheel defect-induced impact force is negligible [31]. The wheel with a flat is assumed to roll along the track at a constant forward speed V. W denotes the wheel load due to vehicle weight and represents to 1/8 of the total vehicle load. Vehicle and track are coupled through the contact model proposed in the previous sections.

The equations of motion for the coupled system can be expressed as:

$$\begin{aligned} m_w \ddot{z}_w + C\dot{z}_w + K z_w &= -W + P \\ m_t \ddot{z}_r + C_t \dot{z}_r + K_t z_r &= -P \end{aligned} \tag{2.27}$$

Where m_w is half of the wheelset mass; m_t is track segment mass; z_w and z_r are wheel and rail mass displacements, respectively. P is the contact force developed at the wheel-rail interface which can be calculated using either Hertzian non-linear point contact model or proposed adaptive contact model.

The suspension properties are approximately obtained upon combing the series-coupled primary and second suspension stiffness and damping. Considering that the wheel base of a freight bogie nearly equals to 3 sleeper spans, the length of track is taken as 1.5 times the distance between two sleepers. This highly simplified model is only considered here to examine the effectiveness of the developed adaptive contact model in predicting impact load due to wheel flat when compared to Hertzian non-linear point contact model.

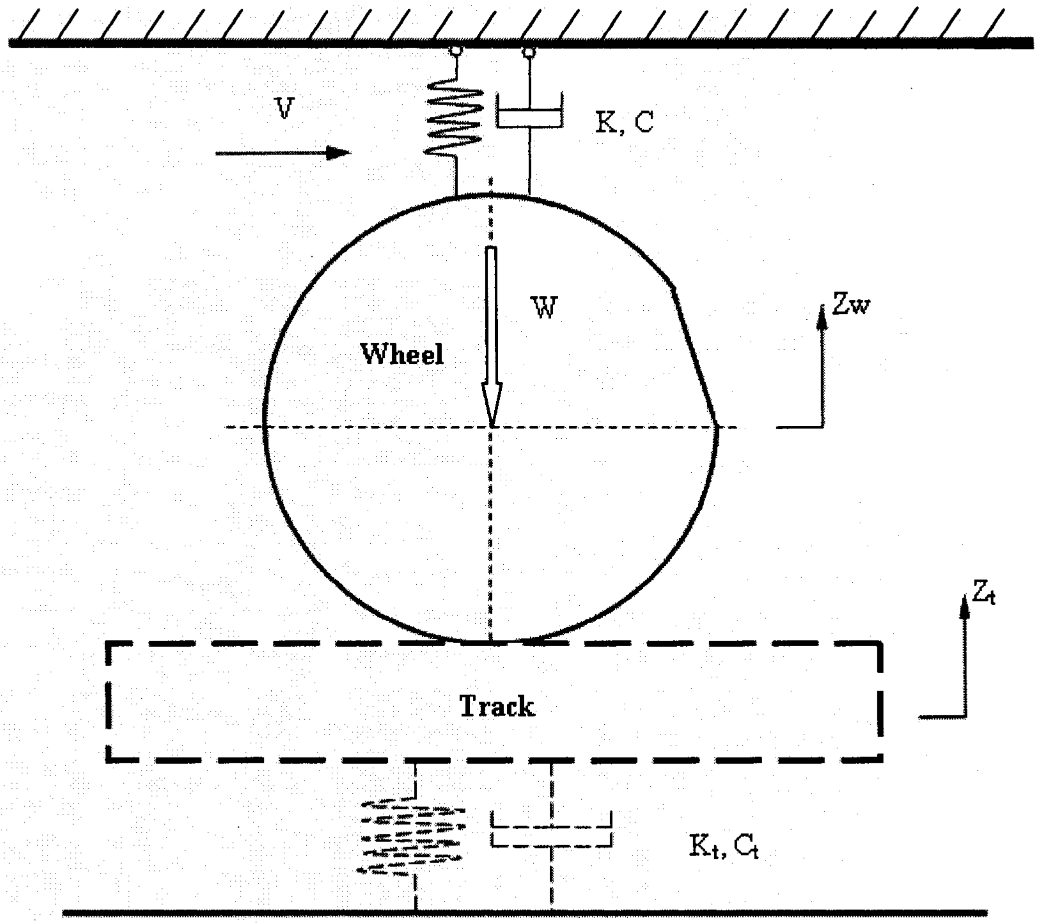

Figure 2.11: Lumped-parameter vehicle track model

2.4.2 Simulation Results

The vehicle, track and wheel defect parameters considered for this simulation are obtained from reference [1]. The parameters are selected to ensure that the wheel traverses a 1.5 sleeper-span track segment, which are listed blow:

<u>Vehicle Parameters</u>

Static wheel load: 82 kN;

Wheel radius: $R_w = 0.4572$ m;

Wheelset mass (half): $m_w = 325$ kg;

Primary suspension properties: K_1 = 788 MN/m, C_1 = 3.5 kN.s/m;

Second suspension properties: K_2 = 6.11 MN/m, C_2 = 158 kN.s/m;

Track Parameters

Mass of unit rail length: 67.57 kg/m;

Sleeper span: 0.65 m;

Track support properties: K_t = 33.3MN/m, C_t = 80kN.s/m;

Wheel Defect

Flat length: l_f = 100 mm;

Flat depth: D_f = 1.5 mm;

Flat initial position: $\beta_o = \pi/2$.

Simulations are performed assuming zero initial rail displacement, $z_r(0) = 0$. the initial wheel displacement is thus taken as the static deformation δ_o and downwards, i.e., $z_{wo} = -\delta_o$.

Figure 2.12 illustrates the simulation results in term of wheel and rail displacement responses to a wheel flat at a forward velocity 50 km/h. The results clearly show that the wheel displacement is larger than that of the rail. The difference represents the overlap or deformation which forms the dynamic contact force. As the wheel flat enters the contact region, there is a sudden drop in the wheel position due to the increasing radial deviation from the nominal wheel radius. During this phase, as the wheel falls downwards, the rail moves upwards to compensate for the missing wheel material. After passing the centre of the wheel flat where the radial deviation starts to decrease and the wheel radius tends to approach the nominal radius, the wheel will continue downwards owing to its great inertia, which causes the rail to do the same. This combined motion of wheel and rail initially causes a reduction in the contact force followed by a sudden peak in the form of an impact. The time history of contact force, derived from the proposed adaptive wheel-rail contact model is shown in Figure 2.13 for three complete revolutions of the wheel. These results clearly reflect the displacement time histories of wheel and rail observed in Figure 2.12. Each time the wheel enters the contact patch, there is an initial drop in the contact force followed by a large sharp impact.

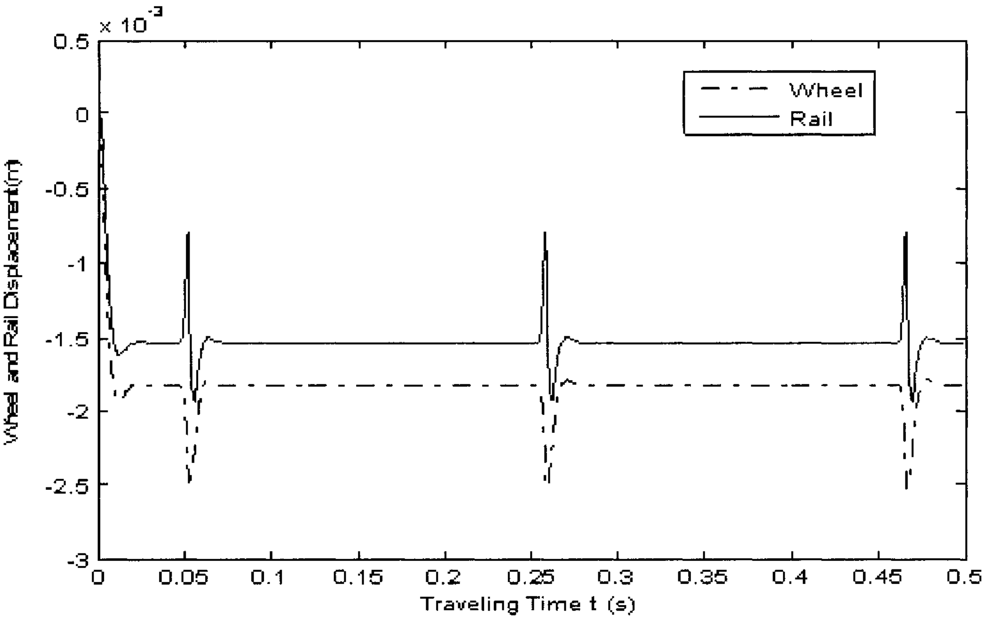

Figure 2.12: Time history of wheel-rail displacements in the presence of a wheel flat

The detailed variation in contact force is presented in Figure 2.14 by considering the impact force for one revolution of the wheel. The results clearly show that the impact force has a very sharp peak with magnitude exceeding 2.5 times the static force. The peak is followed by oscillations of decaying magnitude similar to the response of damped system, and then settles down to the static value within a few cycles. From the results, it can further be noted that the initial drop in contact force may approach zero, suggesting loss of contact of wheel with the rail.

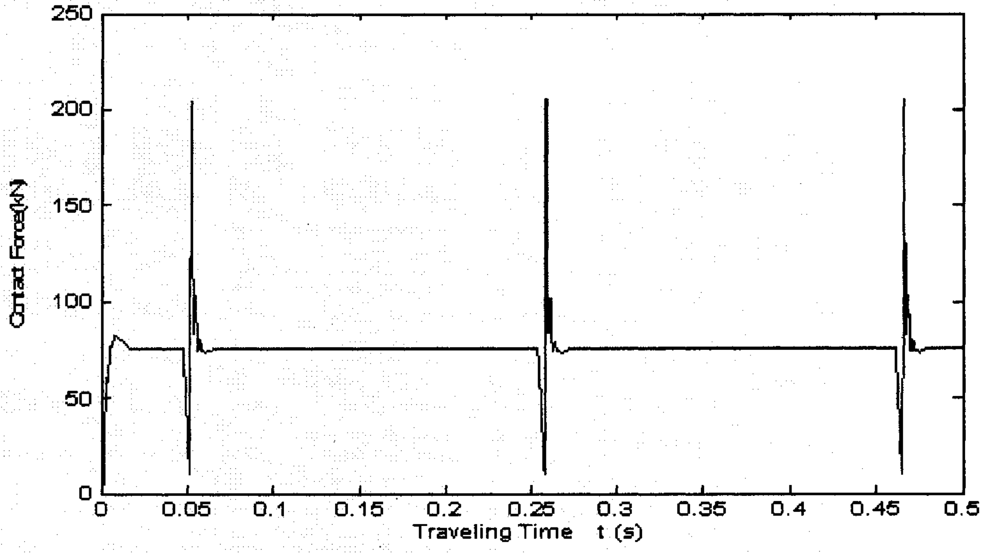

Figure 2.13: Time history of wheel-rail contact force in the presence of a wheel flat (3 revolutions)

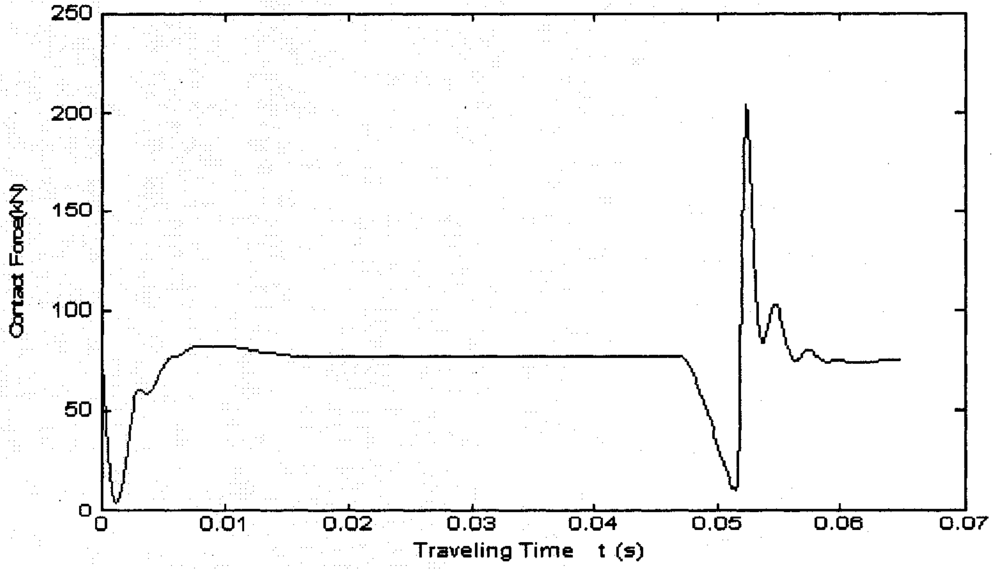

Figure 2.14: Time history of wheel-rail contact force in the presence of a wheel flat

2.4.3 Comparison with Force Response of Hertzian Contact Model

The model, described in Figure 2.11, is further analyzed using Hertzian non-linear contact model. The resulting contact force response is compared with that from adaptive contact model, as shown in Figure 2.15. The comparison exhibits some important differences in the contact force response predicted by the two models. At a forward speed of 50km/h, the peak contact force predicted by adaptive contact model is 206 kN, which is approximately 40% higher than that estimated from Hertzian model (145.4 kN). The results further show that the contact force response of adaptive contact model decreases slowly when flat enters contact region but reaches its peak value more quickly, when compared to that of the Hertzian contact model. The impact force response of adaptive model also decreases very quickly after it reaches its peak value; and the second peak value of contact force tends to be larger magnitude and occurs earlier than that of the Hertzian contact model response. The results also show significant difference in the oscillation frequencies of the contact force. The frequency of fluctuation in the contact force after the impact is 714 Hz for the Hertzian contact model, whereas that of the adaptive contact model is nearly 370 Hz. This may be related to the difference between the state-dependent contact spring stiffness used in two contact models.

The result presented so far are for a forward speed of 50km/h. It is expected that the forward velocity will have a significant effect on the impact force developed due to a wheel flat. A set of simulations are thus conducted in the speed range of 5 to 150 km/h. The peak contact forces referred to a wheel-rail impact force, obtained from both models, are plotted as a function of speed as shown in Figure 2.16. Results suggest that adaptive contact model overestimates the impact force in the lower speed range and underestimates the impact force at higher speeds when compared to the Hertzian contact model. This trend suggest better validity of the adaptive contact model over the Hertzian contact model, since a number of reported studies have indicated that the Hertzian contact model couple with a linear track model underestimates the impact force at low speeds and overestimates the impact force at high speeds [2, 9].

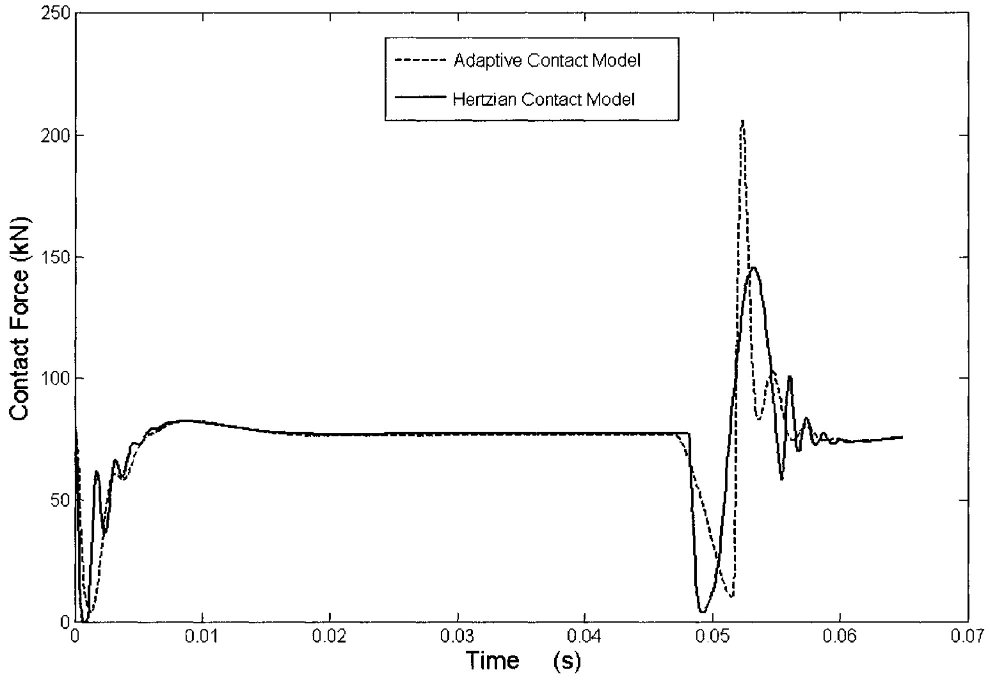

Figure 2.15: Comparison of contact force responses of the Hertzian and adaptive models (speed = 50 km/h)

The adaptive wheel-rail contact model developed in this investigation, however, employs the radial spring stiffness (K_w) on the basis of Hertzian contact coefficient C_H. The effectiveness of the proposed adaptive contact model could be further enhanced through selection of appropriate value fro K_w. Further efforts in identifying K_w would thus be highly desirable.

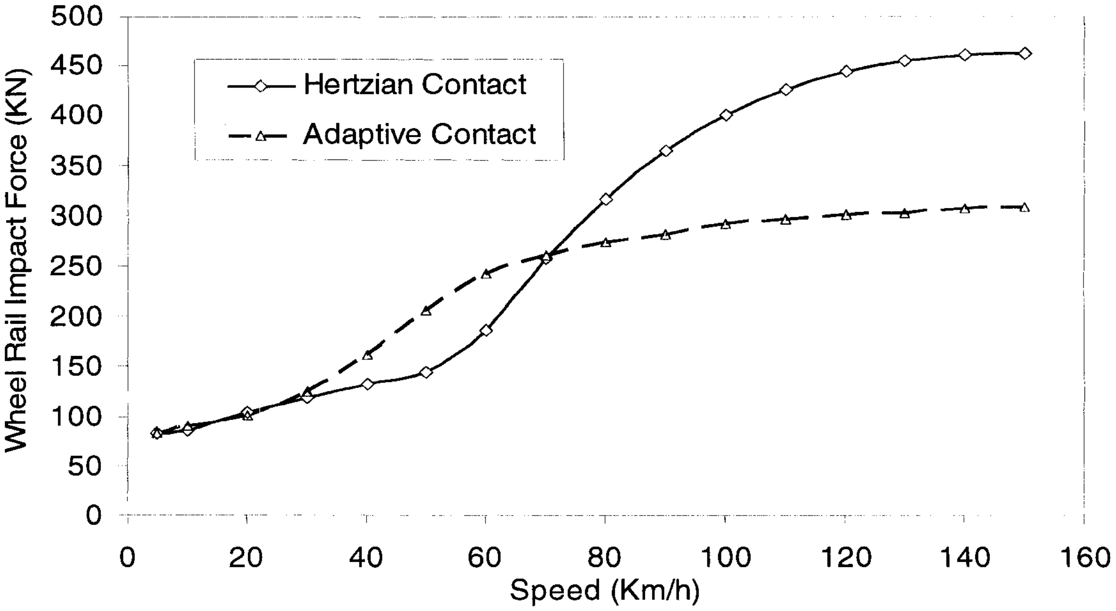

Figure 2.16: Comparison of impact force predicted by adaptive and Hertzian contact model

Owing to uncertainty in K_w, a parametric study is undertaken to study the effect of C_H on the wheel flat-induced peak contact force predicted by Hertzian and adaptive contact models, respectively, in the speed range of 5~160 km/h as shown in Figure 2.17 and Figure 2.18. It can be seen that the impact force response of adaptive contact model appears to be more sensitive to C_H, particularly in the lower speed range. In the published literature, many researchers choice $C_H = 0.8\text{x}10^{11}\sim1.0\text{x}10^{11}$ N/m$^{3/2}$ [9, 29, 41]. Some use $C_H = 0.15\text{x}10^{11}$ N/m$^{3/2}$ [1].

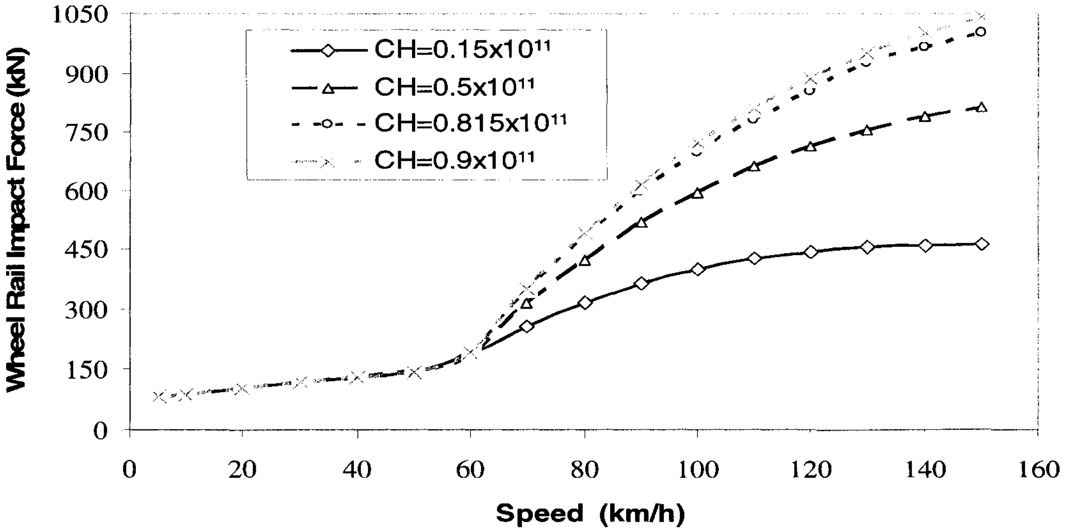

Figure 2.17: Effect of variations in Hertzian coefficient on peak contact force (Hertzian non-linear contact model)

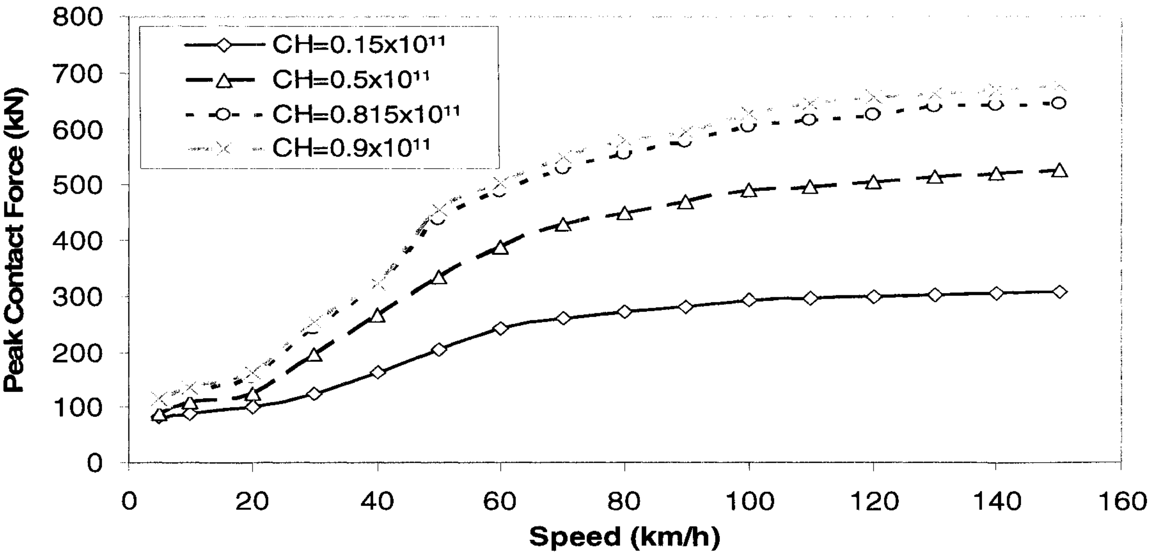

Figure 2.18: Effect of variations in Hertzian coefficient on peak contact force (Adaptive contact model)

2.5 SUMMARY

In this chapter, an adaptive wheel-rail contact model is developed and applied to a simple vehicle track interaction model to simulate impact force due to a wheel flat. This contact model neglects longitudinal and lateral creep forces between the wheel and rail. Lateral movement of wheel is neglected and, therefore, the radius of wheel is assumed constant.

The proposed adaptive contact model incorporates partial contact between the wheel and rail in presence of a wheel defect. Unlike the single or multiple point contact models, the proposed adaptive contact model is based on continuous wheel-rail contact in the contact patch.

Comparison of simulation results obtained from the adaptive contact model with that of Hertzian contact model suggests a more realistic trend in force-time history by the proposed contact model. It has been widely reported that the Hertzian contact model yields an underestimate of the peak impact force at low speeds and overestimate at higher speeds when compared with experimental data. The proposed adaptive contact model yields the opposite trend that is more comparable with the experimentally observed trends.

The study presented in this chapter is for a very simple system to demonstrate the potential and effectiveness of the proposed contact model. The study in this section further showed that radial spring parameter K_w is a critical parameter, which was established based on Hertzian model with static load. An experimentally established value of K_w may further enhance the accuracy of predicted vertical wheel-rail contact force for perfect or defective wheels.

Further improvement in the model may include reliable nominal radius of the wheel as a function of wheelset lateral and yaw motions.

The simulation results, however, was obtained using a simplified model of the vehicle-track system. The proposed model is further analyzed using a more comprehensive track-vehicle system model.

CHAPTER 3

DEVELOPMENT OF THE VEHICLE-TRACK SYSTEM MODEL AND NUMERICAL METHOD

3.1 INTRODUCTION

The magnitudes of impact forces caused by wheel defects are strongly dependent upon vertical dynamics of the coupled vehicle-track system. The analysis of wheel-rail contact force response thus necessitates development of a representative vehicle-track system model in incorporating the contact model. The vertical dynamics of the vehicle-track system is described by considering interactions among four major elements: vehicle, track, wheel-rail interface and wheel rail irregularities. The analytical models of these four elements are generally integrated for analysis wheel-rail interactions in the presence of wheel defects. In this dissertation, the adaptive wheel rail contact model, proposed in chapter 2, is applied to a three dimensional (3-D) model of multiple layers track system in conjunction with roll plane model of the vehicle system. Such formulation permits for analysis of the influence of a wheel defect on the wheel-rail interaction of not only the defective wheel but also the other wheel within the same axle.

Reported studies have invariably concluded that magnitudes of wheel-flat-induced impact forces are most significantly influenced by the track property, while the effect of vehicle system dynamics is relatively small [1]. More efforts have thus been made developing of effective model of the track system, which includes flexible rails, pads, sleepers and subgrade properties. A more common approach based on Timoshenko beam theory is used for modeling the continuous track. The freight vehicle model, on the other hand, is a simplified roll plane model of a bogie with a fixed load representing vehicle body. The model developed is aimed at only vertical wheel-rail dynamic interaction force due to a defined wheel defect, assuming a defect-free track and vehicle motion on a straight track at a constant speed. Longitudinal and lateral relative motions, and creep forces at wheel-rail interface have little effect on the high frequency vertical dynamic responses and are therefore neglected.

Finite element (FE) and generalized mode methods are commonly used to analyze vertical dynamic interactions between railway vehicle and continuous track systems. Generalized mode method, however, can not be used for analysis of wheel-rail dynamic problem based on Timoshenko beam theory, since it involves two independent parameters, namely, transverse deflection and rotational motion. Although finite element method is very versatile and thus widely used in the modeling and simulation of railway track interactions, it poses considerable complexities when adjustments of variations in number of elements within one sleeper span are needed. In order to overcome these limitations, a methodology based on central finite difference method (CFDM) is developed for analysis of the vehicle-track system. This method allows simple means for varying the overall track length and number of grid elements within a sleeper span.

3.2 FREIGHT VEHICLE SYSTEM

A typical railway vehicle, regardless of freight car or passenger car, usually consists of a carbody and two bogies or trucks. Each bogie comprises two wheelsets and the most important subassembly in view of railway vehicle dynamics. Although a number of variations exist in the design of the bogie, it is essentially a frame to house the wheelsets and suspension components. A photograph of a typical three-piece freight bogie is presented in Figure 3.1 [36]. It consists of two sideframes to which the wheelsets are attached through a set of bearing adapters. In some designs, a pad is inserted between sideframe and bearing adapter. Both bearing adapter and pad are always treated as primary suspension of the freight car system. As shown in Figure 3.1, a bolster with a center plate is also supported by the two sideframes through secondary suspension composed of coil springs and friction dampers. Each end of the car body seats on the center plate.

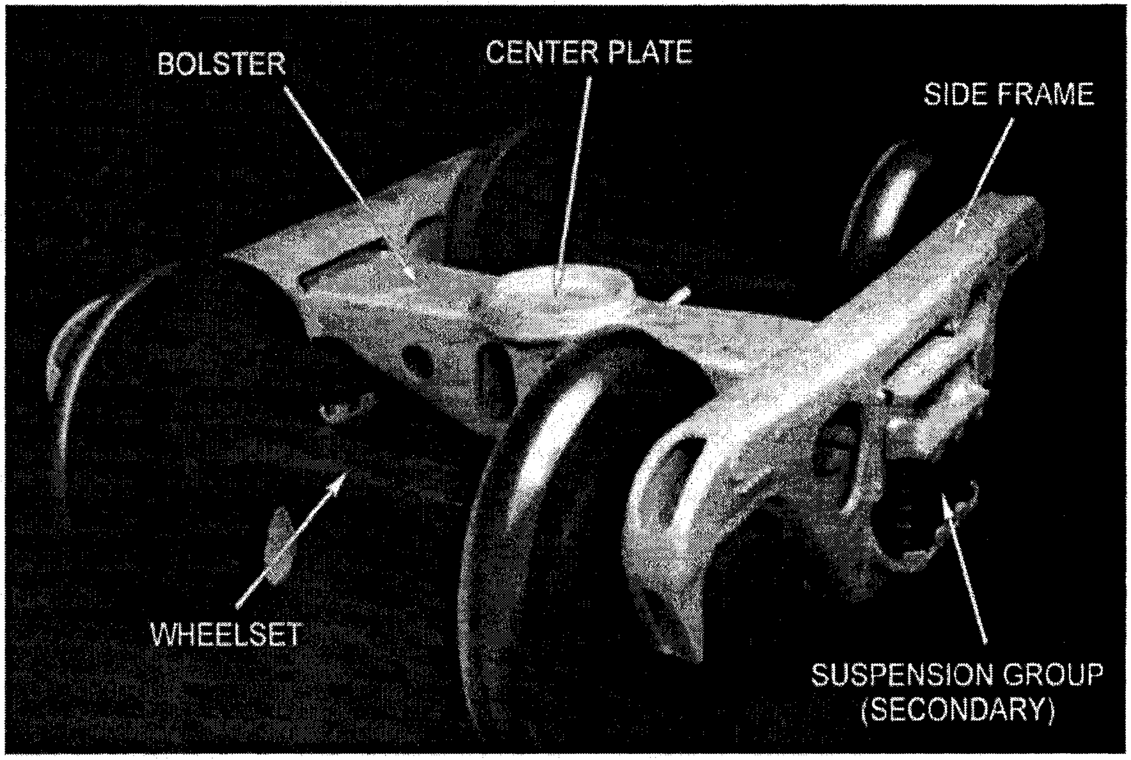

Figure 3.1: A photograph of a typical railway freight vehicle bogie [36]

The railway wheelset is a unique design where two conical or worn wheels are rigidly attached to the axle to form a di-cone configuration. These type profiles cause variations in the effective radii of the two wheels when the vehicle undergoes a lateral motion. Such variations in radii may be considered small under vehicle motion along the track.

3.2.1 Roll-Plane Vehicle Model

The effect of one wheel with defect on the opposite wheel fixed on the same axle is one of the focuses of the present investigation. A simplified roll-plane vehicle model is thus considered appropriate along with a detailed track model. The simplified vehicle model consists of half bolster coupled to two half-sideframes through the secondary suspension and a complete wheelset as shown in Figure 3.2. The secondary suspension is represented by a linear spring constant K_2 and a viscous damping constant C_2. Wheelset is connected to two sideframes via the primary suspension system represented by a spring element K_1 and a viscous damping constant C_1. Load W stands for a quarter of car body weight, and acts on the center of the bolster. P_l and P_r are vertical forces at the wheel-rail contacts at the left and right wheels, respectively. The half-bogie roll plane vehicle model is formulated as a 6-DOF dynamic system model including: the bounce (z_b) and roll (φ_b) motion of the bolster; bounce motion of the left and right sideframes (z_{sfl} ,z_{sfr}); and the bounce (z_w) and roll (φ_w) motion of the wheelset. The model, however, neglects interactions between the leading and trailing wheelsets within a bogie. The contribution of the car body dynamics are also considered to be relatively small due to its low natural frequency.

3.2.2 Equations of Motion of Vehicle System

The six equations of motion for the proposed half bogie roll-plane model can be easily derived using Newton's second law of motion, which are expressed in the matrix form as follows:

$$[M]\{\ddot{d}\}+[C]\{\dot{d}\}+[K]\{d\}=\{F\} \qquad (3.1)$$

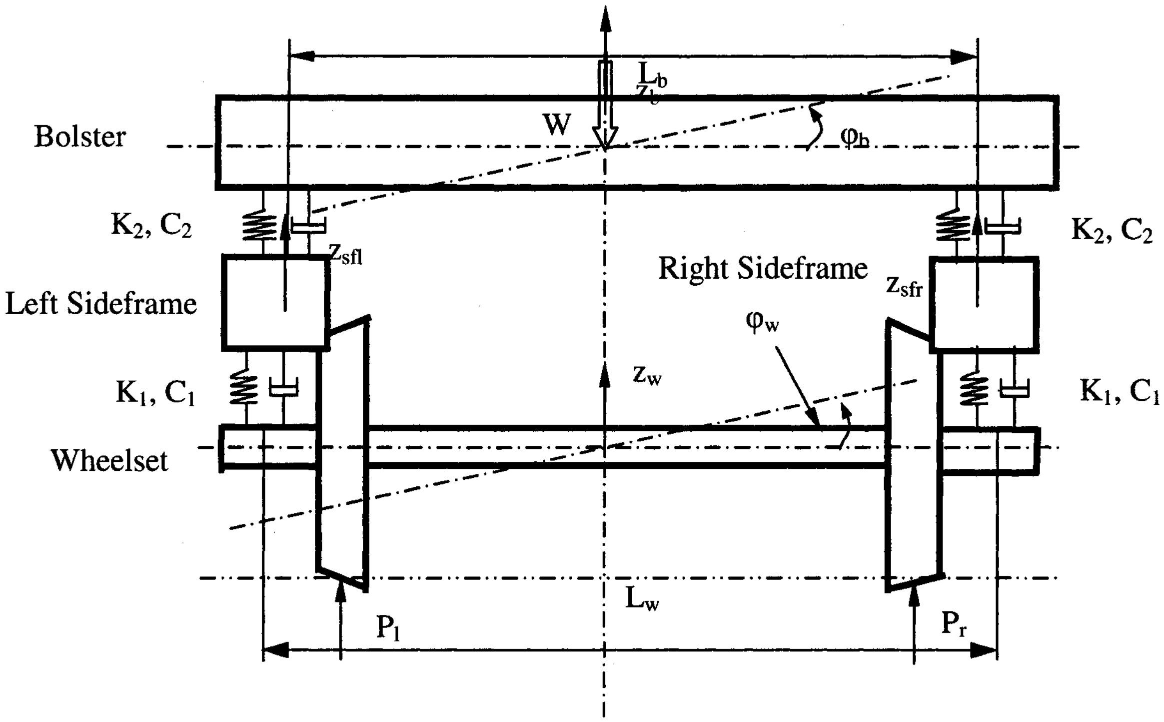

Figure 3.2: Six-DOF roll-plane vehicle

Where $[M]$, $[C]$ and $[K]$ are mass, damping and stiffness matrix, respectively, and vector $\{d\}$ is the displacement vector; $\{F\}$ is the generalized external force vector. These matrics and vectors are summarized in the following:

$$[M]=\begin{bmatrix} m_b & & & & & \\ & J_b & & & 0 & \\ & & m_{sfl} & & & \\ & & & m_{sfr} & & \\ & 0 & & & m_w & \\ & & & & & J_w \end{bmatrix};$$

$$\{d\}=\{z_b, \phi_b, z_{sfl}, z_{sfr}, z_{w}, \phi_w\}^T ;$$

$$[C]=\begin{bmatrix} 2C_2 & 0 & -C_2 & -C_2 & 0 & 0 \\ 0 & \frac{L_b^2}{2}C_2 & \frac{L_b}{2}C_2 & -\frac{L_b}{2}C_2 & 0 & 0 \\ -C_2 & \frac{L_b}{2}C_2 & C_1+C_2 & 0 & -C_1 & \frac{L_w}{2}C_1 \\ -C_2 & -\frac{L_b}{2}C_2 & 0 & C_1+C_2 & -C_1 & -\frac{L_w}{2}C_1 \\ 0 & 0 & -C_1 & -C_1 & 2C_1 & 0 \\ 0 & 0 & \frac{L_w}{2}C_1 & -\frac{L_w}{2}C_1 & 0 & \frac{L_w^2}{2}C_1 \end{bmatrix};$$

$$[K]=\begin{bmatrix} 2K_2 & 0 & -K_2 & -K_2 & 0 & 0 \\ 0 & \frac{L_b^2}{2}K_2 & \frac{L_b}{2}K_2 & -\frac{L_b}{2}K_2 & 0 & 0 \\ -K_2 & \frac{L_b}{2}K_2 & K_1+K_2 & 0 & -K_1 & \frac{L_w}{2}K_1 \\ -K_2 & -\frac{L_b}{2}K_2 & 0 & K_1+K_2 & -K_1 & -\frac{L_w}{2}K_1 \\ 0 & 0 & -K_1 & -K_1 & 2K_1 & 0 \\ 0 & 0 & \frac{L_w}{2}K_1 & -\frac{L_w}{2}K_1 & 0 & \frac{L_w^2}{2}K_1 \end{bmatrix};$$

$$\{F\}=\left\{-W \quad 0 \quad 0 \quad 0 \quad P_l+P_r \quad -\frac{L_w}{2}(P_l-P_r)\right\}^T .$$

Where L_b is lateral spacing between left and right side secondary suspensions and L_w is the distance between left and right wheel bearing centers or primary suspensions, which is assumed to be equal to the distance between left and right wheel-rail contact points.

In order to calculate wheel-rail contact force by the approach developed in chapter 2, it is necessary to establish the vertical displacements of the left and right wheels given by:

Left wheel: $z_{wl} = z_w - \frac{L_w}{2}\phi_w$ (3.2)

Right wheel: $$z_{wr} = z_w + \frac{L_w}{2}\phi_w \qquad (3.3)$$

3.3 TRACK SYSTEM

Railway track system is an important infrastructure in railway industry. The conventional ballasted track consists of two parallel rails supported by cross-track sleepers through rail pads and fasteners at regular spacing as shown in Figure 3.3. Rail-pads are usually synthetic materials that provide cushioning between the rail and sleeper, and serve as electrical isolation between the ground and the rail. As shown in the figure, the sleepers are embanked in position by the ballast. Although some sleepers used are made of solid wood, enhanced pre-stressed concrete sleepers are now widely used in the railway industry. The layer of ground underneath the ballast is the subgrade. When train runs along the rail, the wheel loads are transmitted to a layer of ballast through sleepers and fasteners, and subsequently to the subgrade underneath.

In order to effectively simulate for motions of the track system under a given wheel load, it is necessary to set up the representative models for the flexible track system and its components. There is a wide range of track models that have been reported and used depending on the purpose of the investigation. Comprehensive models of the track components are generally employed for analysis of the vibration wave expansion, while relatively simple track models are considered adequate for analysis of wheel-rail interactions [29]. As it was briefly discussed in the literature review, the rail dynamics have been mostly described using either Timoshenko or Euler beam formulations. Results have shown that both formulations yield comparable results under excitations at low frequencies. Significant differences in the responses predicted by these two theories, however, have been reported in the high frequency range [24].

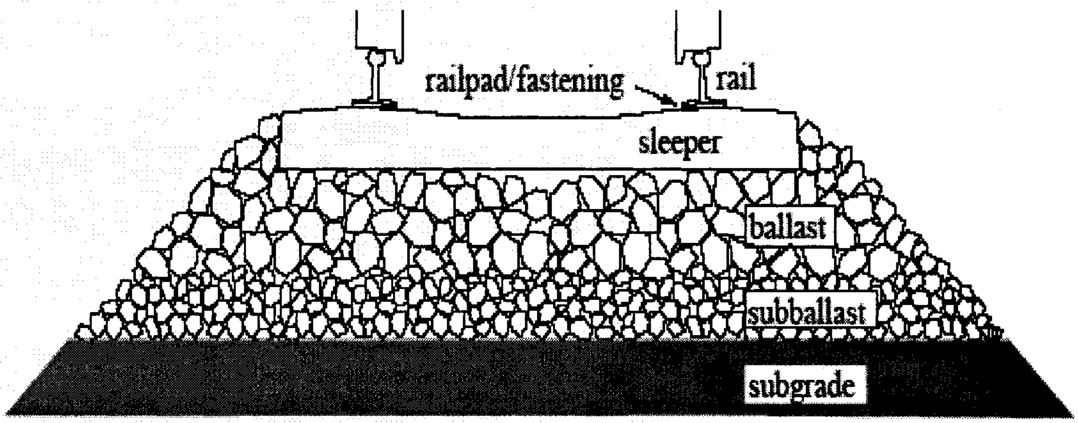

Figure 3.3: A typical railway track and its components [46]

Apart from the rail flexibility, the dynamic motions of the track system are strongly influenced by static and dynamic properties of individual layers, namely, rails, sleepers, ballast, sub-ballast and subgrade. Different studies have considered track models of various layers. Zhai [29] concluded that the wheel-rail interaction forces predicted by a two-layer track model are very similar to those predicted by a three-layer model. A two-layer model, however, tends to predict slightly higher interaction forces at lower frequencies. Furthermore, the motion of the ballast can not be predicted from a two-layer track model.

Apart from the number of layers, the track system model involves careful consideration of track length. The infinite long track is invariably modeled as a track with finite length whose two ends are fixed. The track length and the boundary conditions, however, must be selected to ensure minimal contributions of the boundary conditions to the resulting interface forces and vehicle/track motions.

In this study the wheel-rail impact forces due to wheel defects are the main focus and therefore, a simplified two-layer track model is considered sufficient. The coordinate system used for the track system is shown in Figure 3.4, where the original is assumed to be at the left fixed end.

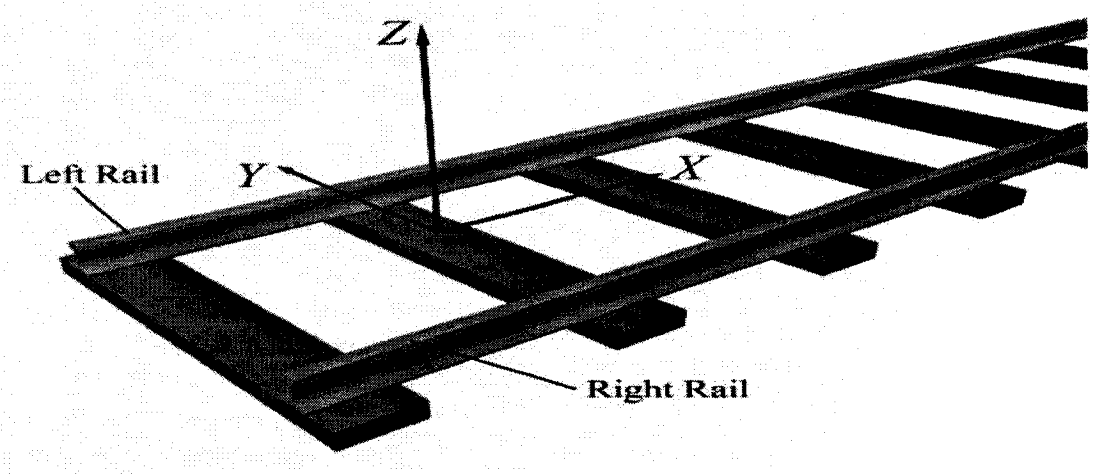

Figure 3.4: The track and its coordinate system [36]

3.3.1 Model of Track System

A 3-D two-layer track system model consisting of left and right rails, pads, sleepers and ballast elasticity is developed, as shown in Figure 3.5. Two rails are modeled as Timoshenko beams supported on the sleepers modeled as lumped masses, through the rail-pads and fasteners that are represented by springs and dampers. The ballast is modeled as springs and dampers inserted between each discrete sleeper and subgrade. The two rails are modeled as thick Timoshenko beams, whose both the rotary inertia and shear deformations are taken into account.

Considering nearly negligible contributions of longitudinal and lateral deformations of the track system, the track system model is simplified to describe its dynamic motions in the vertical plane along. Furthermore, the contribution of the ballast mass to the contact forces is assumed to be negligible. The elastic properties of the ballast, however, are considered and modeled by discrete sets of springs and dampers as shown in Figure 3.5. Finally, the gauge between two rails and sleeper spacing are assumed to be constant along the length of the track. The model is developed to incorporate variable number of sleepers depending on the forward velocity of the train over the track system.

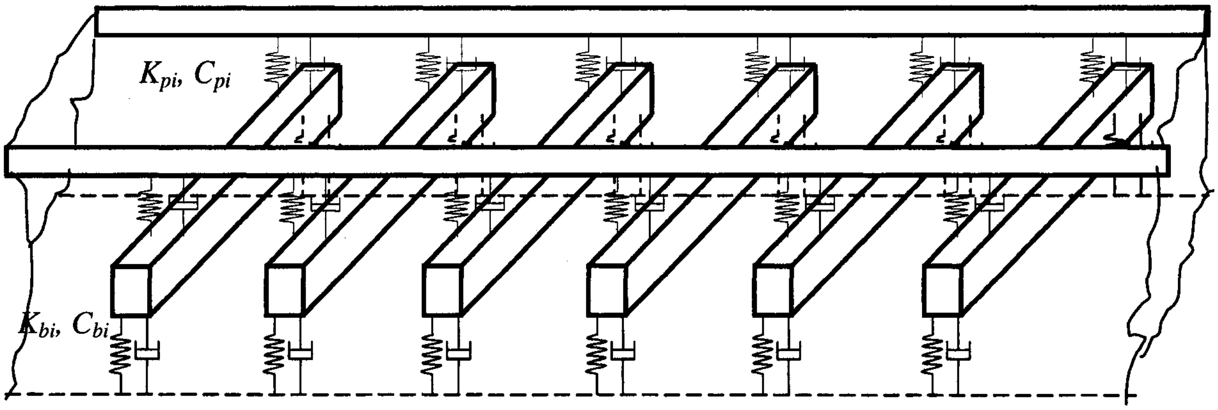

Figure 3.5: Schematic of the two-layer 3D track system model

3.3.2 Equations of Motion of the Track System Model

A rail of length *L*, modeled as Timoshenko beam supported discretely by '*n*' sleepers is shown in Figure 3.6. Both ends of the rail are assumed fixed, where '*a*' denotes the spacing between two adjacent sleepers. P_c and X_w represent the vertical contact load and its location along the rail length. For an element of rail, Timoshenko theory [59] yields following expressions for the vertical force and bending moment:

$$U(x,t) = kAG\left[\frac{\partial Z_{Rl(r)}(x,t)}{\partial x} - \theta_{l(r)}(x,t)\right] \qquad (3.4)$$
$$M(x,t) = EI\,\frac{\partial \theta_{l(r)}(x,t)}{\partial x}$$

Where Z_R and θ represent rail vertical and rotation motions; k is the shear coefficient of rail; A is the cross-sectional area of the rail and G is the shear modulus of the rail material and EI represents the flexural rigidity of the rail.

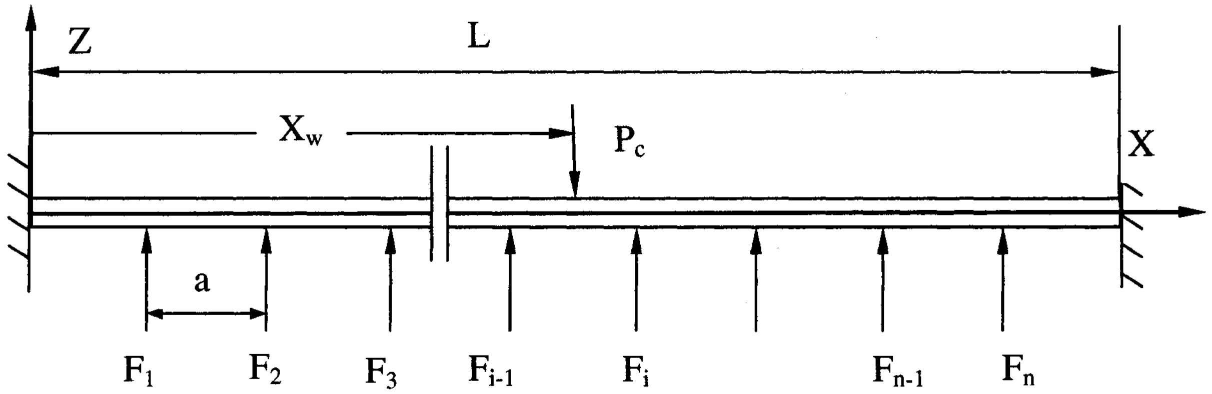

Figure 3.6: Model of rail supported by sleepers (fixed end)

For the rail model with a moving point load P_c and discrete support forces F_i (Figure 3.6), the governing equations for vertical and bending motions can be expressed as [49]:

$$\frac{\partial}{\partial x}\left\{kAG\left[\frac{\partial Z_{Rl(r)}(x,t)}{\partial x}-\theta_{l(r)}(x,t)\right]\right\}-\overline{m}\frac{\partial^2 Z_{Rl(r)}(x,t)}{\partial t^2}=P_{cl(r)}(t)\delta(x-X_w)-\sum_{i=1}^{N}F_{il(r)}\delta(x-ia) \tag{3.5}$$

$$\frac{\partial}{\partial x}[EI\frac{\partial\theta_{l(r)}(x,t)}{\partial x}]+kAG\left[\frac{\partial Z_{Rl(r)}(x,t)}{\partial x}-\theta_{l(r)}(x,t)\right]-\overline{m}r^2\frac{\partial^2\theta_{l(r)}(x,t)}{\partial t^2}+P_a\theta_{l(r)}(x,t)=0$$

Where δ function represents the position of vertical forces on the rail and converts the concentrated forces into distributed forces. Subscript i refers to i^{th} sleeper, and notation $l(r)$ refers to left (right) side rail. $\overline{m}$ is rail mass of unit length. r is the radius of gyration of rail cross-section. P_a is longitudinal force applied on the rail which it is neglected in this study.

As shown in Figure 3.3, the sleepers are supported by ballast which is distributed under the discretely spaced sleepers. Each sleeper may be modeled either as a continuous beam or a lumped mass. Since this investigation focuses on the vertical interaction forces developed at the wheel and rail contact, a lumped mass representation of sleeper is considered appropriate. A set of springs and dampers represent the compliance of the ballast. The lateral distance between two rail supports is L_s as shown in Figure 3.7. The vertical displacement Z_{is} and roll displacement φ_{is} of i^{th} sleeper are derived from the following differential equation:

$$[M_s]\{\ddot{d}_s\}+[C_s]\{\dot{d}_s\}+[K_s]\{d_s\}=\{F_s\}^T \tag{3.6}$$

Where $[M_s]$ is the mass matrix:

$$[M_s]=\begin{bmatrix} m_s & 0 \\ 0 & J_s \end{bmatrix};$$

Where m_s and J_s are the mass and roll moment of inertia of the sleeper.

$\{d_s\}$ is the displacement vector, $\{d_s\}=\{Z_{is},\varphi_{is}\}^T$;

$[C_s]$ is the damping matrix:

$$C_s=\begin{bmatrix} 2C_b & 0 \\ 0 & 2L_{is}^2 C_b \end{bmatrix};$$

Where C_b is the damping due to ballast.

$[K_s]$ is the stiffness matrix:

$$K_s=\begin{bmatrix} 2K_b & 0 \\ 0 & 2L_{is}^2 K_b \end{bmatrix};$$

Where K_b is the stiffness due to the ballast.

In the above formulations, $\{F_s\}$ is the generalized external force vector, given by:

$$\{F_s\}=\{-(F_{il}+F_{ir}) \quad L_s(F_{il}-F_{ir})\}^T;$$

Where $F_{il(r)}$ are the forces due to visco-elastic rail-pad between the left rail and i^{th} sleeper, and the right rail and the i^{th} sleeper, respectively.

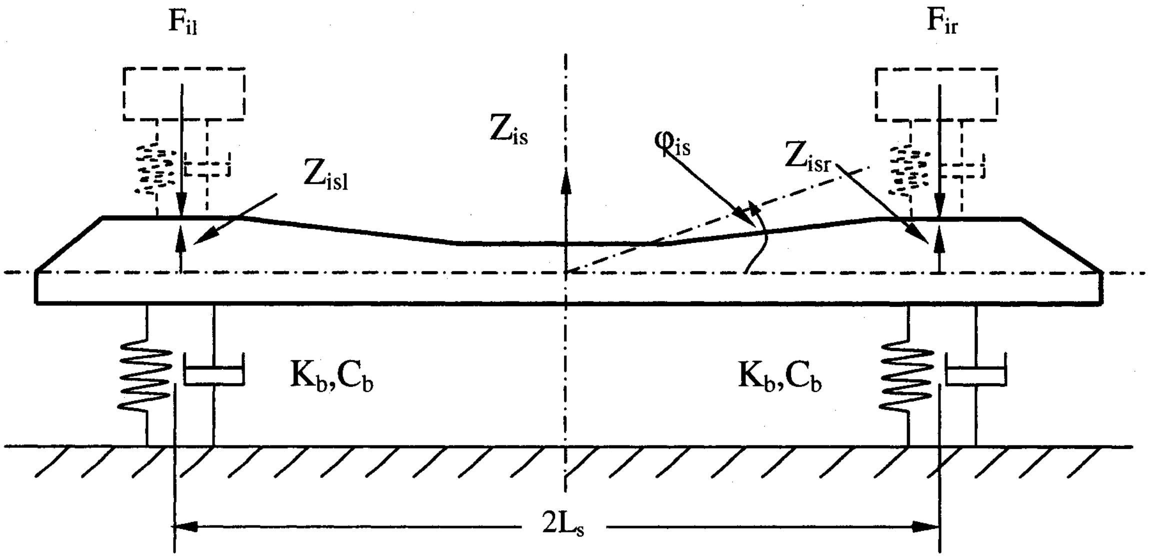

Figure 3.7: Sleeper Modeled as Lumped Mass

Expressing the vertical displacements of sleeper at the left and right pad location by:

$$\text{Left end: } Z_{isl} = Z_{is} - L_s \varphi_{is}\,; \tag{3.7}$$

$$\text{Right end: } Z_{isr} = Z_{is} + L_s \varphi_{is}\,. \tag{3.8}$$

The pad force for the i^{th} sleeper at the left and right rail support can be expressed by:

$$F_{il(r)} = -K_p\left[Z_{Rl(r)}(ia,t) - Z_{isl(r)}(t)\right] - C_b\left[\dot{Z}_{Rl(r)}(ia,t) - \dot{Z}_{isl(r)}(t)\right] \tag{3.9}$$

Where K_p is the pad spring stiffness and C_p is the pad damping coefficient.

3.4 METHOD OF ANALYSIS

Coupled vehicle-track system model developed in the previous section considered the rail as continuous system, while the vehicle and sleeper components are modeled by discrete or lumped mass systems. Mathematically, the model is represented by a set of coupled ordinary (ODE) and partial differential equations (PDE). Furthermore, the total number of DOF for the model can be up to 500 depending on the length of track used in the model. It is thus essential to explore an effective method for analysis of coupled partial and ordinary differential equations with sufficient accuracy and stability of the solution.

There are two basic methods which are usually used in the study of vehicle track dynamic interaction: generalized mode and finite element (FE) methods. The former one transfers the partial differential equations (PDE) to ordinary differential equations (ODE) by converting the natural coordinate system to generalized or normalized mode coordinate system. This method is well-suited when Euler beam theory is used, since the forth order PDE can be easily converted to second order ODE [29, 35, 38]. The FE method transfers the partial differential equations (PDE) into ordinary differential equations (ODE) by dividing the beam into small elements and is mostly widely used in many studies [1, 60, 61, 62].

In this study, a central finite difference method (CFDM) is applied to solve for partial and ordinary differential equations, while the partial differential equations are solved directly.

3.4.1 Numerical Method to Solve Equations of Track System

The track system model represented by a set of PDEs and ODEs, coupled through the interaction force between sleepers and two rails, is solved using a central finite difference method (CFDM). In this method, the displacement of the mass is evaluated from the previous history of displacement at time t_i and t_{i-1} as well as the current external force F_i. For repeated application of the process, a recurrence formula must be established for both rails and sleepers as follows.

Recurrence Formulation for Rail:

In finite difference method, the solution domain is replaced with a finite number of points referred to as grids or mesh points as shown in Figure 3.8. The continuous rail is essentially an initial-boundary condition problem for which the solution at initial time and boundary position are already known, as shown in the Figure 3.8.

The PDE for the rail obtained in equation (3.5) can be rewritten in the following form:

$$\begin{aligned} \frac{\partial^2 Z}{\partial t^2} &= \frac{kAG}{\overline{m}}\left(\left[\frac{\partial^2 Z}{\partial x^2} - \frac{\partial \theta}{\partial x}\right]\right) - \frac{P}{\overline{m}}\delta(x - X_w) + \frac{1}{\overline{m}}\sum_{i=1}^{N} F_i \delta(x - ia) \\ \frac{\partial^2 \theta}{\partial t^2} &= \frac{EI}{\overline{m}r^2}\frac{\partial^2 \theta}{\partial x^2} + \frac{kAG}{\overline{m}r^2}\left[\frac{\partial Z}{\partial x} - \theta\right] \end{aligned} \tag{3.10}$$

Where the subscripts for displacements are neglected.

Defining time and position by:

$$\begin{aligned} t &= t_o + j\Delta t; & j &= 0,\ 1,\ 2\ \cdots,\ J \\ x &= x_o + k\Delta x, & k &= 0,\ 1,\ 2\ \cdots,\ K \end{aligned}$$

At time $t = t_j$ and position $x = x_k$, the vertical displacement of rail is Z_{jk}, and the rational angle is θ_{jk}. From Taylor's series expansion, one can get the representation of central finite difference of the differential terms of equation (3.10) as shown in the following [63]:

$$\begin{aligned} \frac{\partial^2 Z}{\partial t^2}\Big|_{j,k} &= \frac{Z_{(j+1)k} - 2Z_{jk} + Z_{(j-1)k}}{(\Delta t)^2} + O(\Delta t^2); & \frac{\partial^2 \theta}{\partial t^2}\Big|_{j,k} &= \frac{\theta_{(j+1)k} - 2\theta_{jk} + \theta_{(j-1)k}}{(\Delta t)^2} + O(\Delta t^2); \\ \frac{\partial^2 Z}{\partial x^2}\Big|_{j,k} &= \frac{Z_{j(k+1)} - 2Z_{jk} + Z_{j(k-1)}}{(\Delta x)^2} + O(\Delta x^2); & \frac{\partial^2 \theta}{\partial x^2}\Big|_{j,k} &= \frac{\theta_{j(k+1)} - 2\theta_{jk} + \theta_{j(k-1)}}{(\Delta x)^2} + O(\Delta x^2); \\ \frac{\partial Z}{\partial x}\Big|_{j,k} &= \frac{Z_{j(k+1)} - Z_{j(k-1)}}{2\Delta x} + O(\Delta x); & \frac{\partial \theta}{\partial x}\Big|_{j,k} &= \frac{\theta_{j(k+1)} - \theta_{j(k-1)}}{2\Delta x} + O(\Delta x). \end{aligned} \tag{3.11}$$

The CFDM recurrence equation for rail vertical and rotation displacement can now be established by substituting equation (3.11) into (3.10) to yield:

$$\frac{Z_{(j+1)k}-2Z_{jk}+Z_{(j-1)k}}{(\Delta t)^2}=\frac{kAG}{\overline{m}}\left[\frac{Z_{j(k+1)}-2Z_{jk}+Z_{j(k-1)}}{(\Delta x)^2}-\frac{\theta_{j(k+1)}-\theta_{j(k-1)}}{2\Delta x}\right]-\frac{P_j}{\overline{m}}\delta(x-X_W)+\frac{1}{\overline{m}}\sum_{i=1}^{N}F_{ji}\delta(x-ia)$$

$$\frac{\theta_{(j+1)k}-2\theta_{jk}+\theta_{(j-1)k}}{(\Delta t)^2}=\frac{EI}{\overline{m}r^2}\frac{\theta_{j(k+1)}-2\theta_{jk}+\theta_{j(k-1)}}{(\Delta x)^2}+\frac{kAG}{\overline{m}r^2}\left[\frac{Z_{j(k+1)}-Z_{j(k-1)}}{2\Delta x}-\theta_{jk}\right]$$

Which expressed in matrix form is:

$$\begin{Bmatrix} Z_{(j+1)k} \\ \theta_{(j+1)k} \end{Bmatrix}=\begin{bmatrix} \frac{kAG(\Delta t)^2}{\overline{m}(\Delta x)^2} & 2-\frac{2kAG(\Delta t)^2}{\overline{m}(\Delta x)^2} & \frac{kAG(\Delta t)^2}{\overline{m}(\Delta x)^2} & \frac{-kAG(\Delta t)^2}{2\overline{m}(\Delta x)} & 0 & \frac{kAG(\Delta t)^2}{2\overline{m}(\Delta x)} \\ \frac{kAG(\Delta t)^2}{2\overline{m}r^2(\Delta x)} & 0 & -\frac{kAG(\Delta t)^2}{2\overline{m}r^2(\Delta x)} & \frac{EI(\Delta t)^2}{\overline{m}r^2(\Delta x)^2} & 2-\frac{2EI(\Delta t)^2}{\overline{m}r^2(\Delta x)^2}-\frac{kAG(\Delta t)^2}{\overline{m}r^2} & \frac{EI(\Delta t)^2}{\overline{m}r^2(\Delta x)^2} \end{bmatrix}\begin{bmatrix} Z_{j(k+1)} \\ Z_{jk} \\ Z_{j(k-1)} \\ \theta_{j(k+1)} \\ \theta_{jk} \\ \theta_{j(k-1)} \end{bmatrix}$$

$$+\begin{bmatrix} -Z_{(j-1)k}-\frac{P_j(\Delta t)^2}{\overline{m}}\delta(x-X_W)+\frac{(\Delta t)^2}{\overline{m}}\sum_{i=1}^{N}F_{ji}\delta(x-ia) \\ -\theta_{(j-1)k} \end{bmatrix} \tag{3.12}$$

Equation (3.12) indicates that in order to get the solution for time $t = j+1$ at point $x = k$, the solution for points $x = k-1$, k and $k+1$ must be known at a previous time $t = j$, as well as the solution for point $x = k$ must also be known at time $t = j-1$.

The scheme for the solution is shown in the recurrence grid illustrated in Figure 3.8. The method is therefore, not self-starting and appropriated boundary conditions are needed. For the rail problem, both ends of the rail are assumed fixed with zero displacement and rotation.

In order to obtain the displacement of position $x = x_k$ at time $t_{(j+1)}$, it is necessary to know the solution at time step t_j and $t_{(j-1)}$; i.e., if the recurrence starts from $j = 2$, the solution at first time step $j = 1$ is needed. The solution at the first time step can be established using Taylor's series expansions:

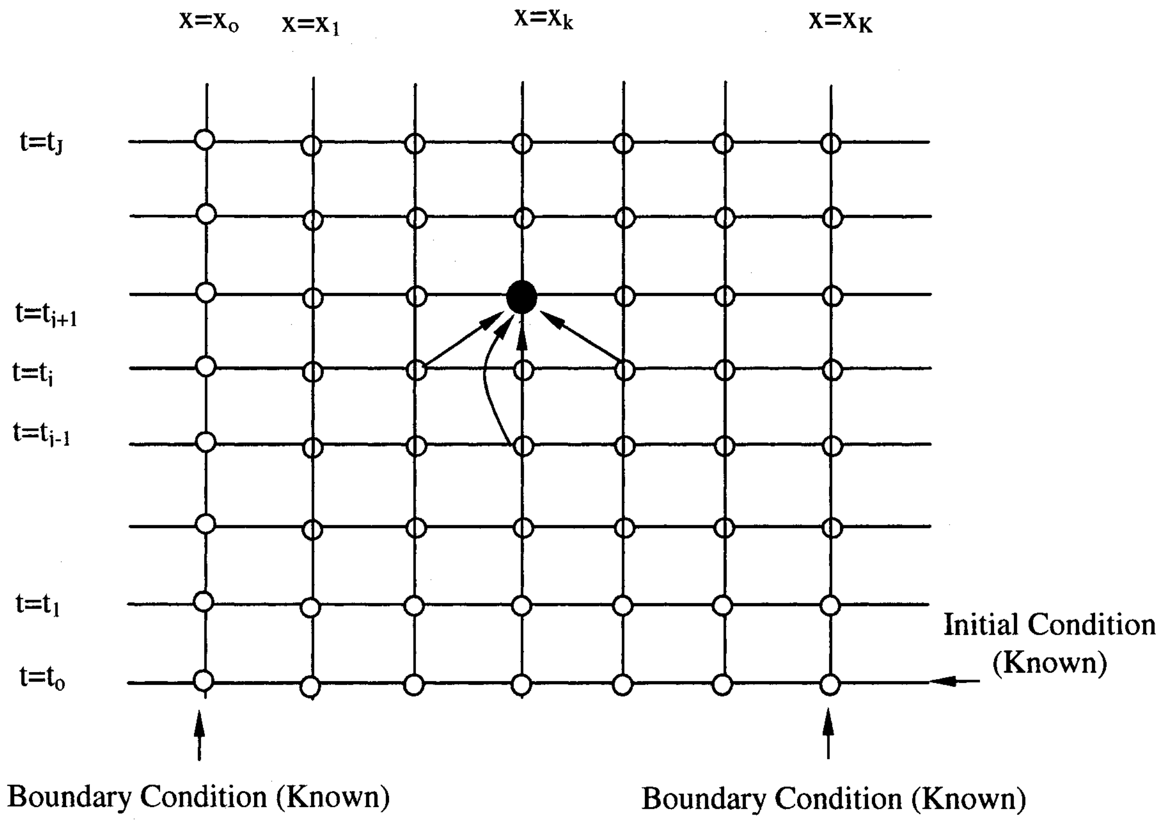

Figure 3.8: Scheme of the recurrence grid of beam (Rail)

$$\begin{aligned} Z_{1k} &= Z_{0k} + \Delta t \dot{Z}_{0k} + \frac{\Delta t^2}{2}\ddot{Z}_{0k} \\ \theta_{1k} &= \theta_{0k} + \Delta t \dot{\theta}_{0k} + \frac{\Delta t^2}{2}\ddot{\theta}_{0k} \end{aligned} \tag{3.13}$$

Where Z_{0k}, θ_{0k} and $\dot{Z}_{0k}$, $\dot{\theta}_{0k}$ are determined by initial condition. The solution at first time step can therefore be obtained if the accelerations at initial time $t = t_o$ are known. Using equation (3.10) and expanding the derivative terms, the acceleration at time t_o can be obtained from:

$$\begin{aligned} \ddot{Z}_{0k} &= \frac{kAG}{\bar{m}}\left[\frac{Z_{0(k+1)} - 2Z_{0k} + Z_{0(k-1)}}{(\Delta x)^2} - \frac{\theta_{0(k+1)} - \theta_{0(k-1)}}{2\Delta x}\right] - \frac{P_0}{\bar{m}}\delta(x - X_W) + \frac{1}{\bar{m}}\sum_{i=1}^{N} F_{0i}\delta(x - ia) \\ \ddot{\theta}_{0k} &= \frac{EI}{\bar{m}r^2}\frac{\theta_{0(k+1)} - 2\theta_{0k} + \theta_{0(k-1)}}{(\Delta x)^2} + \frac{kAG}{\bar{m}r^2}\left[\frac{Z_{0(k+1)} - Z_{0(k-1)}}{2\Delta x} - \theta_{0k}\right] \end{aligned} \tag{3.14}$$

Equation (3.14) rewritten in matrix form is:

$$\begin{bmatrix} \ddot{Z}_{0k} \\ \ddot{\theta}_{0k} \end{bmatrix} = \begin{bmatrix} \dfrac{kAG}{\overline{m}(\Delta x)^2} & \dfrac{-2kAG}{\overline{m}(\Delta x)^2} & \dfrac{kAG}{\overline{m}(\Delta x)^2} & \dfrac{-kAG}{2\overline{m}(\Delta x)} & 0 & \dfrac{kAG}{2\overline{m}(\Delta x)} \\ \dfrac{kAG}{2\overline{m}r^2\Delta x} & 0 & \dfrac{-kAG}{2\overline{m}r^2\Delta x} & \dfrac{EI}{\overline{m}r^2(\Delta x)^2} & \dfrac{-2EI}{\overline{m}r^2(\Delta x)^2}-\dfrac{kAG}{\overline{m}r^2} & \dfrac{EI}{\overline{m}r^2(\Delta x)^2} \end{bmatrix} \begin{bmatrix} Z_{0(k+1)} \\ Z_{0k} \\ Z_{0(k-1)} \\ \theta_{0(k+1)} \\ \theta_{0k} \\ \theta_{0(k-1)} \end{bmatrix}$$

$$+\begin{bmatrix} -\dfrac{P_0}{\overline{m}}\delta(x-X_W)+\dfrac{1}{\overline{m}}\sum_{i=1}^{N}F_{0i}\delta(x-ia) \\ 0 \end{bmatrix} \qquad (3.15)$$

As the equation indicates, the initial acceleration of the k^{th} position at time t_0 can be found from initial displacement of positions k-1, k, k+1. The initial accelerations along with initial condition can then be used to find the displacement at first time instance t_1 using equation (3.13)

Recurrence Formulation for Sleeper

The sleepers governing equation (3.8) can be rewritten in the form:

$$\begin{aligned} \ddot{Z}_s &= -\frac{2C_b}{m_s}\dot{Z}_s - \frac{2K_b}{m_s}Z_s - \frac{1}{m_s}(F_l + F_r) \\ \ddot{\varphi}_s &= -\frac{2L_s^2C_b}{J_s}\dot{\varphi}_s - \frac{2L_s^2K_b}{J_s}\varphi_s + \frac{L_s}{J_s}(F_l - F_r) \end{aligned} \qquad (3.16)$$

Where the subscript to represent ith sleeper is neglected in order to simply the notation.

For the sleeper displacements Z_{sj} and φ_{sj} at time $t = t_j$, the central finite difference expressions of the differential terms are:

$$\begin{aligned} \frac{d^2Z_{sj}}{dt^2} &= \frac{Z_{s(j+1)} - 2Z_{sj} + Z_{s(j-1)}}{(\Delta t)^2} + O(\Delta t^2); & \frac{d^2\varphi_{sj}}{dt^2} &= \frac{\varphi_{s(j+1)} - 2\varphi_{sj} + \varphi_{s(j-1)}}{(\Delta t)^2} + O(\Delta t^2); \\ \frac{dZ_{sj}}{dt} &= \frac{Z_{s(j+1)} - Z_{s(j-1)}}{2\Delta t} + O(\Delta t); & \frac{d\varphi_{sj}}{dt} &= \frac{\varphi_{s(j+1)} - \varphi_{s(j-1)}}{2\Delta t} + O(\Delta t); \end{aligned} \qquad (3.17)$$

Substituting equation (3.17) into equation (3.16) yields:

$$\frac{Z_{s(j+1)} - 2Z_{sj} + Z_{s(j-1)}}{(\Delta t)^2} = -\frac{2C_b}{m_s}\frac{Z_{s(j+1)} - Z_{s(j-1)}}{2\Delta t} - \frac{2K_b}{m_s}Z_{sj} - \frac{1}{m_s}(F_{lj} + F_{rj})$$

$$\frac{\varphi_{s(j+1)} - 2\varphi_{sj} + \varphi_{s(j-1)}}{(\Delta t)^2} = -\frac{2L_s^2 C_b}{J_s}\frac{\varphi_{s(j+1)} - \varphi_{s(j-1)}}{2\Delta t} - \frac{2L_s^2 K_b}{J_s}\varphi_{sj} + \frac{L_s}{J_s}(F_{lj} - F_{rj})$$

Which can be rewritten in matrix form:

$$\begin{Bmatrix} (1+\frac{C_b \Delta t}{ms})Z_{s(j+1)} \\ (1+\frac{C_b Ls^2 \Delta t}{Js})\varphi_{s(j+1)} \end{Bmatrix} = \begin{bmatrix} 2-\frac{2K_b(\Delta t)^2}{m_s} & \frac{C_b(\Delta t)}{m_s}-1 & 0 & 0 \\ 0 & 0 & 2-\frac{2L_s^2K_b(\Delta t)^2}{J_s} & \frac{L_s^2C_b(\Delta t)}{J_s}-1 \end{bmatrix} \begin{Bmatrix} Z_{sj} \\ Z_{s(j-1)} \\ \varphi_{sj} \\ \varphi_{s(j-1)} \end{Bmatrix}$$

$$+\begin{Bmatrix} -\frac{(\Delta t)^2}{m_s}(F_{lj}+F_{rj}) \\ \frac{L_s(\Delta t)^2}{J_s}(F_{lj}-F_{rj}) \end{Bmatrix} \tag{3.18}$$

Similar to the beam problem, the recurrence procedure of sleeper can not self-start. Following the same process described for rail, the sleeper displacement at time $t_1$can be established by using Taylor's series expansion:

$$\begin{aligned} Z_{s1} &= Z_{s0} + \Delta t\dot{Z}_{s0} + \frac{\Delta t^2}{2}\ddot{Z}_{s0} \\ \varphi_{s1} &= \varphi_{s0} + \Delta t\dot{\varphi}_{s0} + \frac{\Delta t^2}{2}\ddot{\varphi}_{s0} \end{aligned} \tag{3.19}$$

Z_{s0}, $\dot{Z}_{s0}$ and φ_{s0}, $\dot{\varphi}_{s0}$ are determined by initial condition. The acceleration terms in equation (3.19) can be obtained from equation (3.16) for time t_0 as:

$$\begin{aligned} \ddot{Z}_{s0} &= -\frac{2C_b}{m_s}\dot{Z}_{s0} - \frac{2K_b}{m_s}Z_{s0} - \frac{1}{m_s}(F_{l0} + F_{r0}) \\ \ddot{\varphi}_{s0} &= -\frac{2L_s^2C_b}{J_s}\dot{\varphi}_{so} - \frac{2L_s^2K_b}{J_s}\varphi_{s0} + \frac{L_s}{J_s}(F_{l0} - F_{r0}) \end{aligned} \tag{3.20}$$

Where F_{lo} and F_{ro} are initial rail-sleeper interaction forces or pad force at the left and right rail-sleeper contact. This pad force for the *i*th sleeper can be easily expressed in terms of rail and sleeper motions as:

$$\begin{aligned} F_{ilj} &= K_p\left[Z_{lj}(ia)-Z_{islj}\right]+C_b\left[\dot{Z}_{lj}(ia)-\dot{Z}_{islj}\right] && \textit{for left side} \\ F_{irj} &= K_p\left[Z_{rj}(ia)-Z_{isrj}\right]+C_b\left[\dot{Z}_{rj}(ia)-\dot{Z}_{isrj}\right] && \textit{for right side} \end{aligned} \tag{3.21}$$

Formulation for Moving Load

The vertical load on the rail due to vehicle is essentially a moving load. As discussed earlier, the CFDM utilizes solution at finite grid points, and hence assumes that load is applied only at the grid. The numerical method therefore, will not account for continuous load although it is defined by delta function. In order to ensure that the moving load is present in the function at all times, an interpolation method is employed in the numerical computational procedure as shown in Figure 3.9, and described in the following.

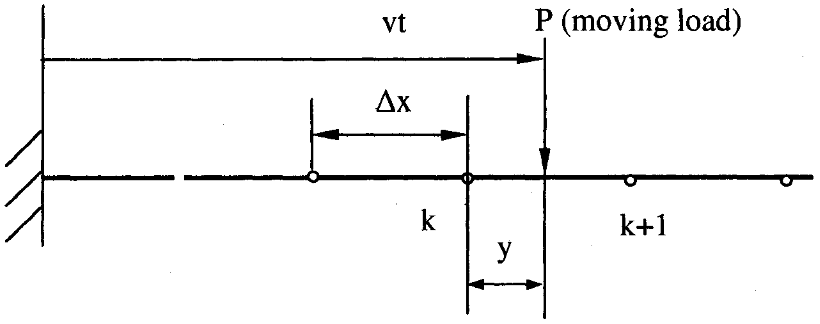

Figure 3.9: Interpolation of Moving Load

In Figure 3.9, *P* represents moving load traveling at a velocity *v*. If the shape function of point *k* is defined by *N1* and that of point *k+1* is defined by N_2, then the load at grid points are:

$$\begin{aligned} P_k &= N_1(y)P \\ P_{k+1} &= N_2(y)P \end{aligned} \tag{3.22}$$

Where $N_1 = 1 - \frac{y}{\Delta x}$, $N_2 = \frac{y}{\Delta x}$, y is the distance from the k^{th} grid point to the force applied point, and $0 \leq y \leq \Delta x$; P_k, P_{k+1} are the equivalent forces to be applied at points k and $k+1$.

Similarly, the displacement of the point where the moving load is applied can be determined by:

$$Z = N_1(y)Z_k + N_2(y)Z_{k+1} \tag{3.23}$$

where Z_k, Z_{k+1} are displacement of point k and $k+1$, respectively.

The track system CFDM formulation representing continuous rails, discrete sleepers and moving load can finally be solved systematically to obtain the response of the track. A program flow chat for the simulation of the track system is presented in Figure 3.10

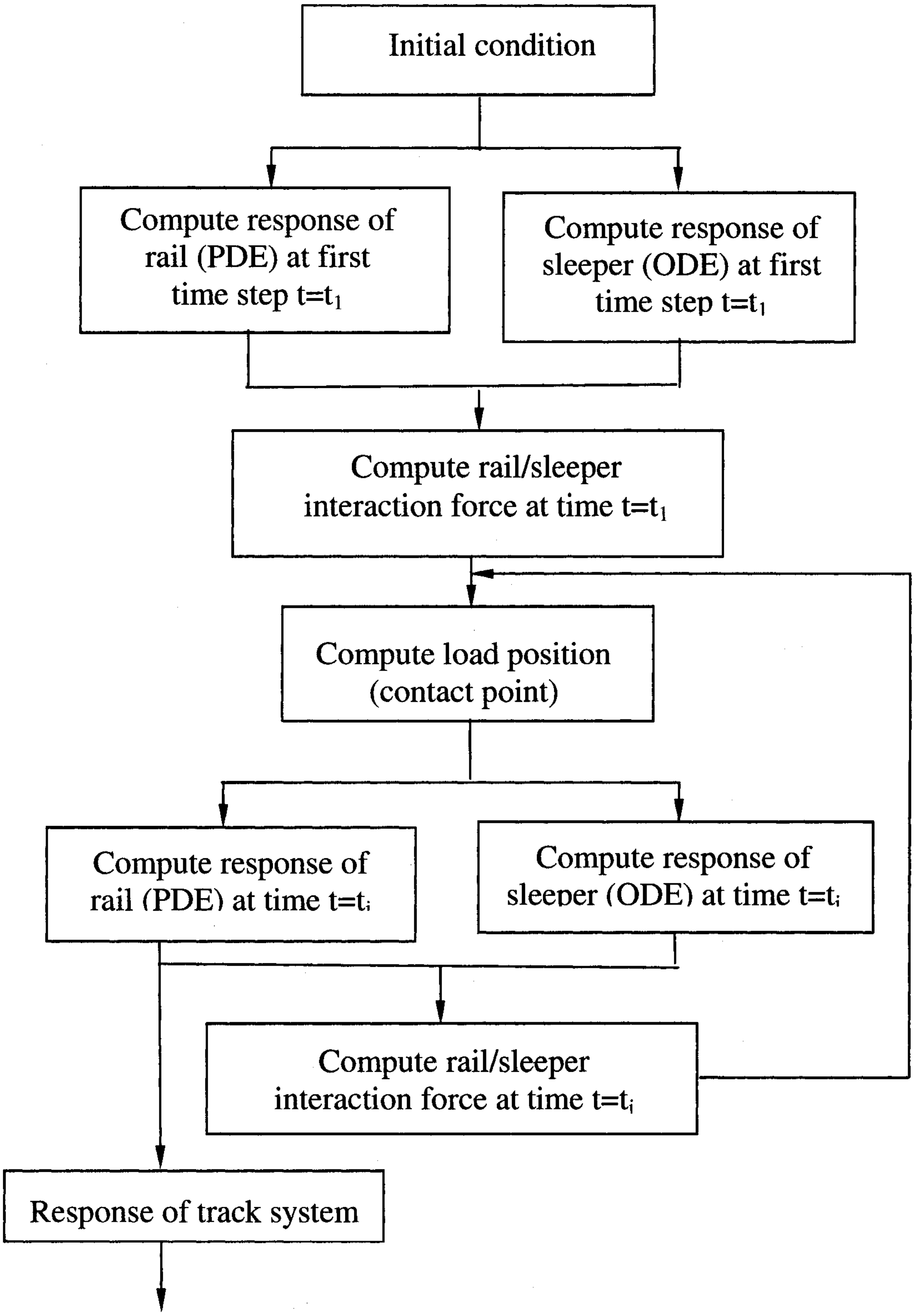

Figure 3.10: Program flow chat of track simulation under moving load

3.4.2 Numerical Method to Solve Equations of Vehicle System

In order to apply CFDM for the coupled vehicle-track system, it is necessary to develop the recurrence expressions for vehicle system equations. The lumped mass vehicle model described in section 3.2 is governed by equation (3.1). This equation of motion can be rewritten in the form:

$$\{\ddot{d}\}=[M]^{-1}\{F\}-[M]^{-1}[C]\{\dot{d}\}-[M]^{-1}[K]\{d\} \tag{3.24}$$

Substituting the expressions for finite difference of the differential terms:

$$\frac{\{d\}_{(j+1)}-2\{d\}_j+\{d\}_{(j-1)}}{(\Delta t)^2}=[M]^{-1}\{F\}_j-[M]^{-1}[C]\frac{\{d\}_{(j+1)}-\{d\}_{(j-1)}}{2\Delta t}-[M]^{-1}[K]\{d\}_j$$

The response vector at $t = t_{j+1}$ can then be established by following formula:

$$\left[I+\frac{(\Delta t)}{2}[M]^{-1}[C]\right]\{d\}_{(j+1)}=(\Delta t)^2[M]^{-1}\{F\}_j+\left[2I-(\Delta t)^2[M]^{-1}[K]\right]\{d\}_j+\left[\frac{(\Delta t)}{2}[M]^{-1}[C]-I\right]\{d\}_{(j-1)} \tag{3.25}$$

Where I is the identity matrix. The above recurrence expression can lead to the solution at time $t = j+1$ as long as the solution at time $t = j-1$ and $t= j$ is known. Similar to the equation (3.18) for sleepers, the response vector for vehicle at time t = $t_1$can be established from response vector at $t = t_0$ using the expression:

$$\{d\}_1=\{d\}_o+\Delta t\{\dot{d}\}_o+\frac{\Delta t^2}{2}\{\ddot{d}\}_o \tag{3.26}$$

where $\{d\}_o$ and $\{\dot{d}\}_o$ are determined by initial condition, and $\{\ddot{d}\}_o$ can be obtained from:

$$\{\ddot{d}\}_o=[M]^{-1}\{F\}_o-[M]^{-1}[C]\{\dot{d}\}_o-[M]^{-1}[K]\{d\}_o \tag{3.27}$$

The adaptive wheel-rail contact model presented in chapter 2 along with the finite difference equations for track and vehicle systems can now be solved simultaneously to determine the response of the track and vehicle system. In the proposed method, an appropriate length of the track with rigid sleepers must be selected to ensure that there is no effect of boundary conditions. Furthermore, the effect of time step Δt must be examined to ensure reliable and stable solution.

3.5 SUMMARY

A 3D model of coupled vehicle-track system is developed to investigate vehicle track vertical dynamic interaction. The sub-models of the entire system, namely, the vehicle system and track system are discussed in detail. Important considerations and assumptions in developing the model include:

- The vehicle is traveling on a straight track at a constant velocity without any lateral motion;
- There is no variation in the rail gauge or the radius of the wheel;
- All the elements of the coupled system are linear except for the wheel-rail interface.

The vehicle model is based on typical North American freight car which uses three-piece bogie as running gear. The basic features are summarized as follows:

- The vehicle model is a simplified 2D roll plan model but can be extended to study 3D problems of vehicle-track vertical interaction. The model can be used to investigate effect of a wheel defect on the other wheel force within the axle;
- The car body is simplified as a “dead weight” and its motion is neglected since the natural frequency of car body (1.5~3Hz) is rather small compared to track and wheel-rail interaction frequency.

The track model is based on popular rail-sleeper-ballast railway track and has following characters:

- The model uses finite long track to model infinite long track. The effect of two ends can be neglected in the middle range of the track as long as the track is of sufficient length;
- Timoshenko beam theory is employed to describe the two rails. The shear deformation, shear force and the rotational inertia of rails are taken into account;
- The track system is modeled as two-layer system, while the sleepers are modeled as rigid body that has mass and mass moment of inertial. The distributed support from ballast is simplified as two point elastic support at the two ends of sleeper;
- Only the elasticity of ballast is taken into account, and the mass of ballast is neglected. So the displacement, acceleration, etc. of the ballast can not be studied in this model.

To facilitate the simulation of coupled subsystems represented by PDE and ODE in time domain, central finite difference method (CFDM) is proposed and formulated in this chapter. The continuous moving contact force is incorporated within the CFDM grid-based solution when the force is located in between. This is achieved by appropriate interpolation of the moving load at two adjacent points. The advantages of CFDM are that it provides time domain solution, as well as the length of track and the element number between two sleepers can be adjusted easily in the simulation program.

CHAPTER 4

MODEL VALIDATION AND RESPONSE OF VEHICLE-TRACK SYSTEM

4.1 INTRODUCTION

Wheel-rail contact model developed in chapter 2, combined with vehicle and track system model developed in chapter 3, along with numerical method formulation, can now be applied to obtain response of vehicle-track system. The primary objective in developing the model is to examine wheel-rail impact force in the presence of wheel defect. A complex model, such as the one developed must, however, be first examined to carry out all possible validation in order to gain confidence in the simulated results. The present chapter is devoted to such effort where simulations are carried out to examine qualitative and quantitative responses of the track system and wheel-rail contact force for perfect wheel rail profile. Such idealized study of the deflection, acceleration, stress and strain, and Failure Mode and Effects Analysis (**FMEA**) in steady-state case is also highly useful for design of the track and vehicle system. Analytical work of the steady-state wheel-rail interaction is also necessary for some special purpose, e.g. noise and effect of vibration on the constructions nearby the railway infrastructure.

Although perfect wheel and rail profile is considered, the discrete feature of sleeper support may introduce dynamic interaction forces between wheel and rail, dynamic deflection and acceleration of track components, and dynamic deformation and acceleration of vehicle parts. These dynamic components are the major source of many problems which the railway transportation industry faces, such as track deterioration, fatigue and noise.

This chapter will focus on the dynamic response of vehicle and track system under steady-state interaction for perfect wheel rail profile. The dynamic characteristics are investigated for constant load moving on the track, and vehicle moving on the track with perfect wheel rail profile. The effect of time step (Δt) on the stability problem introduced by the numerical method as well as effect of CFDM grid distance or length step (Δx) on the simulated results are also discussed.

4.2 RESPONSE OF TRACK SYSTEM WITH CONSTANT MOVING LOAD

A set of first simulation is carried out for a constant load moving on the track system. In this case the problem is same as that of the steady-state response due to a constant load moving on periodical structure, which is a popular example in advanced vibration text book. This section deals with this problem by the model and approach developed in chapter 3. The parameters used in this part of the simulation to represent the track system are presented Table 4.1 [34].

As discussed under numerical method in chapter 3, a length grid (Δx) for the track must be defined. For this simulation, Δx is defined as: $\Delta x = \frac{a}{n}$, where a is the sleeper span and n stands for the length step.

4.2.1 Response of Track Components with Constant Moving Load

The rails and sleepers of the track system will undergo deflection and oscillation as a load moving along the track. The response can be defined as the dynamic deflections of rail and sleeper in vertical plane. A first set of simulation is carried out for a constant load of 100 kN on each rail moving at a constant forward velocity of 50 km/h. This load represents a typical static wheel load for freight car. Two rails of length 13.7 m (20 sleeper spans) supported on 21 sleepers equally spaced every 0.685 m are considered to represent the track system. The simulation is carried out for a grid where the length step parameter n is taken as 2. Therefore the grid point falls on the rail at every sleeper location and in between two sleepers. The simulation time step used is 0.00045 s.

Table 4.1: Parameters of track system

Shear coefficient	0.34
Ballast damping coefficient (*)	50 kN.s/m
Ballast stiffness (*)	40 MN/m
Elastic modulus of rail	2.07×10^{11} N/m
Mass moment of inertia of sleeper	90 kg.m^2
Pad damping coefficient	45 kN/m
Pad stiffness	140 MN/m
Radial spring stiffness	5.3361×10^{10} N/m/radian
Rail cross section area	7.77×10^{-3}m^2
Rail mass per meter	60 kg/m
Rail support distance (*)	1.505 m
Second moment of area of rail about Y axis	2.94×10^{-5} m^4
Shear modulus of rail	81GN/m^2
Sleeper mass	270 kg
Sleeper spacing	0.685 m
Note: The parameters with (*) are not given in reference [34] and are for typical railway track, obtained from other sources.	

The resulting rail deflection as a function of time is presented in Figure 4.1 for both left and right rails. These results show the vertical deflection of the two rails at the moving contact point. It can be seen that the deflection of rails is not effected by the end conditions when the contact point is far enough from the ends. In this case, the effect of two ends is within about 2 seconds or 2.8 m from both ends. This indicates that finite long track model can effectively be employed to simulate the response of an infinite long track system. These results can be readily compared with those obtained by Bajer *et al.* [64], which obtained very similar waveform. A quantitative validation is, however, not possible since all necessary parameters were not presented in [64].

A close-up view of the response between 0.3 s and 0.7 s also presented in Figure 4.1 clearly shows identical behavior of both left and right rail under the constant moving load. The results further show that the rail deflection when the moving load is at a sleeper location is smaller than that when the moving load is at the middle of sleeper span. The waveform produced in these results is a direct result of grid length selected. The computed result of deflection is obtained at the sleeper and mid-sleeper locations, while other values are by interpolation.

The time history of the dynamic response of the rail at a point close to the center along the track length is plotted in Figure 4.2. The response shows that when the moving load is far from the middle point of rail, there is no vertical deflection at this point. As the moving load approaches middle point of rail, this point of rail first moves up slightly prior to reaching its peak deflection when the moving load is at the middle point of the rail. The vertical deflection becomes smaller and smaller as the load is moved away from this point.

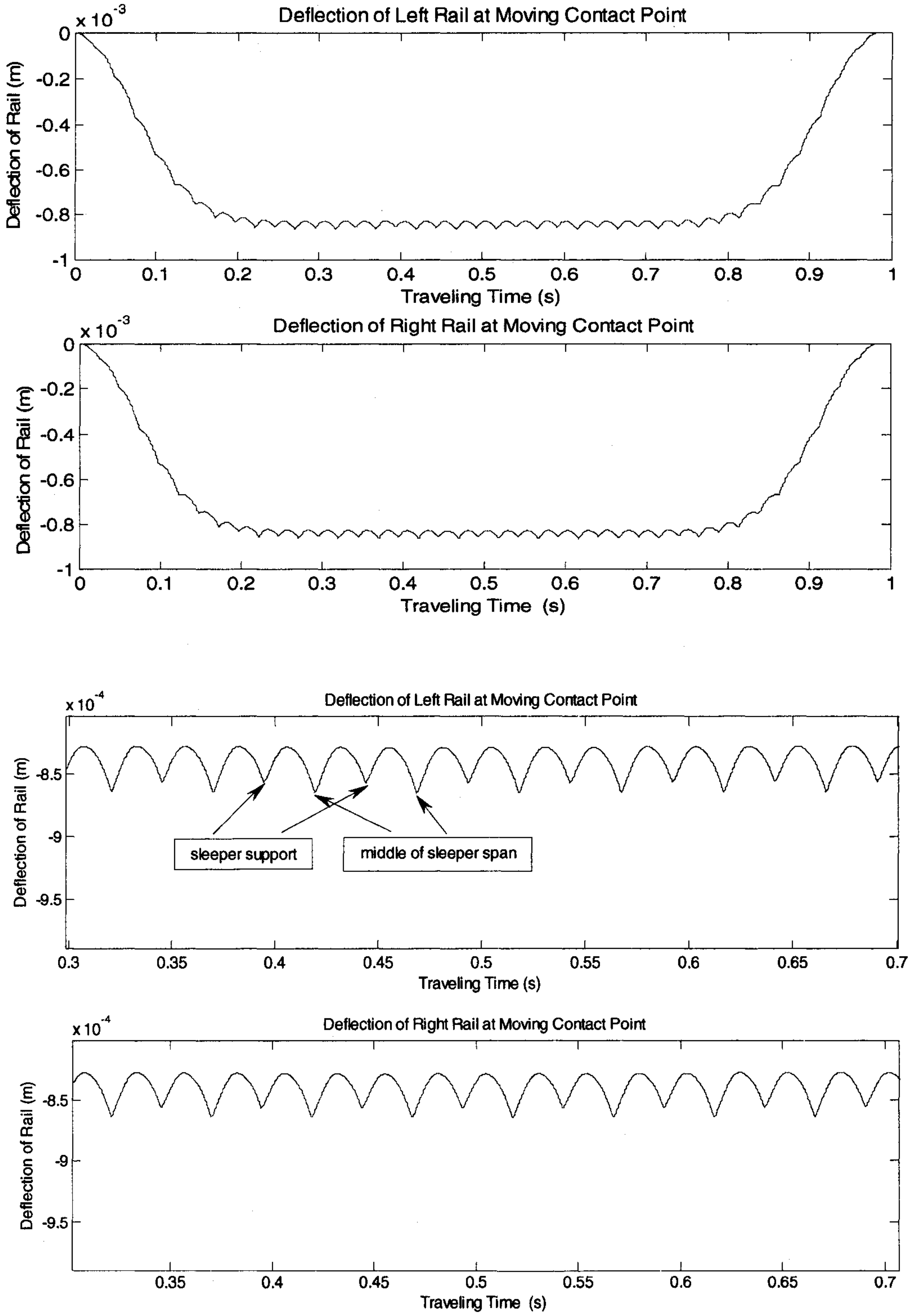

Figure 4.1: Time history of rail vertical deflection at moving contact point

Figure 4.2 also indicates that the load acting on one point of the rail has effect on a zone around this point. This indicates that if a bogie with two axles is considered, the deflection of rail under each wheel will be slightly larger than those predicted by one wheel. It is also confirmed when the results are compared with other studies [1] that considers a pitch plane vehicle model.

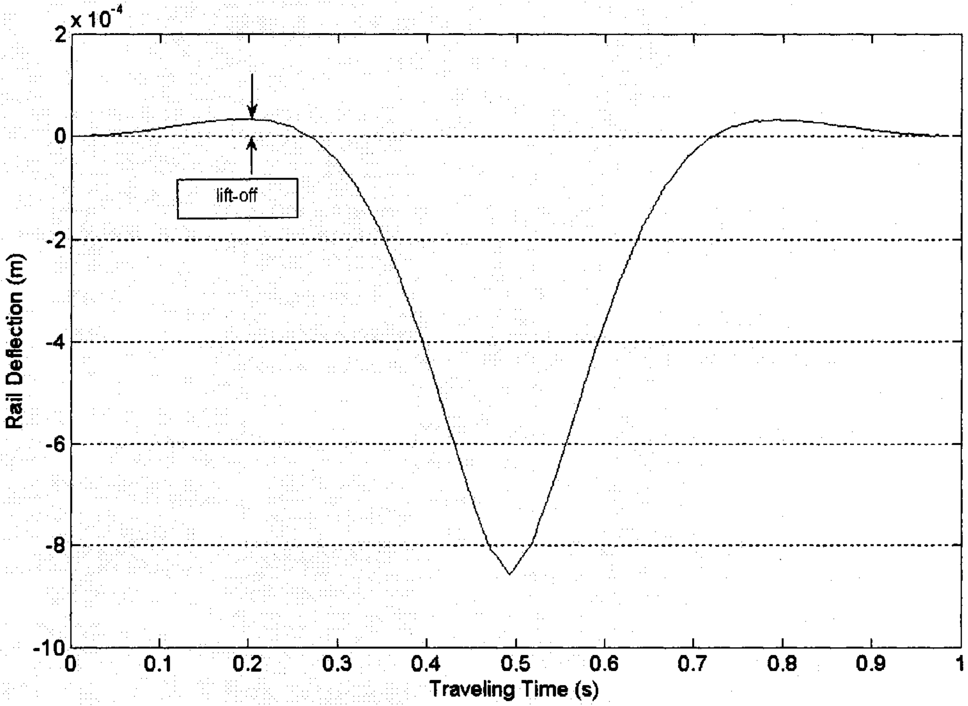

Figure 4.2: Time history of rail vertical deflection at middle point

The response of the left end of the middle sleeper is illustrated in Figure 4.3. It can be seen that the sleeper is unaffected when the moving load is far from it. As the moving load approaches the middle sleeper, it tends to move up slightly from the ballast and then reaches its peak magnitude of downward displacement when the load reaches the point. This trend observed from the sleeper is very similar to that of the rail.

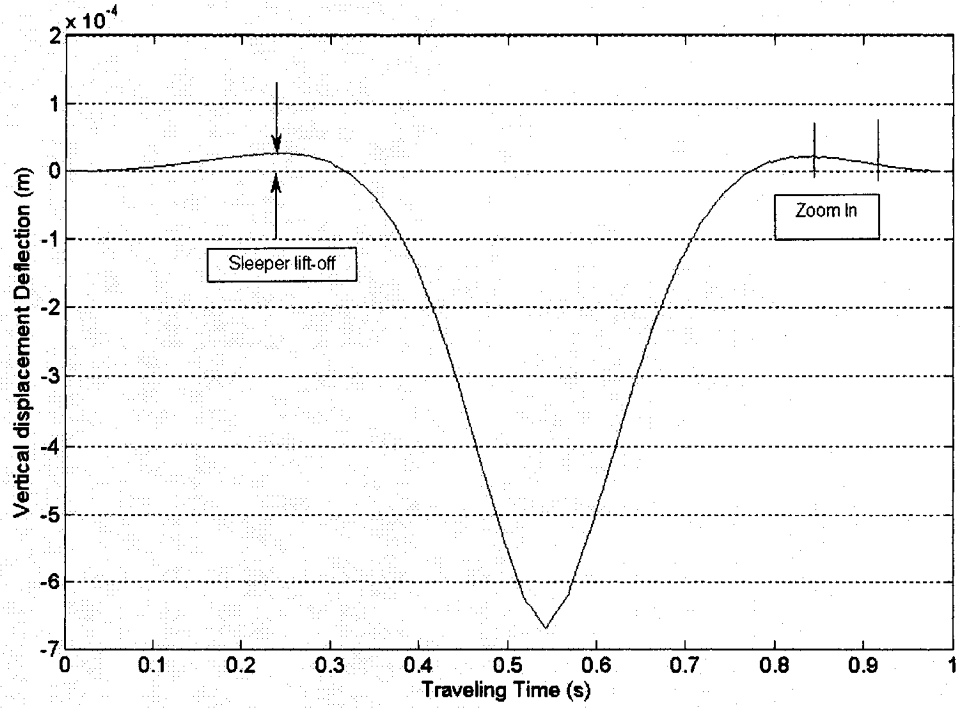

Figure 4.3: Time history of vertical displacement of left end of middle sleeper

A close-up view of the zone in Figure 4.3 is shown in Figure 4.4. As the result indicates, the sleepers go through an oscillating motion as the load moves away form the sleeper. The frequency of the sleeper oscillation from Figure 4.4 is estimated to be around 80 Hz, which is the bounce natural frequency of the sleeper.

Comparison of rail and sleeper displacement presented in Figure 4.2 and 4.3 indicates that the primary element for rail displacement under a load is the displacement of sleeper, while the rail displacement with respect to sleeper at the mid-sleeper span is rather small.

4.2.2 Effect of Simulation Parameters

The rail and sleeper deflection response presented so far were obtained for a constant moving load of 100 kN traveling at a speed of 50 km/h. The track was assigned zero initial conditions. Parameter *n* to define length step (Δx) was 2, and time step (Δt) used was 0.00045 s.

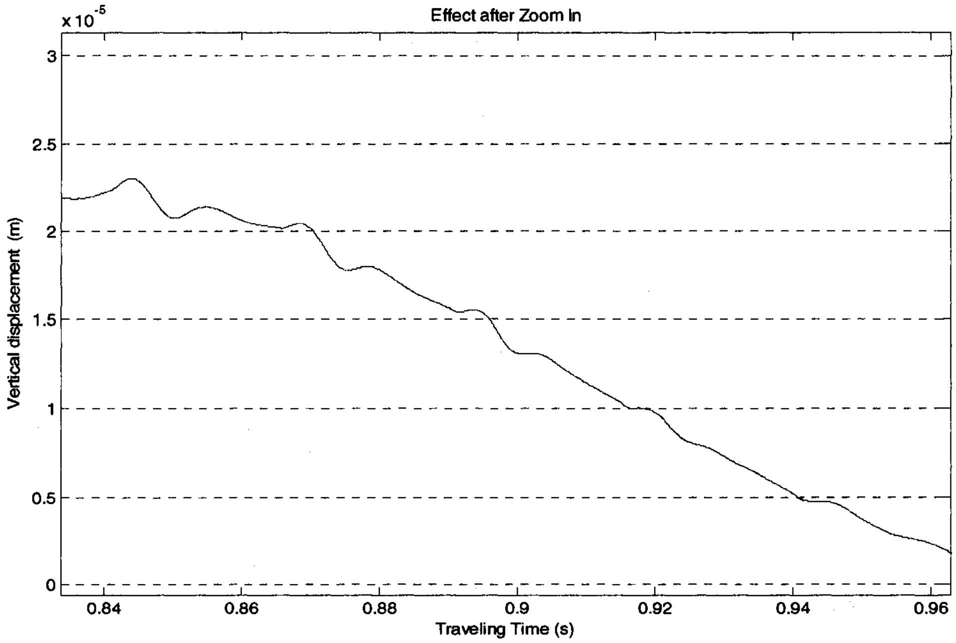

Figure 4.4: Time history of vertical displacement of left end of middle sleeper

In further validation attempt, influence of some of the simulation parameters such as initial condition, forward speed of moving load, time step Δt and length step Δx or the value of *n* is next examined in this section.

Initial Condition

The response of the rail at moving contact point with an initial condition is plotted in Figure 4.5. The left rail has been assigned an initial condition of 5mm static vertical deflection at any point except the two boundary ends. The simulation is carried out for all other parameters same as the previous section. The simulation result indicates that the initial condition has influence on the deflection of contact point when the load just starts to move on the rail, but has no influence on the deflection when the moving load is far away from the starting point. As shown, the damping in the track system stabilizes the vibration component resulting from the initial conditions within a very short period of time.

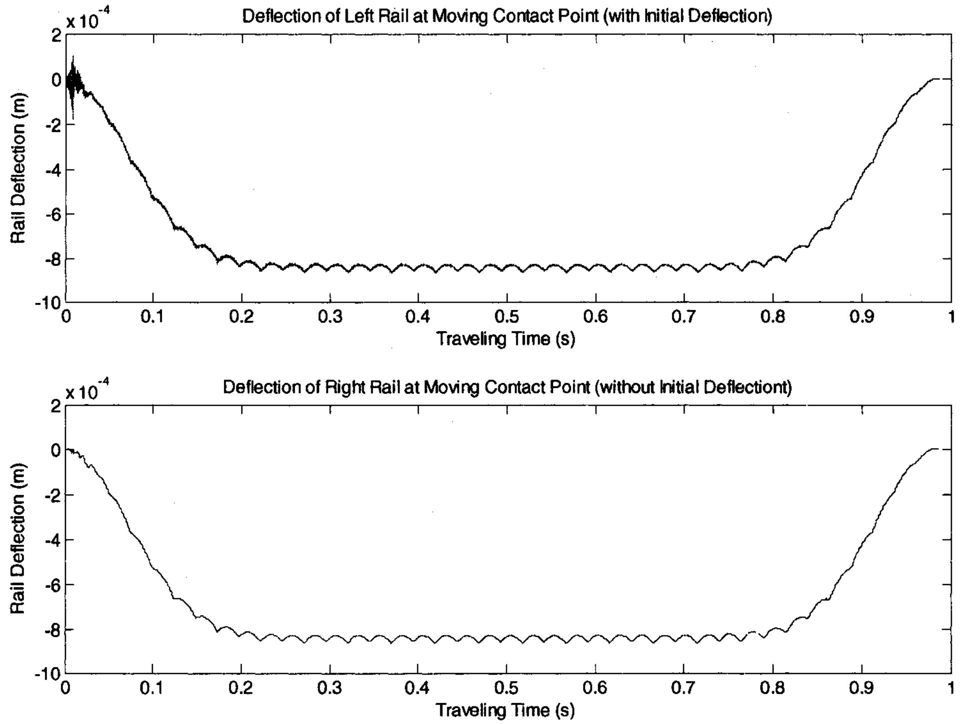
Deflection of Left Rail at Moving Contact Point (with Initial Deflection)

Deflection of Right Rail at Moving Contact Point (without Initial Deflectiont)

Figure 4.5: Time history of rail deflection at moving contact point with initial condition

The results further show that the initial condition assigned to the left rail hardly has any effect on the right rail response. This result further confirms that the feasibility of using a finite long track to model infinite long track system.

Finite Difference Step

Appropriate time step Δt and length step Δx are the important simulation parameters to ensure stable and convergent solution when numerical method is used to solve the PDEs and ODEs. The accuracy of the solution is also determined by the time step and length step used. In this subsection, only the effect of Δt and Δx on the dynamic response of the coupled vehicle-track system is examined. An in-dept discussion on the influence of these parameters can be found in [63].

Time step Δt

For a given length step Δx and track parameters, there exits a critical value of time step, Δt_c. A value of time step larger than Δt_c will result in unstable solution. For the track parameter listed in Table 4.1 and length step parameter $n = 2$, the critical Δt_c is established as 0.000046 s. Displacement of a rail at contact point obtained from simulation carried out at 50km/h with critical time step $\Delta t_c = 0.000046$ s is shown in Figure 4.6. As shown, this value of time step leads to a stable solution. When a value of $\Delta t = 0.000047$ s was used, the solution became unstable with 1 second of simulation time.

For different values of length step parameter n, the values of critical time step Δt_c is next established for the track parameter listed in Table 4.1. The results are summarized in Table 4.2. It is clear shown that smaller length step Δx induces a smaller value of critical time step Δt_c which is required for the solution to be stable.

Such trend in the dependency of Δt_c on the Δx is expected. It is reported in the book *Numerical recipes in FORTRAN* [63] that the solution of the hyperbolic PDE $(\frac{\partial^2 u}{\partial^2 t} = v^2 \frac{\partial^2 u}{\partial^2 x})$ is stable only when the following condition is satisfied:

$$\frac{|v|\Delta t}{\Delta x} \leq 1.$$

Thus as Δx is reduced, the Δt must also be reduced to ensure a stable solution.

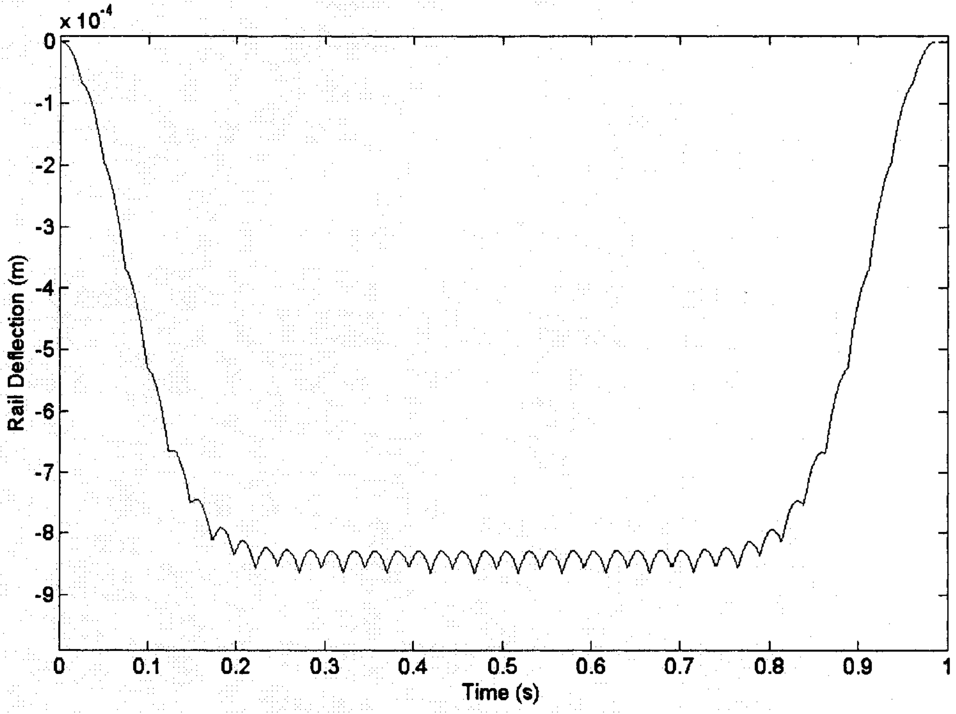

Figure 4.6: Time history of rail deflection at contact point with critical time step

Table 4.2: Relationship between critical time step Δt_c and length step Δx

n ($\Delta x=a/n$)	1	2	3	4	5	10
Δt_c (s)	0.000058	0.000046	0.000036	0.000029	0.000024	0.000013

Length step Δx

As pointed earlier, the numerical CFDM used for the solution in this investigation computes the response only at the grid points. The grid points are defined along the rail by the length step Δx which in this case is further defined by a/n where a is the spacing between adjacent sleepers. Therefore, when n = 1, the response are computed only at the sleeper location. When n = 2, the response are computed at the sleeper location and at the sleeper mid-span. It should be further noted, that as explained in chapter 3, the response at points other than the grids are obtained by interpolation. The simulated results for n = 1, 2 and 3 with appropriate value of Δt as given in Table 4.2 are shown in Figure 4.7.

This results show that reducing the length step can reduce the undulation of the response of rail deflection. It, however, does not influence the mean value of the response. This means refining length step can not increase the computational accuracy. So it is not necessary to use very small length step Δx in the simulation.

However, if critically analyzed, it can be seen that peak deflection of rail at sleeper support predicted for $n = 1$ is 0.835 mm, whereas the peak deflection at sleeper support and sleeper mid-span are 0.856 mm and 0.864 mm respectively when $n = 2$. For $n = 3$, the peak deflection at sleeper support and two points within sleeper span are 0.834 mm and 0.839 mm, respectively. It should be further noted that when $n = 3$, the rail deflection in the middle point between two adjacent sleepers is not the peak value as there is no grid at the mid-span.

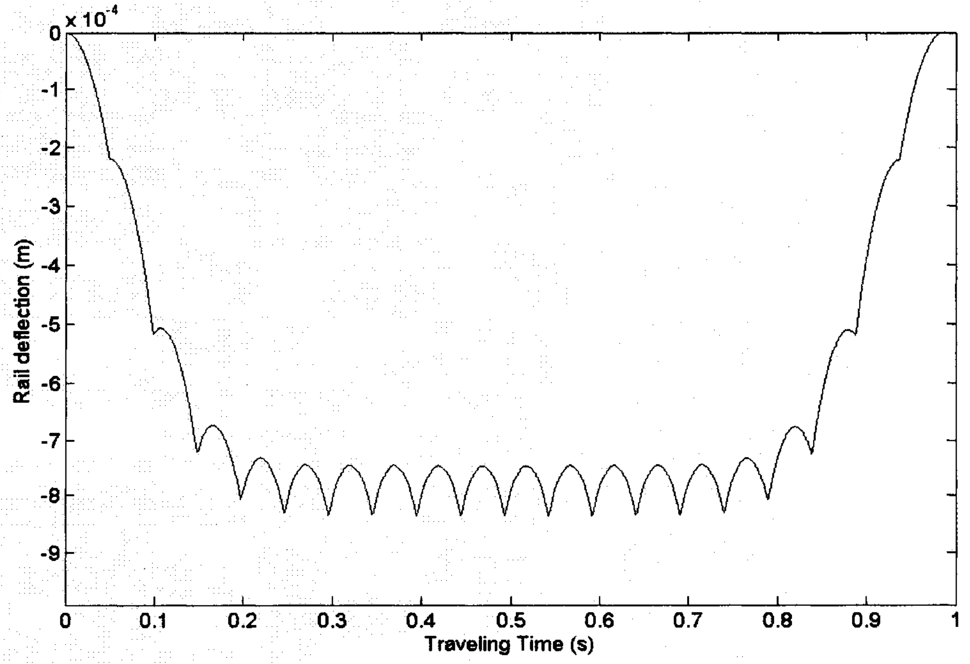

(n=1)

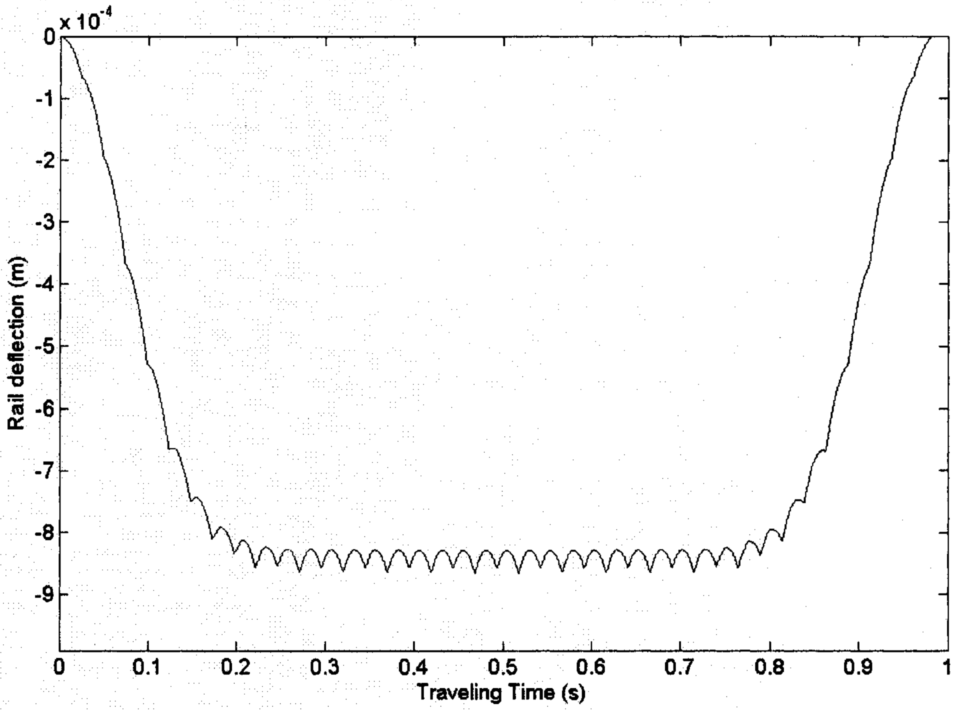

(n=2)

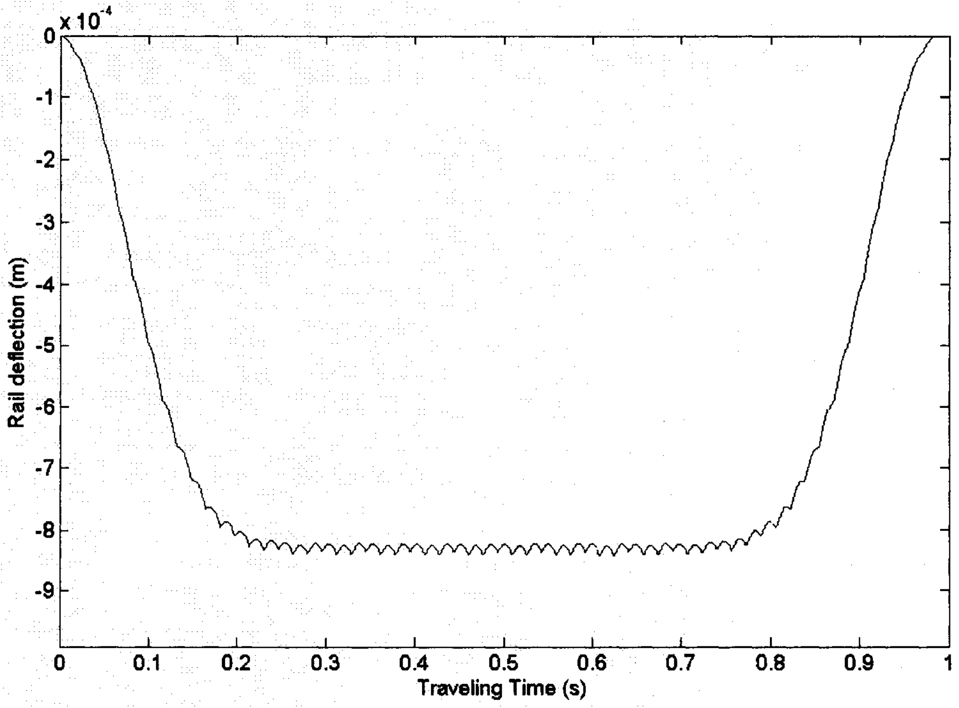

(n=3)

Figure 4.7: Effect of length step on simulation result

In summarizing these results it can be concluded that $n = 1$ is not adequate since it can not provide rail response at locations other than sleepers. $n = 2$ will provide the rail response at the sleeper location as well as the mid-span of sleepers. Although large n will provide a more refined response, larger n with smaller required Δt_c will demand unacceptable computing time for simulation of such large system.

Speed of Moving Load

The effect of the speed of moving load on the rail deflection is next studied. The simulation parameters used are same as those used in the previous section except $n = 1$ is used to ensure stable solution to save simulation time. The maximum steady-state rail deflection at different speed is obtained from each time history and listed in Table 4.3. From the results it can be concluded that the forward speed has some influence on the deflection of rail if a fixed value of n is used. The value of deflection decreases with an increase in the speed. The difference found, however, is quite insignificant.

Table 4.3: Stable maximum deflection at different moving speed
($N = 20$, $n = 1$, $\Delta t = 0.00002$ s)

V(km/h)	5	10	30	50	100	150	200	250	300
Max Deflection (mm)	0.8386	0.8383	0.8380	0.8376	0.8366	0.8361	0.8335	0.8313	0.8303

4.3 DYNAMIC RESPONSE OF COUPLED VEHICLE-TRACK SYSTEM

The results presented in previous section were for a constant load moving along the track. Such simulation results are useful for validation of the complex track system model developed for this investigation. Such loading, however, neglects any dynamics of the vehicle and thus not adequate for predicting wheel-rail interaction forces. In order to examine the effectiveness of the coupled vehicle-track system model, the vehicle, track system and adaptive contact models developed in chapter 2 and 3 are utilized in this section. Simulations are carried out to evaluate dynamic wheel-rail contact force using the numerical method proposed in chapter 3.

For this study, the wheel and rail profiles are assumed to be perfect, i.e., free from any defect. Such study will contribute to an in-depth understanding of the vehicle and track dynamics, prior to introducing wheel defect. Parameters for vehicle and track system used for the investigation are obtained primarily from [34], and are presented in Table 4.4. The results from this investigation are analyzed to evaluate steady state wheel-rail interaction at a speed of 100 km/h, as well as the effect of speed on the dynamic interaction forces. The simulations are carried out for a track length with 20 sleeper spans. The time step $\Delta t = 0.000045$ s, and the length step $n = 2$ are used to ensure stable and time efficient simulation.

4.3.1 Steady-State Wheel Rail Interaction

At 100 km/h, steady state solution can be easily reached without any effect of the track boundary condition. At this speed, it takes around 0.5 s for the vehicle to go over the track length considered. The response is found to settle between 0.17 s and 0.37 s when there is no effect of boundary condition. This response is referred to as the steady-state response. The time history of steady-state contact force evaluated at the left and right wheel-rail contact is presented in Figure 4.8. These results show that for perfect wheel, the left and right wheel contact force is identical. The contact force, however, fluctuated between 105.8 kN and 113 kN as the dynamic load (vehicle) moves along a

Table 4.4: Parameters of vehicle and track system

Vehicle System	
Car body mass (quarter of vehicle)	20150 kg
Bolster mass (half)	232.5 kg
Mass moment of inertia of bolster about centerline of track (half)	87.5 kg.m^2
Mass of half side frame (half)	223.75 kg
Mass of wheelsets	1120 kg
Mass moment of inertia of wheelset about centerline of track	420.1 kg.m^2
Primary suspension stiffness	6.5 MN/m
Primary suspension damping coefficient	100 kN.s/m
Secondary suspension stiffness	2.55 MN/m
Secondary suspension damping coefficient	44.24 kN.s/m
Distance between left and right secondary suspension in bogie	1.6002m
Distance between left and right wheel bearing center	1.6002m
Wheel radius	0.475
Track System	
Shear coefficient	0.34
Rail cross section area	7.77×10^{-3}m^2
Shear modulus of rail	81GN/m^2
Elastic modulus of rail	2.07×10^{11} N/m
Second moment of area of rail about Y axis	2.94×10^{-5} m^4
Rail mass per meter	60 kg/m
Pad stiffness	140 MN/m
Pad damping coefficient	45 kN/m
Ballast stiffness (*)	40 MN/m
Ballast damping coefficient (*)	50 kN.s/m
Sleeper mass	270 kg
Mass moment of inertia of sleeper	90 kg.m^2
Sleeper spacing	0.685 m
Rail support distance (*)	1.505 m
Radial spring stiffness	3.3443×10^{10} N/m/radian
Note: The parameters with(*) are not given by reference [34] and assumed according to typical freight car[1]	

continuous rail supported on sleepers. It can be obtained that the static contact force or the normal load due to vehicle is 107.6 kN.

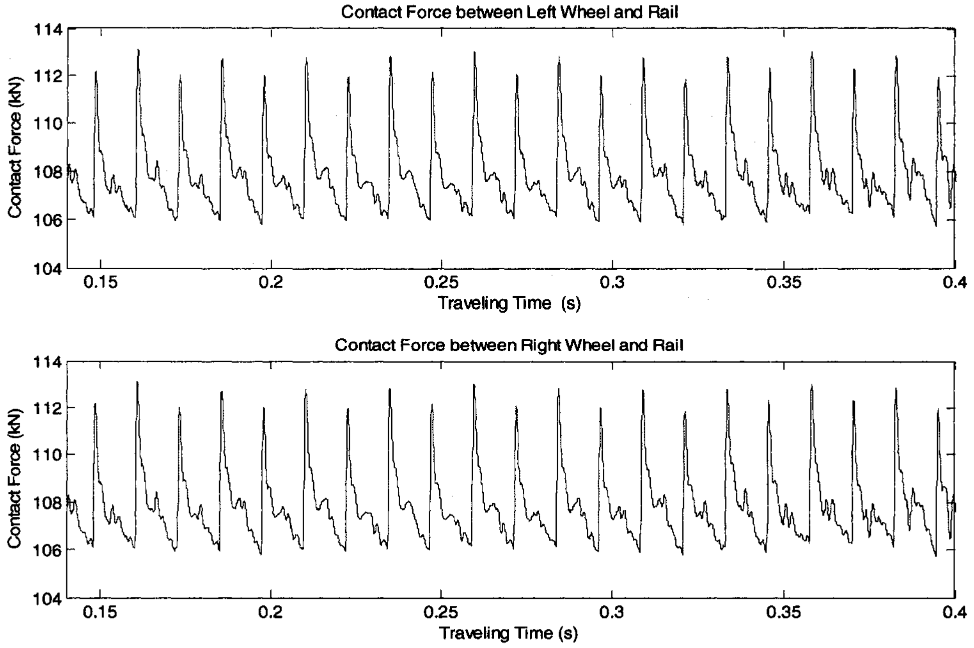

Figure 4.8: Time history of steady-state wheel-rail dynamic contact force

For a close look, the result of contact force represented as a function of sleeper-span is shown in Figure 4.9. These results represented for sleeper numbers 5 to 14 clearly show that as the wheel reaches the sleeper support, the contact force peaks, after which the contact force drops close to its static value and peaks again as the wheel reaches the mid-span between two sleepers. It is further noted that the peak reached at the mid-span is slightly larger than that reached at the sleeper support. Clearly, as the wheel and rail oscillate in the vertical direction, certain impact forces are created between the wheel and rail due to the presence of discrete supports. These impact forces are, however, very small compared to the static wheel load.

In practice, variation in wheel-rail contact force is generated due to variation in relative displacement between wheel and rail. For a better understanding, the rail deflection as a function of sleeper span is presented in Figure 4.10. As the result shows, the deflection of rail at the sleeper span is larger than that at the sleeper support. The larger inertia force for the vehicle mass is thus the cause for larger peak contact force at mid-span.

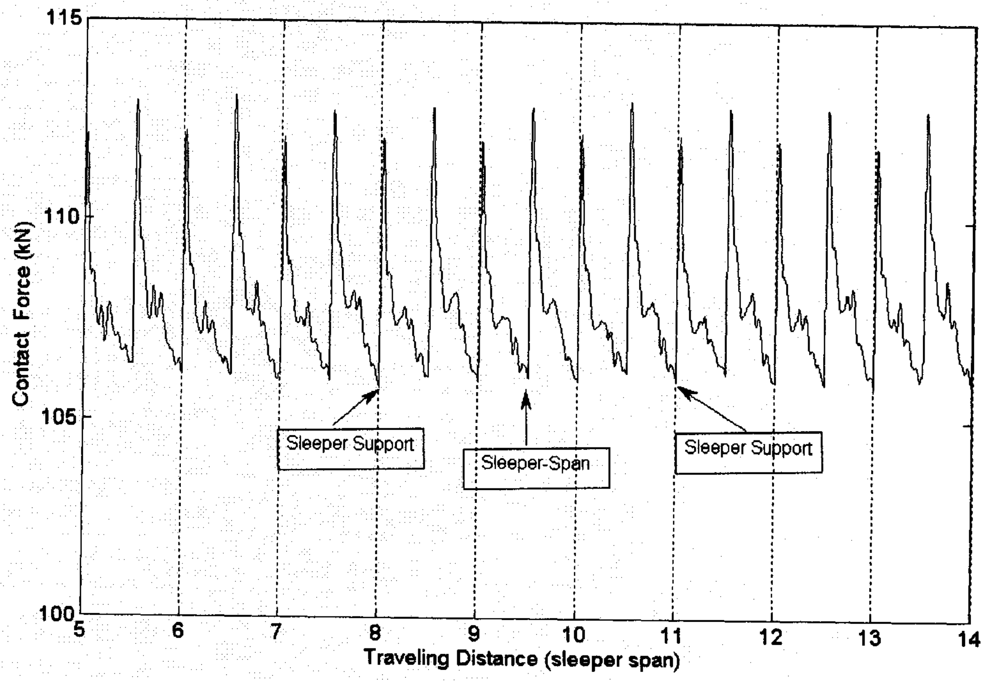

Figure 4.9: Distance history of steady-state wheel-rail dynamic contact force

When the time history of deflection for rail and wheel are examined as shown in Figure 4.11, it reveals that both follow the same trend. The difference in the deflection establishes the dynamic wheel-rail interpenetration, which causes the dynamic contact force.

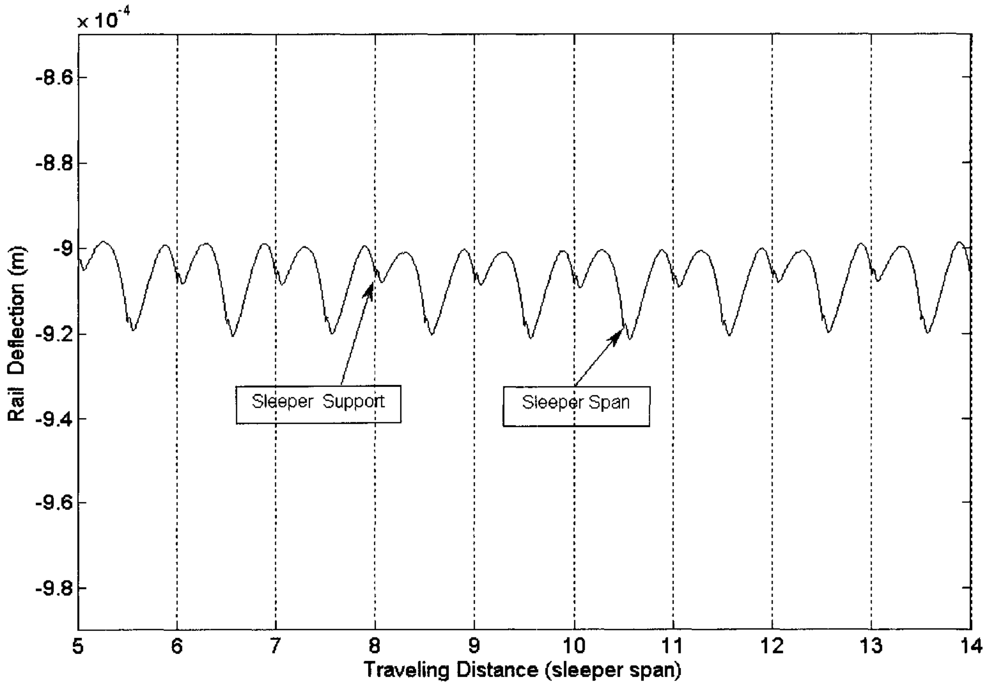

Figure 4.10: Distance history of steady-state rail dynamic deflection

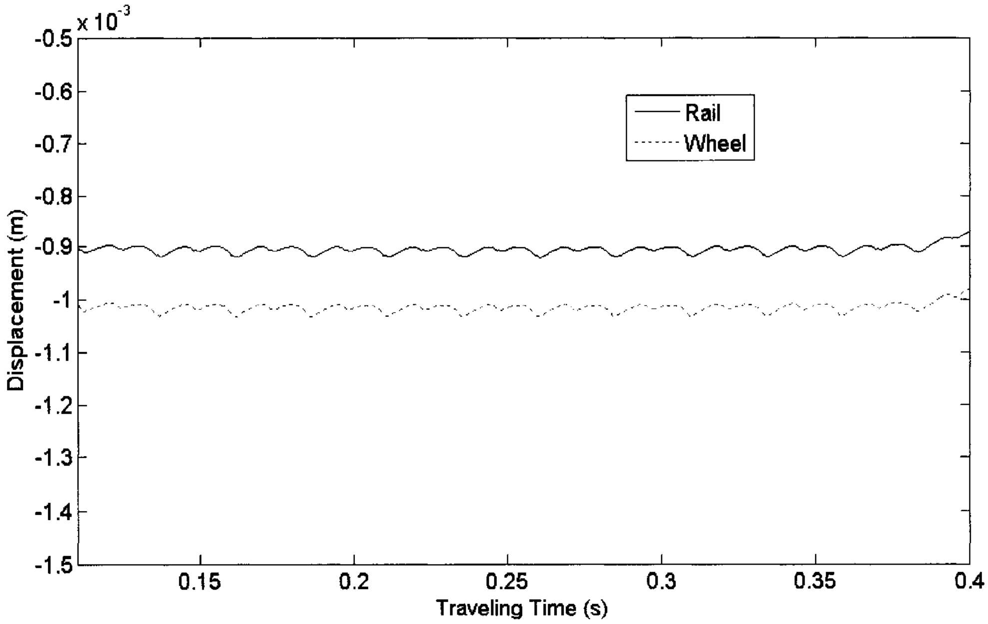

Figure 4.11: Time history of steady-state vertical displacement of wheel and rail

4.3.2 Effect of Speed on Dynamic Contact Force

As found in contact force analysis at 100km/h presented in the previous section, the wheel, even when of perfect profile, does go through vertical oscillation due to periodic support under the rail. Therefore, it is likely that forward speed of the wheel or vehicle will generate larger inertia force at higher speeds, leading to larger contact force. Furthermore, it is likely and it is believed by many researches [1, 67] that there should be a resonance when the passing frequency (speed/sleeper spacing) equals to certain coupled wheel-track natural frequency components. The peak contact force therefore should be larger when the frequency is close to one of the natural frequencies of the coupled wheel-rail system.

In this section the results of simulations carried out at speeds in the range of 10 to 350 km/h is presented and discussed. Figure 4.12 presents the contact force waveform as a function of traveling distance scaled by sleeper span for 3 sample (10, 50 and 100km/h) speeds. These results clearly show that peak impact force both at the sleeper support and mid-span increases as the speed is increased. Further more, the waveform of the contact force is somewhat affected by the forward velocity. The waveform between peak impacts is more distinct when the speed is low and the oscillation diminished prior to next peak. Whereas, the waveform is less distinct and the waveform can not dissipate prior to next peak as the speed is increased.

The peak contact force at the sleeper support and sleeper span for speeds in the range of 10 to 350 km/h are presented in Figure 4.13. The results show a general trend of increased contact force as the speed is increased. The contact force is always larger at the mid-span than those at the sleeper location. The difference between the peak force at the sleeper location and mid-span increases as the speed is also increased. All these are directly attributed to the increase in vehicle inertia force when going through oscillation at high speeds.

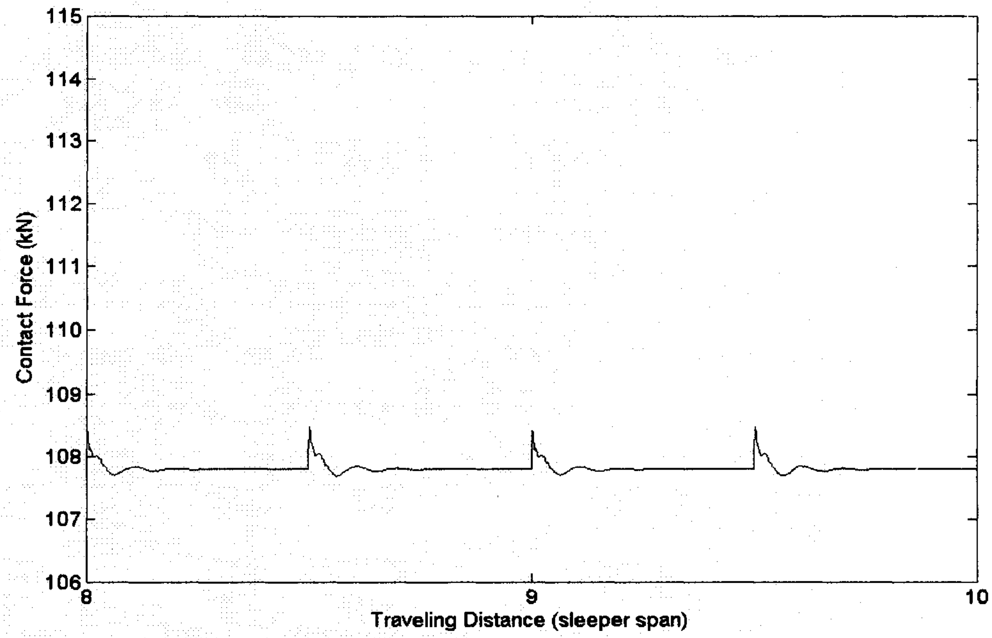

(10km/h)

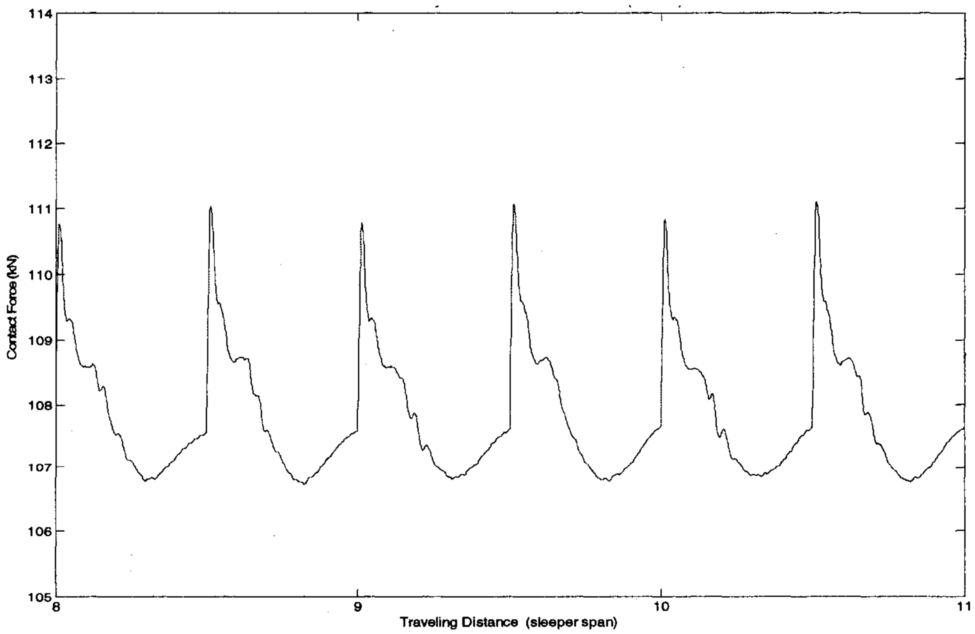

(50km/h)

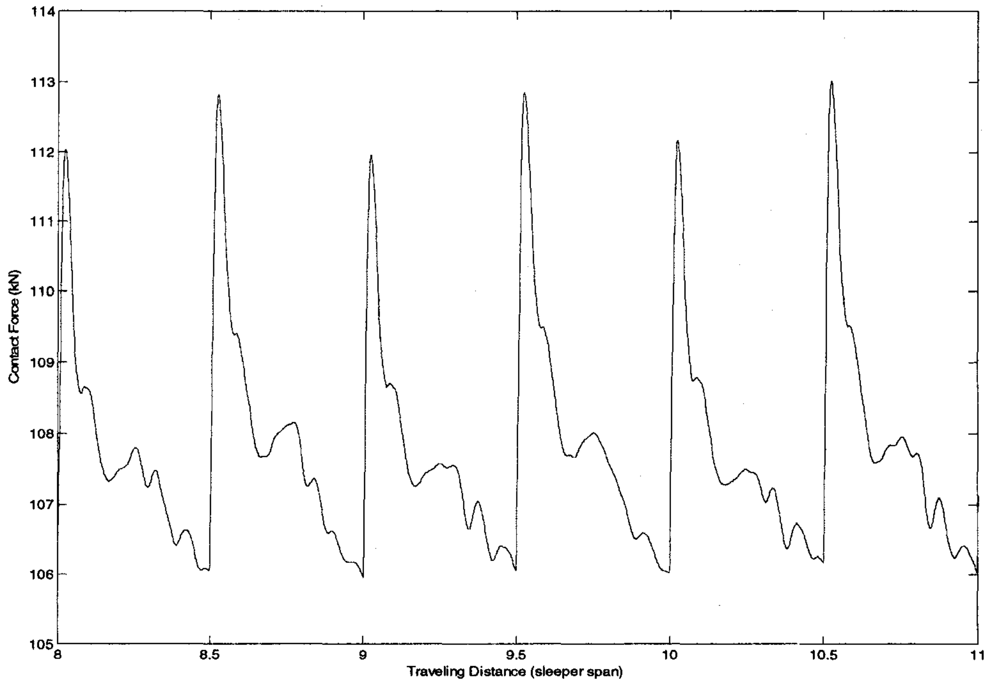

(100km/h)

Figure 4.12: Steady-state wheel-rail contact force at different speed

More interestingly, the trend in Figure 4.13 clearly shows two distinct peaks. The first peak occurs at 50 km/h, which corresponds to a passing frequency of 20.3 Hz. This is perhaps close to the fundamental natural frequency of track system. The second peak observed at 100 km/h corresponds to passing frequency 40.6 Hz, which is expected to be close to one of the natural frequencies of coupled vehicle-track system.

The results in Figure 4.13 can be readily compared with those obtained by Nielsen [37] for similar model parameters. Both the results presented, and in [3] show the same trend with peaks near 50 and 100 km/h. Nielsen reported one of his calculated vehicle-track resonance frequencies to be 42 Hz.

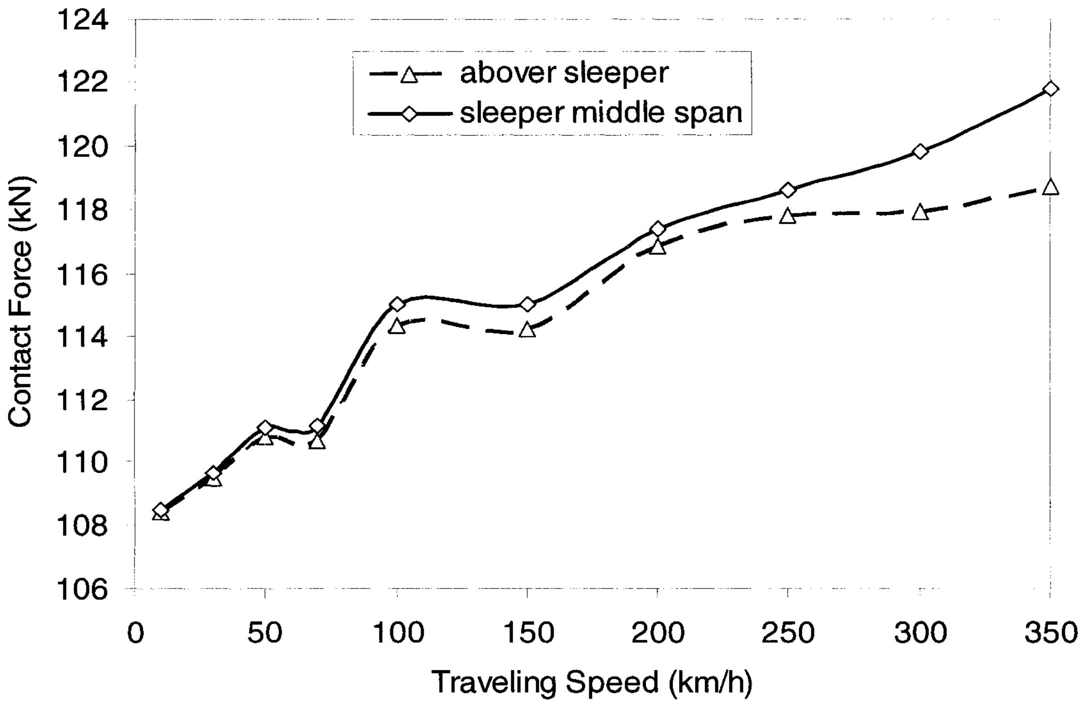

Figure 4.13: Effect of speed on wheel-rail contact force in steady-state
(Static load 107.8 kN)

4.4 SUMARRY

The dynamic response of track system under a constant moving load is investigated in order to validate the model and numerical method. The results show that a rail length of 20 sleeper span is adequate to simulate infinite long track with a finite length as long as response away from the boundary is used. The effect of the important simulation parameters, i.e., the time step and length step on the numerical solution is studied, and the critical time step required to ensure the stable solution is established.

The results show that there exists a critical time step beyond which the stable solution can not be obtained. The critical time step is determined by the length step besides track properties such as bending stiffness *EI* and shear stiffness *KAG*, *etc*. Small length step (Δx) results in further reduction in critical time step. As far as the effect of length step is concerned, refining length step can reduce the undulation of the response of rail deflection. The peak deflection and contact force, however can be effectively predicted by a length step equal to the half of the sleeper span, i.e., $n = 2$.

This chapter also presented dynamic interaction between wheel and rail when a dynamic model of a vehicle with perfect wheel profile is included. The results show that the discrete sleeper support acts as a source of excitation for the vehicle-track dynamics interaction. The deflection of rail above sleeper support and corresponding contact force is found to be smaller than at the sleeper span. This study shows that even for perfect wheel and rail interface, there are light impacts between wheel and rail in steady-state. The results also demonstrated that this dynamic interaction force increases with increasing vehicle traveling speed. The resonant phenomena noted by other investigators are also observed in this study.

From the results obtained in this section, it is obvious that the wheel of a bogie in a pitch plane will effect the rail deflection under each wheel. Therefore, one axle model will slightly underestimate the deflection. The present study using a roll plane vehicle model with one axle is, however, necessary for this investigation as it focuses on the effect of wheel defect on the other wheel in an axle.

For the analysis of moving load presented in this chapter, it is observed that under certain load at certain location within the track, one or more sleeper may want to lift off the ballast. Hence it may be appropriate to consider nonlinear elasticity between the sleeper and ballast for further study.

CHAPTER 5

IMPACT LOAD DUE TO SINGLE WHEEL FLAT

5.1 INTRODUCTION

Wheel flat and shelling are the most common wheel defects encountered by railway industry. 1999 AAR CRB data for wheel defects shows that flat and shelling account for 22.7% and 67.48%, respectively [11]. These defects cause significant wheel-rail impact load and therefore, the wheels with certain size defects must be replaced in time. According to AAR estimation, the North American railway industry spent approximately $90 million annually to replace 125000 wheels due to wheel tread defects in 1990's [66]. These tread defects have increased dramatically in recent years and thus the number of wheels which have experienced high impact loads has similarly increased. It is very important to investigate the influence of wheel defects on impact load experienced by vehicle and track components in order to set reasonable removal threshold, optimize track vehicle design, develop smart wheelset and effective defect detectors for early warning generation.

It is well known that wheel defects such as wheel flat can cause abnormally high impact load and stress in vehicle track system. The impact load may initiate fatigue cracks or cause final fracture in the components such as bearings, axles and rails, which can lead to transportation disasters. Although small wheel flats can not induce excessively high stress to cause incidents, they can cause abnormally high periodic impact which contribute to the track deterioration and increase cost of maintenance. With constant effort to realize higher operating speed and popularization of heavy haul freight trains, this problem is more serious than ever [32]. Besides the safety and economic concern, these defects can also cause significant annoying noise and thus impair the environment [2]. It is thus necessary to set limits for the impact loads as well as the defect size.

In resent years, considerable effort has been made directly forward prediction of wheel rail impact force as a result of wheel flat and shelling. Cai [24] and Zhai [51] developed coupled vehicle-track system model to investigate the relationship between wheel rail irregularities and impact loads. Dong [1] carried out intensive study on the factors which affect the impact loads induced by wheel flats. Nielsen [41] and Wu [33] considered nonlinearity of track system in predicting wheel rail impacts. However, most of these works were carried out utilizing pitch-plane model and Hertzian contact theory. As discussed in literature review, impact loads predicted by these investigations trend to underestimate the impact load at low speed while overestimate at high speed when compared with experimental results. For the present investigation, an adaptive wheel-rail contact model based on radial spring is developed. Furthermore, a roll-plane model of vehicle incorporating 3D track model is used to investigate the effects of wheel defect on the cross wheel-rail contact forces.

Although the model can predict response of the track and vehicle system, only the impact load due to wheel flat is examined in the present study. The effect of other types of wheel rail defects can be studied in the similar way as long as the defects' geometric profile is defined similarly to that of the wheel flat described in chapter 2. The objective of this chapter is to carry out a thorough investigation of wheel-rail impact load due to a single wheel flat. The results obtained in this investigation are compared with other studies that deal with impact load due to a wheel flat and experimental results that are available in the literature. A parametric study is also carried out to examine the influence of several vehicle and track system parameters on the impact load.

As discussed in literature review, the worn or rounded flat is a more realistic representation of a wheel flat and haversine flat model is used by most researchers. In this study, the single haversine type flat is used and described by a sinusoidal function. The geometric profile of wheel rim with such a flat was defined and discussed in chapter 2.

5.2 IMPACT LOAD DUE TO A SINGLE FLAT

It was shown in chapter 4 that even for a perfect wheel, there is small impact type contact force between wheel and rail as the vehicle travels over a periodically supported rail. If a wheel with a flat is introduced, it is expected that there will be considerably large periodical impact loads between wheel and rail as a vehicle runs along the track.

A nominal wheel flat in this investigation is defined as 100 mm long and 1.5 mm deep. This flat is introduced only to the left wheel, while the right wheel is assumed to have a perfect profile. The geometric profile of the defective wheel rim is illustrated in Figure 5.1, which shows the change in wheel radius as a function of wheel position.

The numerical method presented in chapter 3 and used in chapter 4, is utilized here to generate time domain solutions. The parameters used are as same as those used in chapter 4 and presented in Table 4.4. The first set of contact force time history obtained for vehicle speed 70 km/h and the track with length of 50 sleeper-spans ($N = 50$) is presented in Figure 5.2.

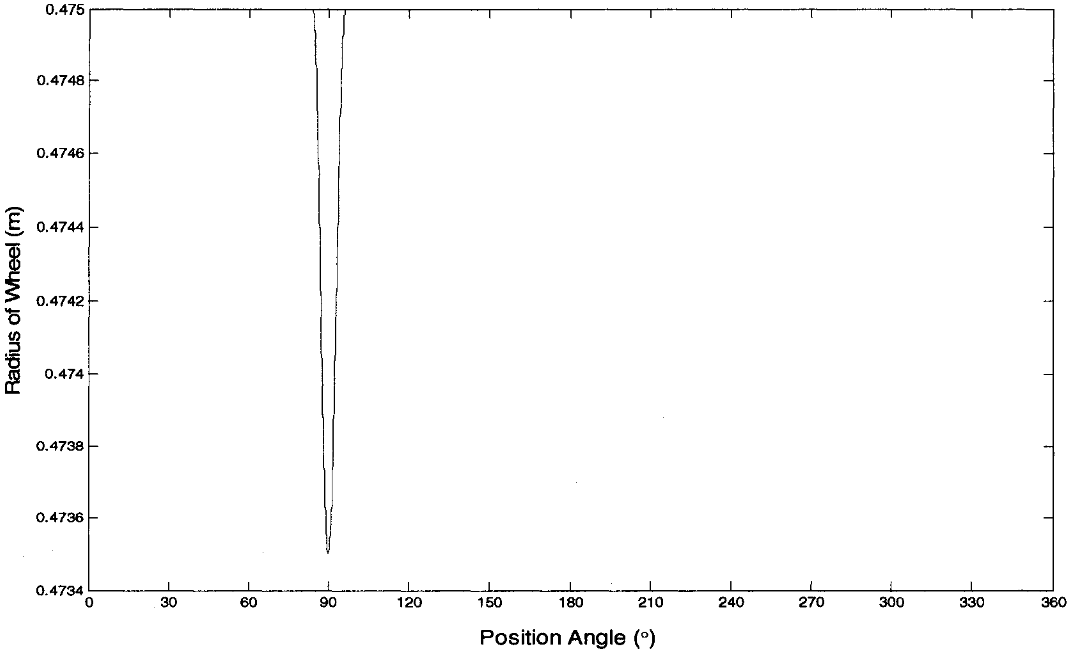

Figure 5.1: Geometric profile of a wheel rim with a flat (100 mm long, 1.5 mm deep)

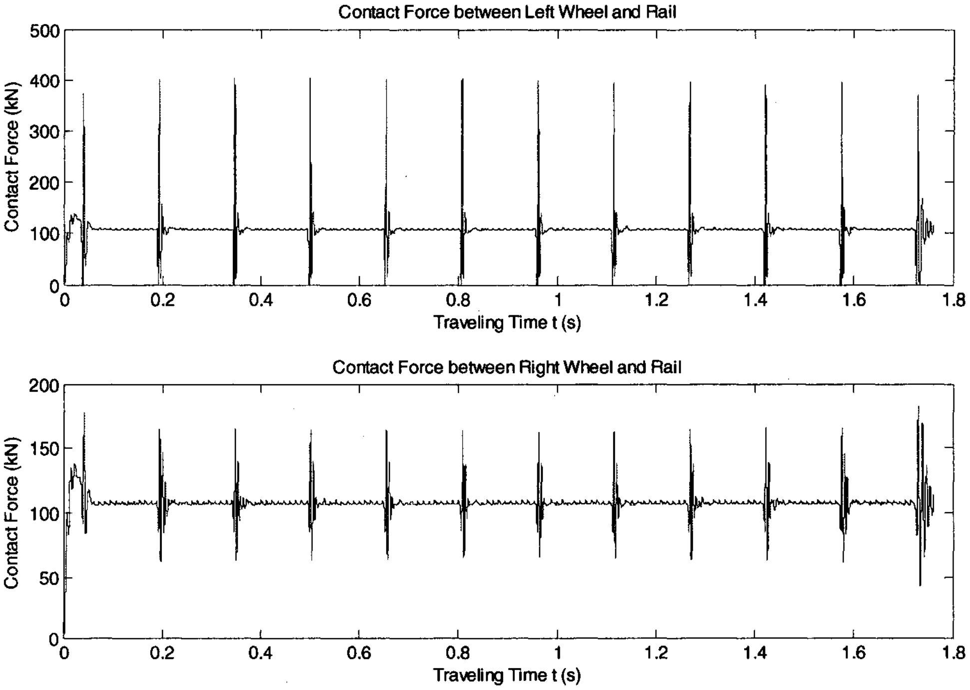

Figure 5.2: Time history of wheel-rail contact force due to a single wheel flat

The results show that there is a significant impact force at the left wheel-rail interface due to the flat. This in turn introduces considerable impact load at the right wheel-rail interface with slight time delay (Figure 5.3). The results further show that the impact load dissipates rapidly and there is a small oscillation of the contact force during perfect wheel contact in between the impacts. This variation was also observed for perfect wheel simulation in chapter 4. The results in Figure 5.2, obtained for 50 sleeper-spans show that there is very little effect of boundary condition and the steady-state is reached within 0.2 s. A long segment of the track is considered for this simulation to obtain the impact force at different locations of the rail with respect to a sleeper position. A close examination of the time history of steady-state impact force reveals that there is a small variation in the impact peak which is attributed to the fact that the impact may be produced at different rail location with respect to the sleeper support.

One impact segment from the simulation is presented in Figure 5.3 that comprises of the contact forces at the left and right wheel-rail interface. When the flat on left wheel comes into contact, the contact force reduces due to loss of contact as the left wheel suddenly drops while the left rail moves up until the wheel hits the rail. Thus an impact force is produced. As shown in Figure 5.3, there is a total loss of contact at the left wheel for the speed and flat size considered. After the impact, the contact force oscillates for about a cycle prior to dissipating due to the damping.

Figure 5.3 further shows that the contact force at the right wheel-rail interface also varies in a similar manner. The magnitude in this case, however, is much smaller and takes places with a time delay in relation to the left wheel. For the speed and flat size considered, the impact force at the left wheel with flat is found to be more than 3.5 times the static load, whereas the peak force at the other side is about 1.5 times the static wheel load.

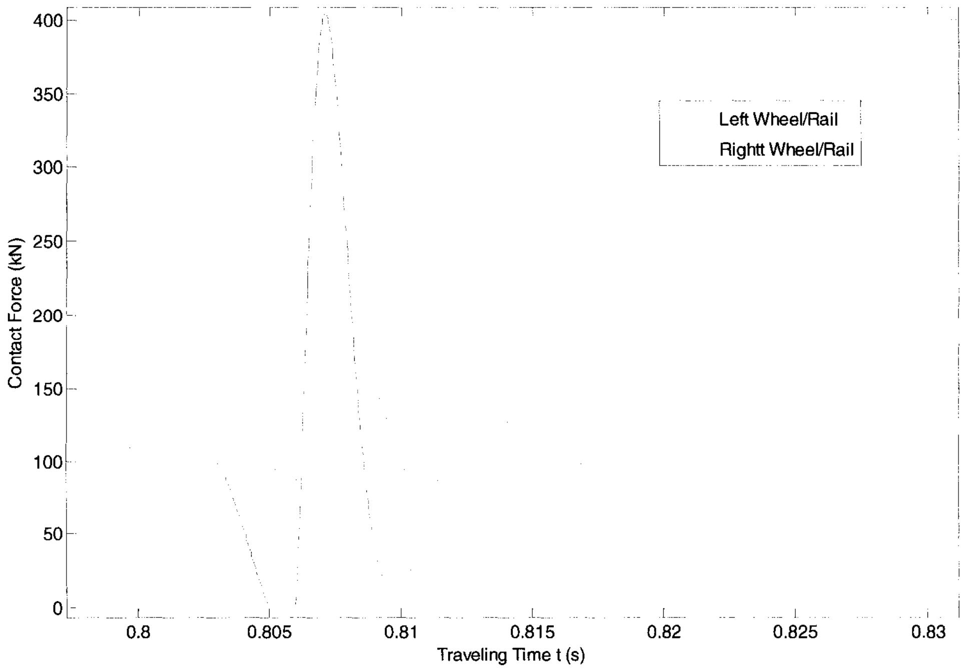

Figure 5.3: Contact force time history in the proximity of wheel flat contact

In order to examine the variation in the steady-state impact force, the contact force at the left wheel-rail interface is plotted as a function of distance in Figure 5.4, which presents the response between number 14 and 24 sleeper. The results confirm that the impact force on or near a sleeper support is slightly larger than those in the mid-span of the sleepers. This can simply be attributed to the fact that the sleepers introduce stiffer elastic support. This variation, however, is not highly significant.

Since in practice it is not possible to control where the flat will hit with respect to sleeper location, it is recommended that the largest value of impact force over a track segment of reasonable length should be taken as the impact force.

Finally, to examine the impact sequence in terms of wheel and rail motion, the time history of wheel rail displacements is presented in Figure 5.5. The results show the change of wheel and rail movement at the left and right track as the vehicle runs along the track. When the flat on left wheel comes into the contact region, the left rail moves up and wheel drops down prior to impact between wheel and rail. After impact, the left wheel and rail oscillate around their individual static position for a short duration. Meanwhile, both rail and wheel move up at first to compensate for the roll motion of the axle as left wheel drops due to the flat. The resulting oscillating motions of the rail and wheel at the right side lead to a change in the contact force experienced by the right wheel.

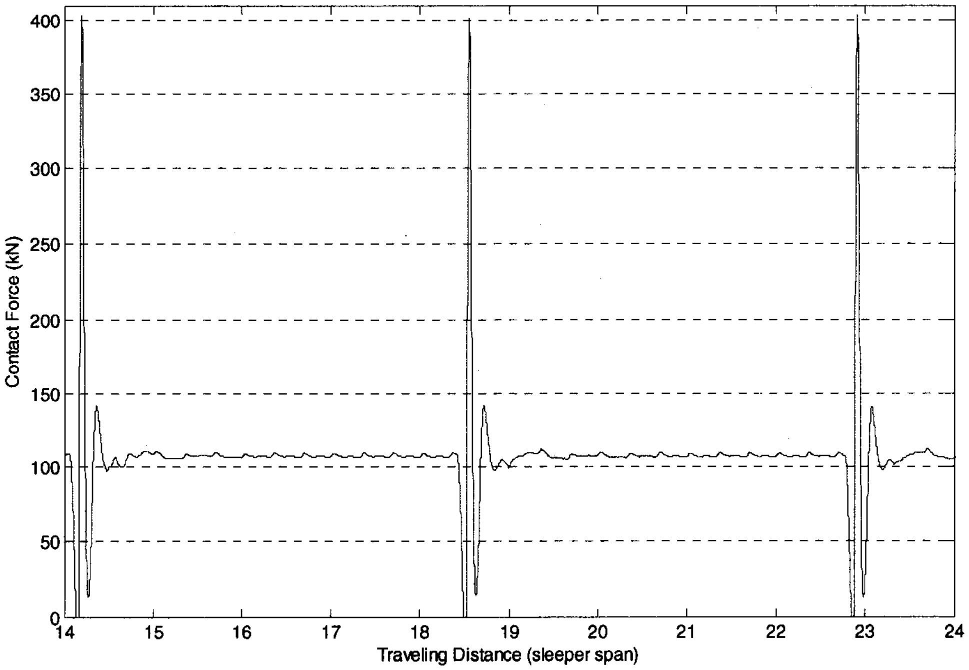

Figure 5.4: Distance history of wheel-rail contact force as a function of sleeper span

The results presented and analyzed in this section are obtained for a new adaptive contact model developed for this investigation. In such study, it is essential to compare the results with those produced by commonly used contact models, results obtained by other researchers and available experimental results. The following section is thus devoted to a comparative study.

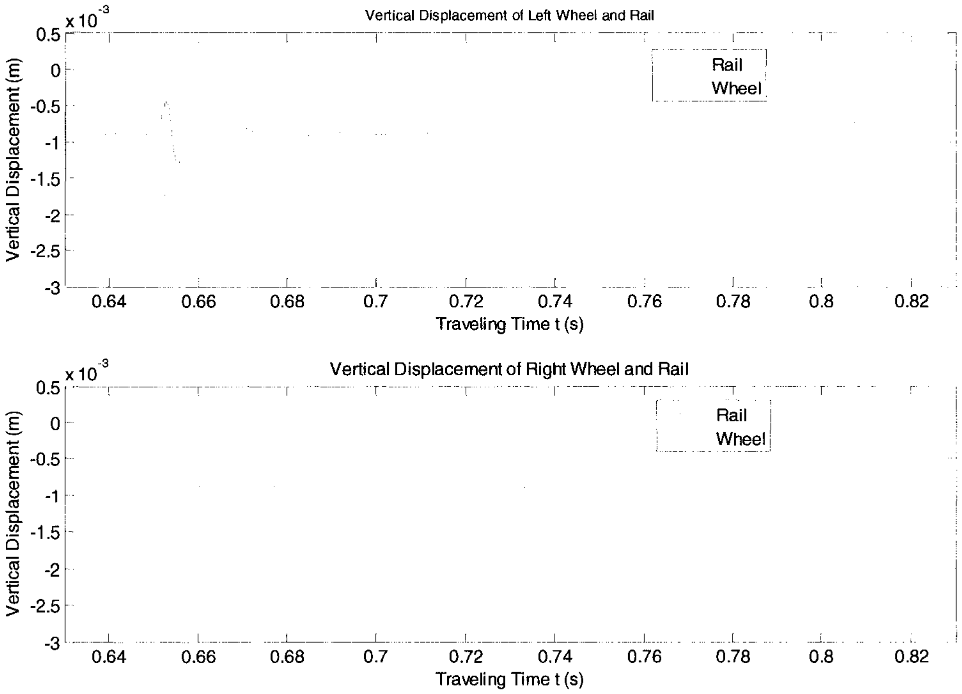

Figure 5.5: Time history of wheel-rail displacement

5.3 COMPARATIVE STUDY OF PROPOSED MODEL

As specified in literature review, a lot of effort has been devoted to investigate the railway wheel-rail impact load due to wheel rail defects by field test and computational simulation. In any comparison, it is essential that identical system and operating conditions are used, and presents a challenge since all vital data information are not always readily available. A best effort is therefore made to modify the present model parameters to reflect the one compared with.

5.3.1 Comparison with Hertzian Contact Model

The most widely used contact theory for vertical wheel-rail contact force simulation is the Hertzian contact model. One of the motivations for the present investigation was to introduce a new radial spring adaptive contact model that can accommodate asymmetric contact region for defective wheel profile. In order to compare the developed model in application to wheel flat, the vehicle-track system model incorporating Hertzian contact model and the developed adaptive contact model are simulated for identical parameters. A common value in literature is used for Hertzian contact coefficient ($c_H = 0.85x10^{11}$) for Hertzian contact model, while the radial spring stiffness of the adaptive model is selected such that both models yields identical static contact force.

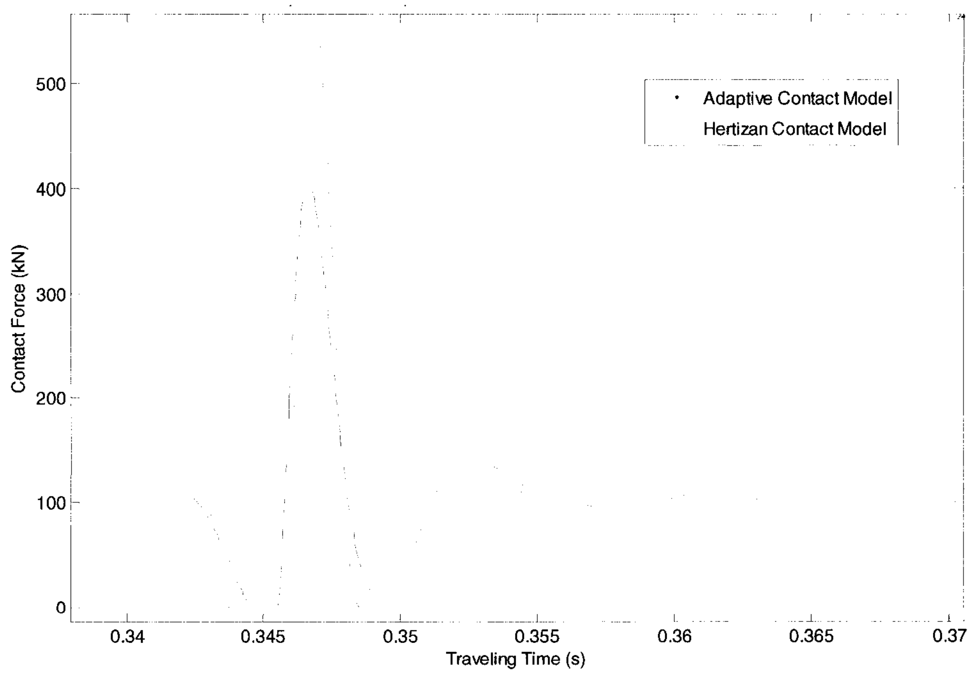

Figure 5.6: Comparison of contact force from adaptive and Hertzian contact model

The simulation is carried out for a 100 mm long and 1.5 mm deep flat at a speed of 70 km/h. The contact force result for one steady-state impact cycle is shown in Figure 5.6. As the results show, the impact force from Hertzian contact model (558.0 kN) is significantly larger than that from adaptive model (404.7 kN). The impact force predicted by adaptive contact model is therefore 27.5% less than that from Hertzian contact model at 70 km/h for given parameters. The results in Figure 5.6 further show that the Hertzian contact model predicts the loss of contact of wheel-rail second time after the impact, and the duration of the second loss of contact is even larger than the first one, which is unlikely in practice.

In order to examine the effect of speed, impact load due to the same flat within the speed range 0 ~ 180 km/h is plotted in Figure 5.7. As the results show, both models predict similar trend for change in speed. However, in comparison to adaptive contact model, Hertzian contact model underestimates wheel-rail impact load at low speeds, and overestimates the impact load at high speeds.

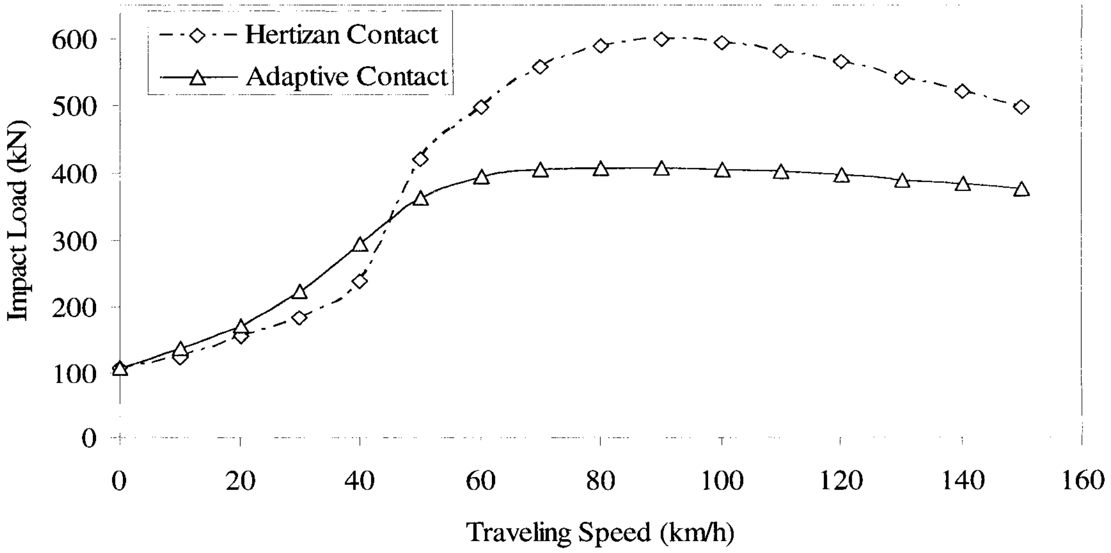

Figure 5.7: Comparison of wheel-rail impact load from different contact model

Such a trend for the performance of adaptive contact model is very encouraging since it is well known in the literature that for simulation of impact force due to wheel flat, Hertzian contact model may underestimate at low speeds while may overestimate at high speeds. Another noticeable difference between the two contact models as shown in Figure 5.7 is the fact that beyond 90km/h, the impact force predicted by Hertzian contact model reduces considerably as speed is increased, whereas the adaptive contact model exhibits very small reduction with increasing speed.

5.3.2 Comparison with other Published Works

Sun [34] developed a three-dimensional wagon-track system dynamics (WTSD) model to simulate the dynamic wheel rail interaction. In his study, the dynamic response of the whole wagon-track system was simulated with wagon traveling at a constant speed of 70 km/h. Two wheels of the leading wheelset on the front bogie were assumed to contain flats (40 mm long, 0.35 mm deep) laterally symmetric to the mass center of the wheelset. The contact model in his investigation was based on multipoint contact developed by Dong [1]. His model was validated against field test data measured by Fermer and Nielsen in 1995 [34, 66]. The results presented in Figure 5.8 show that contact force time history from both Sun's simulation and the field test [34]. The work as shown claims very good agreement with experimental data. The simulated impact force was in fact found to be close to the measured one, whereas the frequency was found to be somewhat different.

The present model parameters, as same as those Sun used shown in Table 4.4 to represent the system and wheel flats [34], is simulated to establish the contact force time history as presented in Figure 5.9. This response from adaptive contact model is found to provide an even better agreement with experiment magnitude. It should, however, be noted that the present model uses a highly simplified in-plane vehicle system model with two layers 3D track system model.

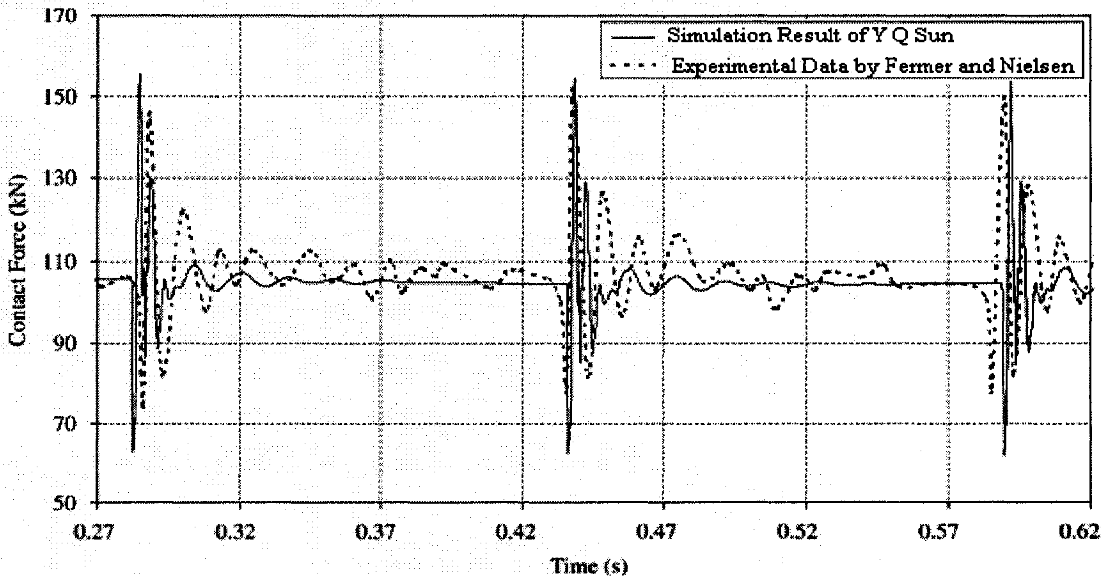

Figure 5.8: Reported data of contact force time history by Y. Q. Sun [34]

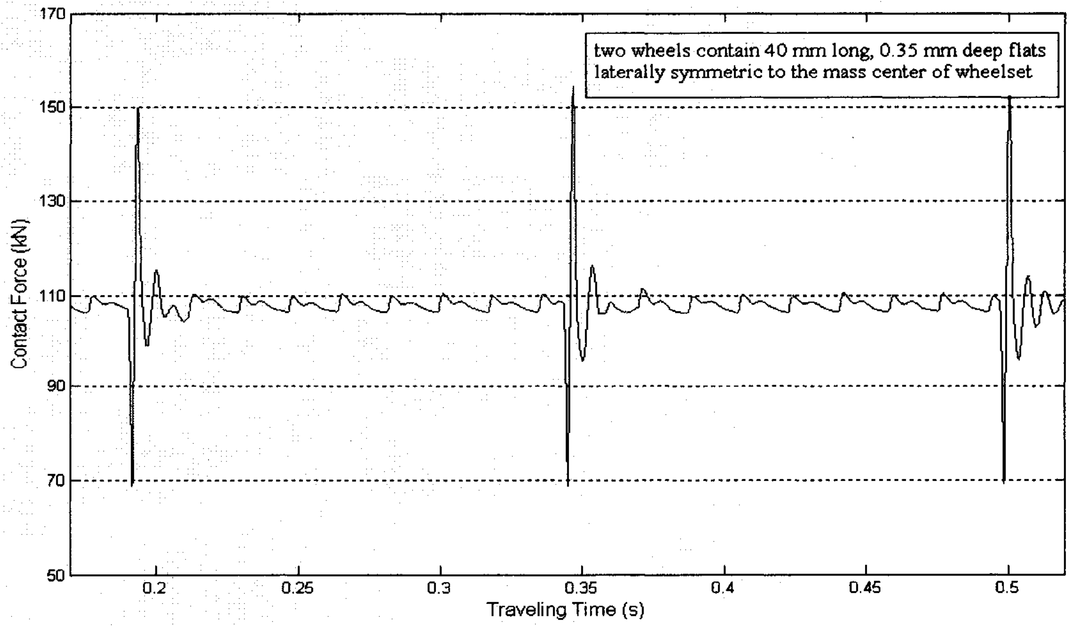

Figure 5.9: Time history of wheel-rail contact force obtained in present work

When the three sets of results during the period when perfect part of the wheel is in contact are examined, there is a difference in both magnitude and impact pulse frequency components of the results. The experimental frequency is difficult to analyze as the radius of wheel may not remain constant in practice. Furthermore, the damping used in the present model, which is assumed by Sun [34] may be too large compared to the actual damping present in the field track which is difficult to verify.

Dong [1] carried out extensive analyses of impact load due to wheel flats in his PhD dissertation research. He developed a multipoint contact model using a set of vertical spring inserted between wheel and rail. An attempt is made to compare the simulation result from present investigation with his result presented in [1]. For this, the parameters representing the coupled vehicle-track system are adjusted to the ones used in [1] as listed in Table 5.1. The simulated wheel-rail contact force for a wheel with a 100 mm long, 1.5 mm deep flat at speed of 117 km/h is presented in Figure 5.10. Here the time history result is superimposed on the results obtained by Dong [1] for multipoint contact and linearized Hertzian contact model. The results show that multipoint contact model predicts significantly larger impact force at this speed when compared to the one obtained from the adaptive contact model. The linearized Hertzian model predicts even smaller impact force due to the same wheel flat. A comparison of these results further show that both multiple contact and linearized Hertzian contact model predict a lift-off of the wheel from the rail, both before and after the impact, whereas the present model exhibit loss of contact only before the impact.

Table 5.1: Parameters of vehicle and track system [1]

(Canadian Pacific Railway)

Vehicle System	
Car body mass (quarter of vehicle)	1470.2 kg
Bolster mass (half)(*)	232.5 kg
Mass moment inertia of half bolster about centerline of track(*)	87.5 kg.m^2
Mass of half side frame (half)	250 kg
Mass of wheelsets	1300 kg
Mass moment of inertia of wheelset about centerline of track	500 kg.m^2
Primary suspension stiffness	788 MN/m
Primary suspension damping coefficient	3.5 kN.s/m
Secondary suspension stiffness	6.11 MN/m
Secondary suspension damping coefficient	158 kN.s/m
Distance between left and right secondary suspension in bogie(*)	1.6002m
Distance between left and right primary suspension in bogie(*)	1.6002m
Wheel radius	0.4572
Track System	
Shear coefficient	0.34
Rail cross section area	8.61×10^{-3}m^2
Shear modulus of rail	81GN/m^2
Elastic modulus of rail	2.07×10^{11} N/m
Second moment of area of rail about Y axis	3.95×10^{-5} m^4
Rail mass per meter	67.57 kg/m
Pad stiffness	200 MN/m
Pad damping coefficient	30 kN.s/m
Ballast stiffness	40 MN/m
Ballast damping coefficient	50 kN.s/m
Sleeper mass	180 kg
Mass moment of inertia of sleeper	90 kg.m^2
Sleeper spacing	0.6069 m
Rail support distance (*)	1.505 m
Radial spring stiffness	5.3787×10^{10} N/m/radian
Note: The parameters with(*) are not given by reference [1] and assumed according to common railway track and freight car	

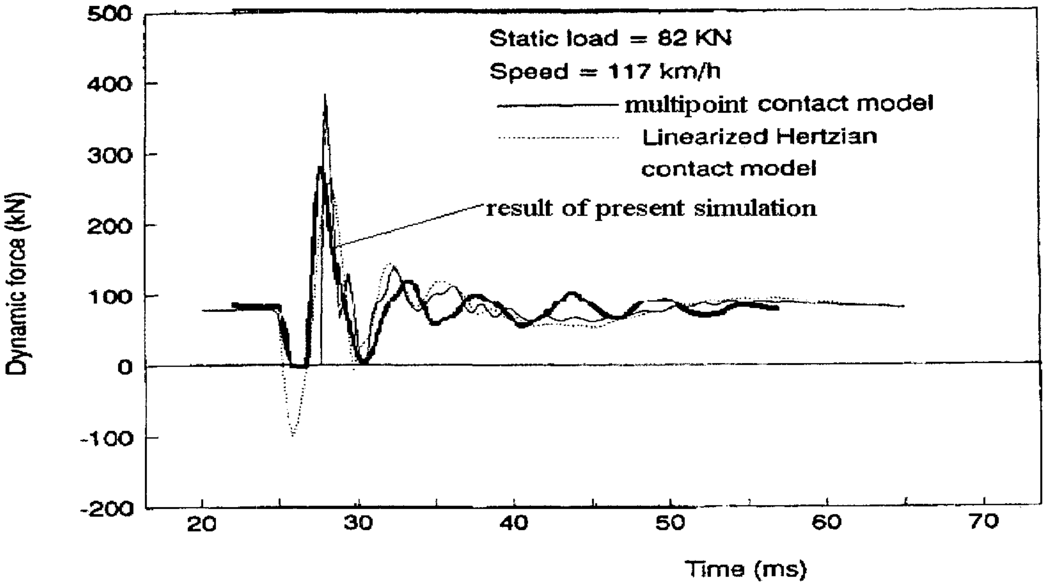

Figure 5.10: Time history of contact force due to a 100 mm long, 1.5 mm deep flat from [1] and present study

5.3.3 Comparison with Field Test Carried Out by CHARMEC

In order to investigate the influence of wheel flat on the dynamic wheel-rail contact force, the Centre of Excellence CHARMEC (CHAlmers Railway MEChanics) carried out extensive field measurements in Svealandsbanan, Sweden on the main line between Eskilstuna and Sodertalje in cooperation with Chalmers University of Technology in 2000 [9]. The response of wheel-rail contact force due to a 100 mm long, 0.9 mm deep wheel flat was measured at different traveling speed.

The wheel rail contact force was measured utilizing an instrumented sleeper bay over which a bogie with a flat wheel was moved at different speeds. A sample of experimental time history of impact force at 50 km/h is shown in Figure 5.11. As the result shows, the wheel-rail contact force recorded is zero except when the wheel is on the instrumental sleeper bay. The impact sequence can be clearly identified from the result. As the wheel flat approaches contact region, there is an initial drop in the contact force from the static value. This is followed by a relatively sharp peak force referred to as the impact force. Finally the impact force is followed by a damped oscillation of the contact force.

The experimental vehicle and track parameters and description of wheel flat (100 mm long and 0.9 mm deep) are also simulated using the developed model for this investigation. Majority of the parameters are obtained from reported studies by Anderson and Oscarsson [43] and by Nielsen and Oscarsson [41]. They also carried out numerical simulation of wheel-rail impact force response due to such wheel flat to compare with experimental results in [9]. These parameters are presented in Table 5.2. The time history of the contact force from the current study is presented in Figure 5.12. The result for 50 km/h shows very good agreement with the field test result presented in Figure 5.11. The peak contact force (215.1 kN) and the trend predicted from this simulation is very similar to the peak (211 kN) and trend observed in the field test.

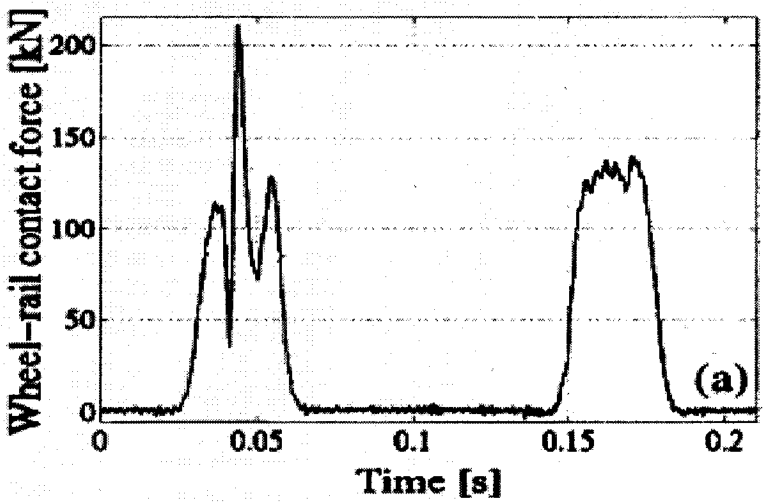

Figure 5.11: Time history of wheel rail contact force measured in one instrumented sleeper bay at 50 km/h [2]

Table 5.2: Parameters of vehicle and track system

Vehicle System	
Car body mass (quarter of vehicle)	22135 kg
Bolster mass (half)(*)	232.5 kg
Mass moment of inertia of bolster about centerline of track (half)(*)	87.5 kg.m^2
Mass of half side frame (half)(*)	223.75 kg
Mass of wheelsets	1185 kg
Mass moment of inertia of wheelset about centerline of track(*)	420.1 kg.m^2
Primary suspension stiffness(*)	788 MN/m
Primary suspension damping coefficient(*)	3.5 kN.s/m
Secondary suspension stiffness(*)	6.11 MN/m
Secondary suspension damping coefficient(*)	15.8 kN.s/m
Distance between left and right secondary suspension in bogie(*)	1.6002m
Distance between left and right primary suspension in bogie(*)	1.6002m
Wheel radius	0.45
Track System	
Rail(UIC60) Bending stiffness (EI)	6.4 MN.m^2
Rail(UIC60) Shear stiffness(KGA)	250MN
Rail(UIC60) rotational inertial per unit length(mr^2)	0.24
Rail mass per meter	60 kg/m
Pad stiffness	80 MN/m
Pad damping coefficient	15 kN/m
Ballast stiffness	30 MN/m
Ballast damping coefficient	31 kN.s/m
Sleeper mass	250 kg
Mass moment of inertia of sleeper (*)	90 kg.m^2
Sleeper spacing	0.65 m
Rail support distance (*)	1.505 m
Radial spring stiffness (*)	3.5574x10^9 N/m/radian
Note: the parameters with(*) are not given by reference[41,43] and assumed according to common railway track and freight car	

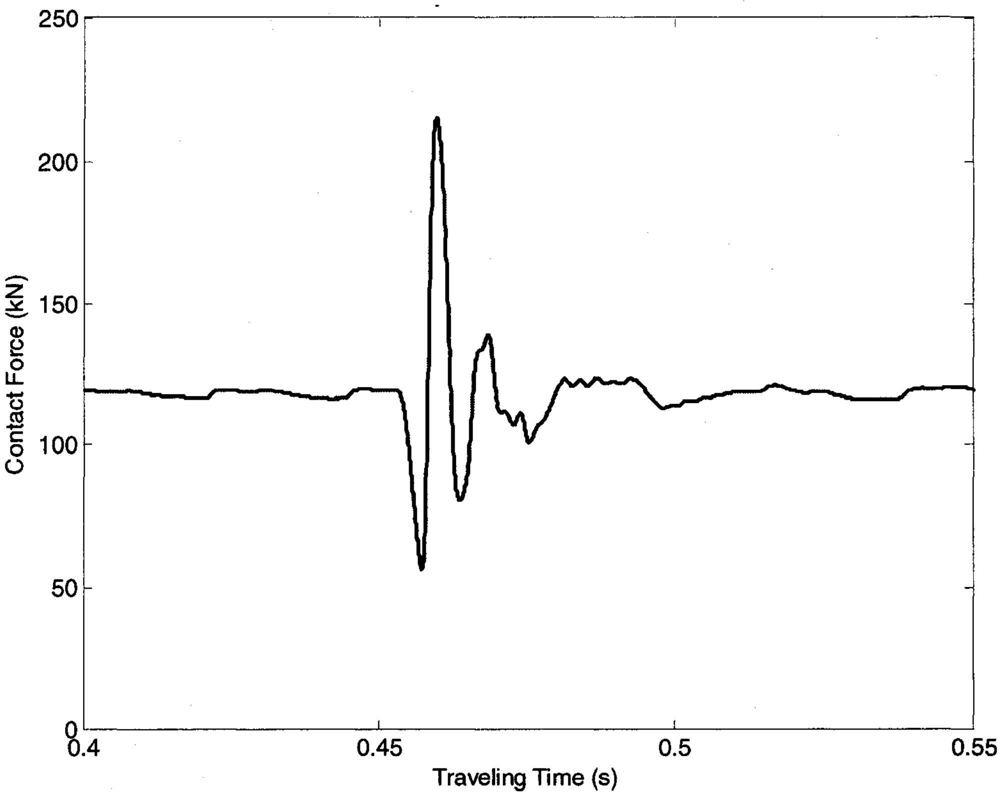

Figure 5.12: Time history of wheel rail contact force calculated in present simulation at 50 km/h

The simulated peak contact or the impact load for the same parameters is evaluated for speed in the range of 5 to 100 km/h. These results are presented in Figure 5.13 along with experimental result from [9]. Figure 5.13 further presents the numerical results obtained in [41, 43] for Hertzian nonlinear contact model along with single wheel vehicle model, and linear and nonlinear track model. Although some experimental results are scattered, it is easy to see that the present vehicle-track model with adaptive contact model shows closest trend to the experiment among all the results presented in Figure 5.13. Particularly, the effectiveness of the adaptive contact model as opposed to Hertzian model at high speed is highly significant. It is also apparent that the simulated results obtained in this investigation trend to predict the upper bounds of experimentally observed impact loads for speeds beyond 40 km/h. From the influence of nonlinearity in the track system [41] as shown in Figure 5.13, it is possible that the present model with track system nonlinearity may produce even a better agreement with the experimental values over the entire speed range.

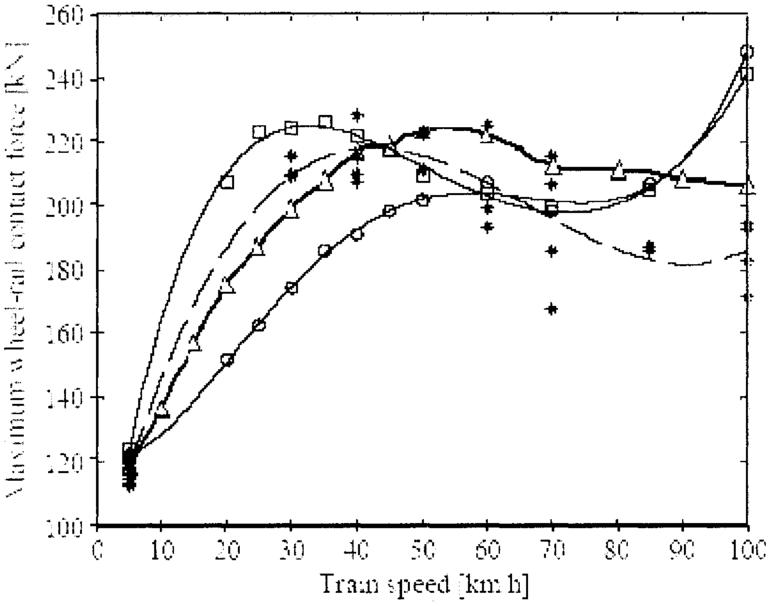

Figure 5.13: Comparison of impact load due to a 100 mm long, 0.9 mm deep wheel flat
Δ: present investigation; *: experimental data; □: nonlinear track model by Nielsen;
○: linear track model by Nielsen

5.4 A PARAMETIC STUDY ON IMPACT LOAD

The proposed roll-plane vehicle model and 3D linear track model along with adaptive contact model is finally used in this chapter to carry out a detailed parametric study. Effect of various vehicle and track parameters on the impact load due to a single flat on one of the wheels is examined systematically. The carbody weight *W* used here is

2100 ton which is approximately equal to a typical freight car axle load. The baseline parameters for the vehicle and track system used by Canadian Pacific Railway and obtained from [1] are presented in Table 5.1. One parameter is varied at a time while the others are held constant and equal to their nominal values.

5.4.1 Effect of Vehicle Load

Vehicle load is an important operating parameter for freight car as it may operate from empty for fully loaded conditions. In this study, using roll-plane vehicle model, the load *W* represents quarter of the total car load. The wheel defect considered is a 75 mm long, 1 mm deep haversine flat and the operating speed is 50 km/h. The simulated impact loads for different vehicle load are presented in Figure 5.14. The cross wheel refers to the other wheel within the axle which is assumed to have perfect wheel profile. The result indicate that increasing the vehicle loading generally increases the impact load between wheel and rail and is consistent with the findings reported by other researchers [1]. The results from the roll plane vehicle model in Figure 5.14 further indicate that the contact force at the cross wheel also increases significantly as the loading is increased.

Figure 5.15 shows the results in terms of impact force factor, defined as normalized impact force with respect to static contact load. The results indicate that the impact force factor between defective wheel and rail decreases almost linearly as the vehicle load is increased. The impact force factor at the cross wheel, however, is unaffected by the vehicle load.

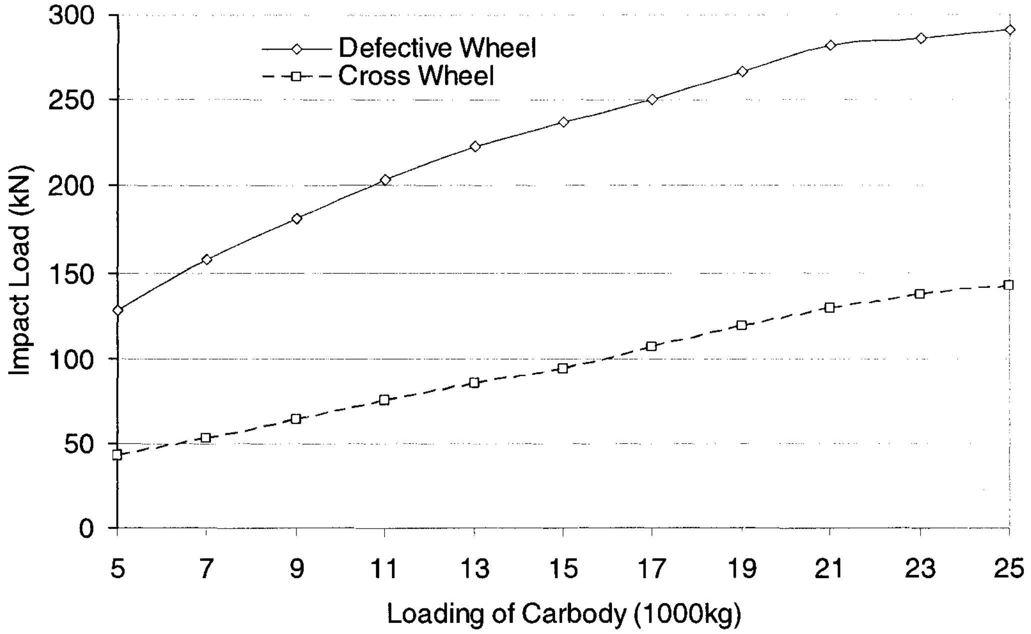

Figure 5.14: Effect of vehicle static load (quarter) on wheel-rail impact load

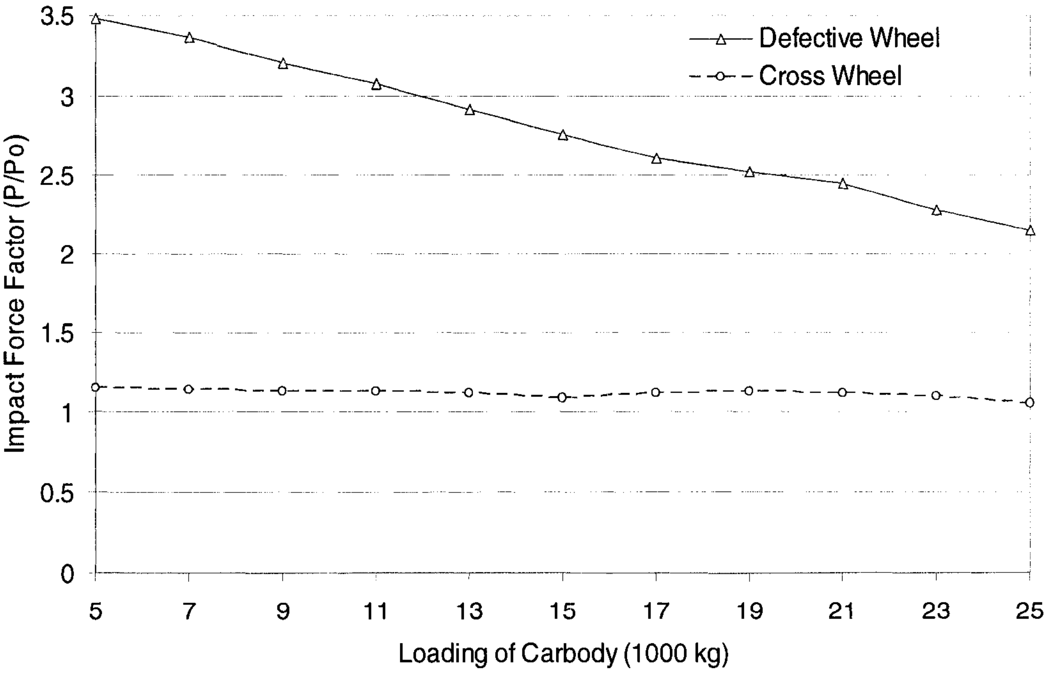

Figure 5.15: Effect of vehicle static load (quarter) on wheel-rail impact load factor

5.4.2 Effect of Wheelset Mass (Unsprung Mass)

The impact load depends on both the mass and velocity of the impacting objects. The effect of wheelset mass is thus investigated to examine its influence on the dynamic wheel rail impact. Figure 5.16 shows the effect of wheelset mass on the impact load induced by the flat. The impact load increases to some extent as the wheelset mass is increased. The influence of wheelset mass, however, is unnoticeable as the wheel mass is increased beyond 1300 kg. Although decreasing unsprung mass can reduce the impact load and improve vertical dynamic performance to some extent, its load carrying capacity severely restricts any scope in practice.

For the nominal wheelset mass, the effect of its mass moment of inertia in the roll plane is investigated in Figure 5.17. Mass moment of inertia of wheelset has little or no effect on impact load on the side of wheel with flat, but has noticeable effect on the wheel rail impact force at the cross wheel. The result shows increasing the mass moment of inertia of the wheelset reduces the peak dynamic load at the cross wheel to some extent. This can be attributed to reduced roll motion of the wheelset during the impact sequence.

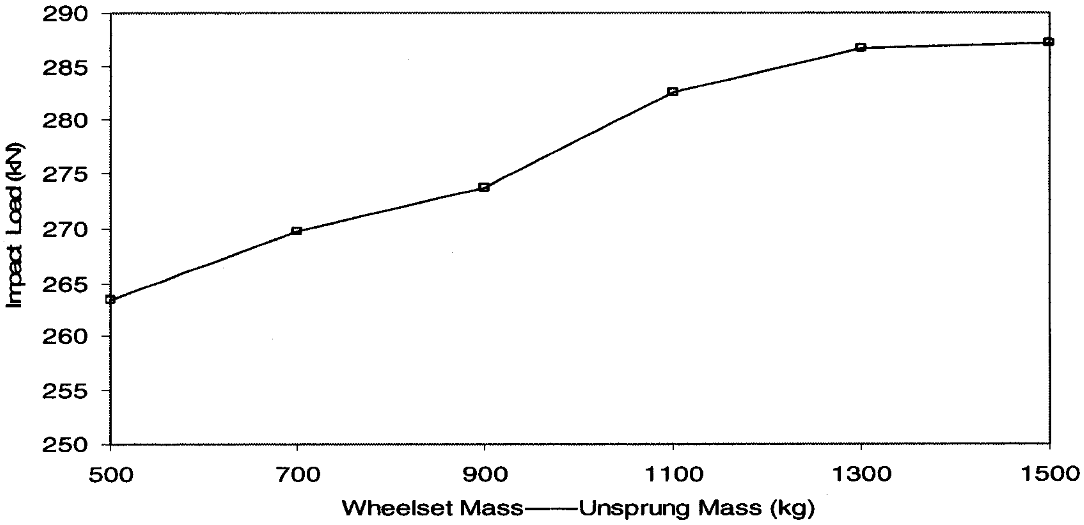

Figure 5.16: Effect of wheelset mass on wheel-rail impact load

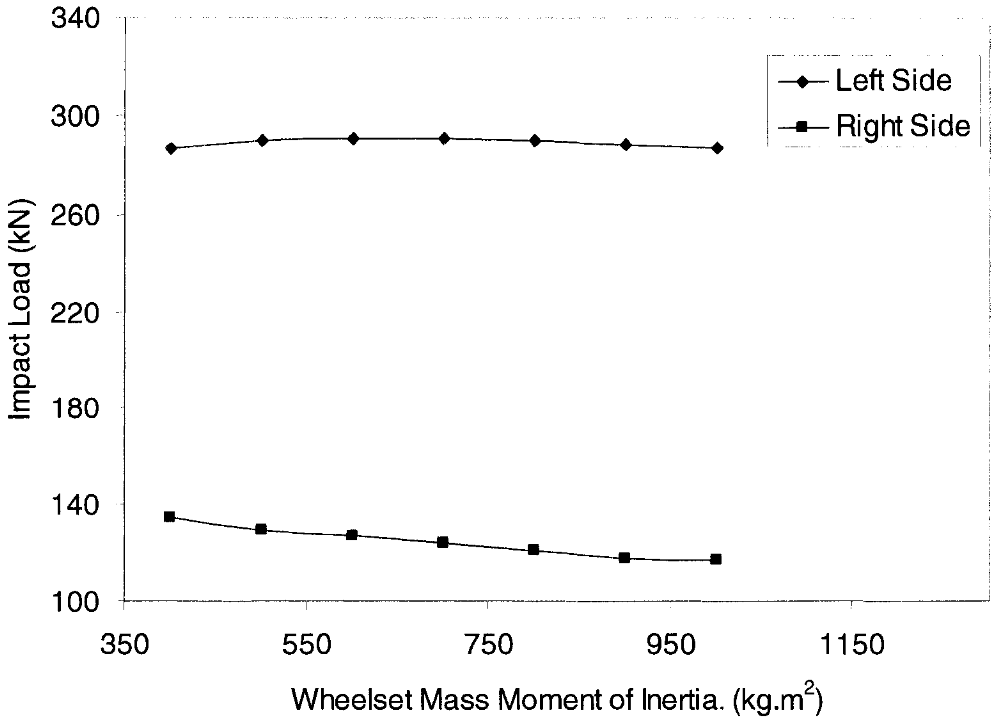

Figure 5.17: Effect of wheelset mass moment of inertia on wheel-rail impact

5.4.3 Effect of Vehicle Speed

The effect of vehicle speed on wheel rail impact loads due to a 100 mm long, 1.5 mm deep flat and a 75 mm long, 0.8 mm deep flat is illustrated in Figure 5.18. It can be seen that the impact load at the defective wheel increases rapidly as the vehicle speed is increased from 5 to 50 km/h, and keep slowly increasing form 50 km/h to 80km/h. For a speed beyond 80 km/h, the impact force decreases with increasing speed. This is due to reduced period of contact with the defect when the speed is high. It can be further noted, that the impact load increase significantly with the increase in flat size. Consequently, the reduction in the impact load for higher speeds is more noticeable for the larger flat size.

As shown in Figure 5.18, the cross wheel force response is affected by the vehicle speed in a similar manner but to a much less extent. In this case the peak occurs around 45 km/h which may coincide with the roll natural frequency of wheelset.

In this study, the local peak that many researchers stated [1, 2, 9, 24, 35, 37, 43] at speed 30~40 km/h is not observed. These researchers stated that the peak value possibly related to resonance when the track natural frequency is close to the excitation frequency due to the sinusoidal assumption of wheel flat. The so-called local peak value, however, is also not appeared in the experimental result [29, 41] and some numerical simulation [33].

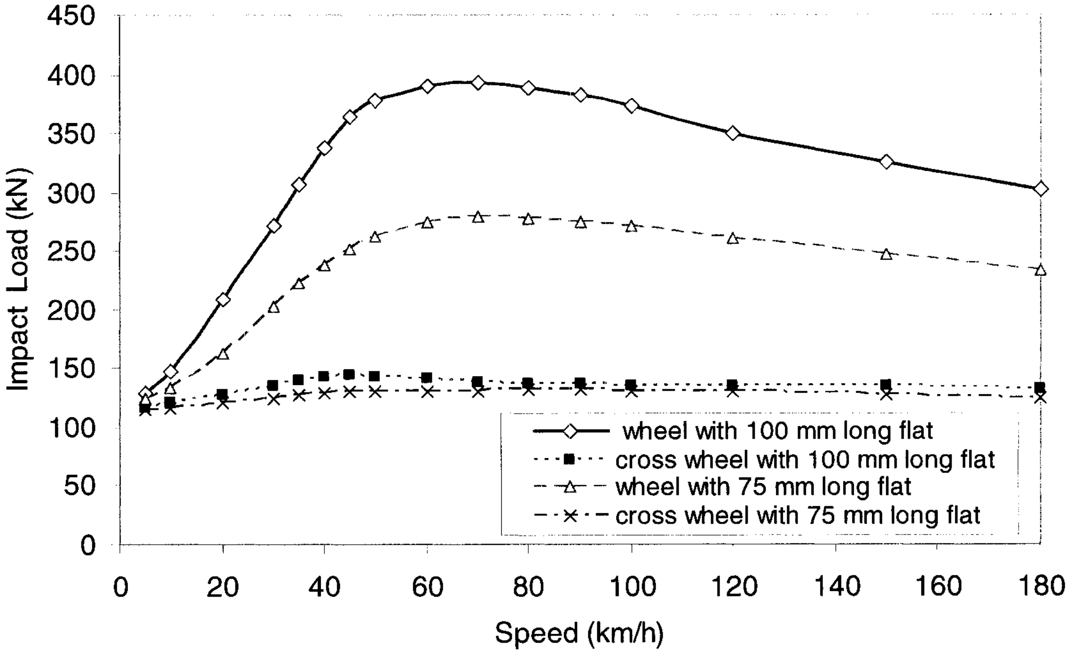

Figure 5.18: Effect of vehicle speed on wheel-rail impact load

5.4.4 Effect of Primary Suspension Stiffness and Damping

The bearing adapter between the wheelset and sideframe is treated as the primary suspension for freight bogies. In practice, there is no intentional primary suspension in most of North American freight car system. It is, however, modeled as parallel spring and damper to account for any compliance. Effect of the parameters of primary suspension on impact load for forward speed 60 km/h has been evaluated and presented in Figure 5.19 and 2.20.

Figure 5.19 shows that primary suspension stiffness has slight effect on the wheel-rail impact load due to wheel flat only when less than 250 MN/m, where the variation of impact loads is less than 7%. Above 250 MN/m, primary stiffness almost has no effect on the impact force, as the stiffness is very high. In practice, the primary stiffness is very large and it is evident that introducing a primary suspension with softer characteristic will hardly show any noticeable improvement for wheel-rail impact load due to flat.

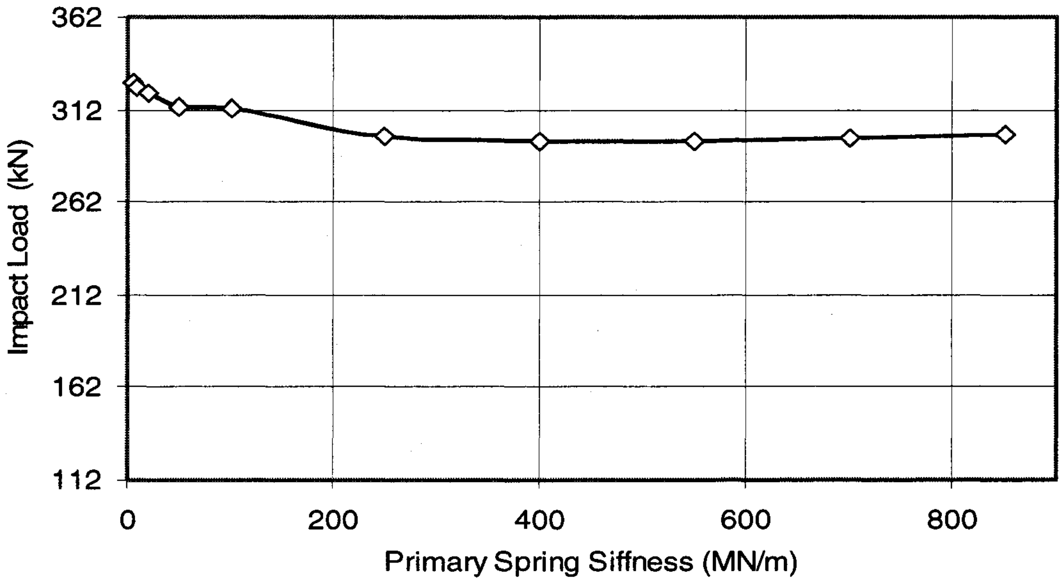

Figure 5.19: Effect of primary spring stiffness on wheel-rail impact load

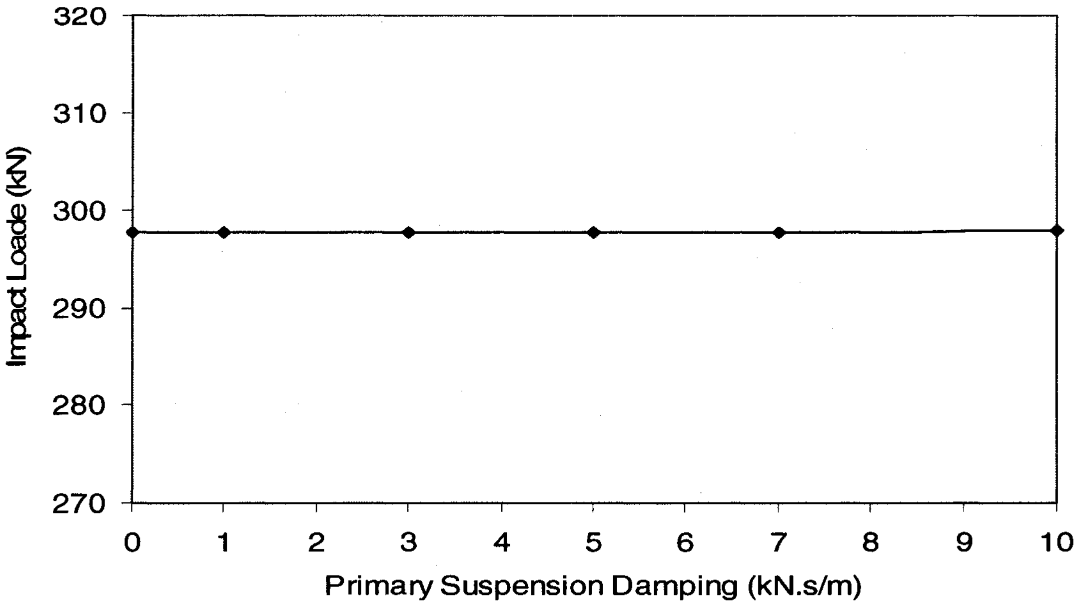

Figure 5.20: Effect of primary damping on wheel-rail impact load

Figure 5.20 presents the effect of primary suspension damping on the impact load for same forward speed and flat size. This result, as expected, shows no effect of primary suspension damping since the baseline stiffness for the suspension is very high. This trend for this parameter is consistent with those examined by other researchers [1].

In freight operation, bearing failure is a major concern. The bearing force as a result of wheel rail defect is thus considered as important performance measure. The effect of variation in the primary stiffness on the bearing force due to wheel flat is therefore examined and presented in Figure 5.21. As the result shows, there is a potential for significant improvement of bearing force by reducing the primary stiffness below 300MN/m. This can be easily achieved by mounting a rubber pad between the bearing adapter and sideframe. Although such change in primary stiffness will cause slight increase in the impact load at the wheel-rail interface (Figure 5.19), the improvement that can be achieved for the bearing force is very significant (Figure 5.21).

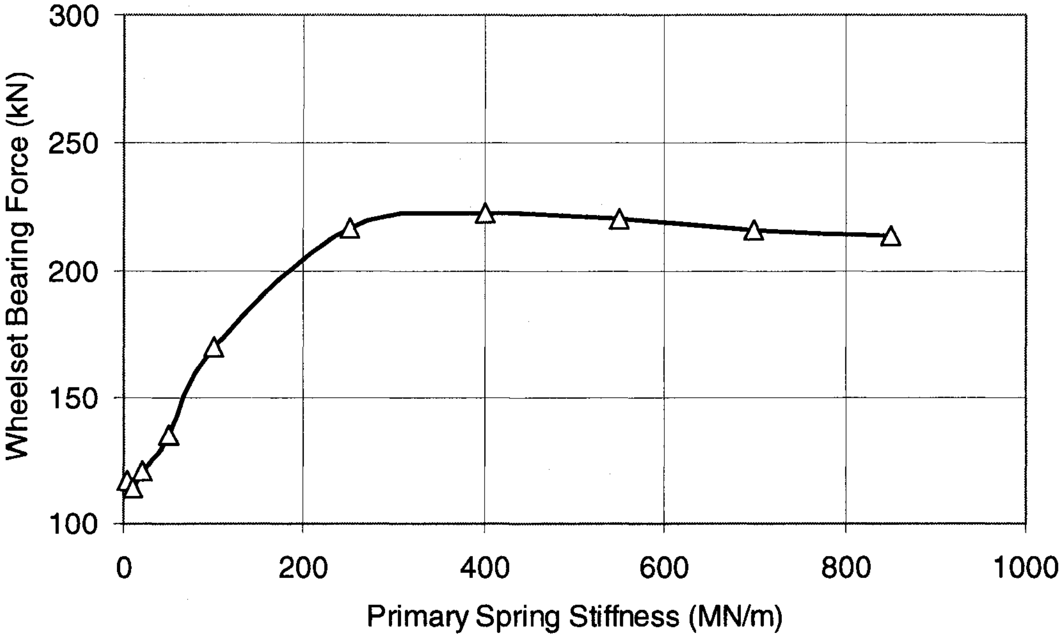

Figure 5.21: Effect of primary spring stiffness on wheelset bearing force

5.4.5 Effect of Secondary Suspension Stiffness and Damping

Effect of secondary suspension parameters on the wheel-rail impact load at forward speed 60km/h has been investigated and plotted in Figurer 5.22 and 5.23. The results show that the impact force due to wheel flat is not affected by the secondary suspension parameters in any significant manner.

5.4.6 Effect of Flat Size

A flat segment for a railway wheel is defined by its length (l_f) and depth (D_f). For a freshly formed flat on circular wheel, the length and depth are related to each other as discussed in Chapter 2. However, as the edges of the flat wear out with use, a fresh flat quickly becomes a rounded flat, and the effective length of the flat may increase for the same depth. From practical point of view, however, there is a constraint on depth for a possible range of length. In examining the effect of flat size in this investigation, the depth is varied between 0.5 and 2.0 mm, while the length of flat is varied between 50 and 150 mm for each depth considered.

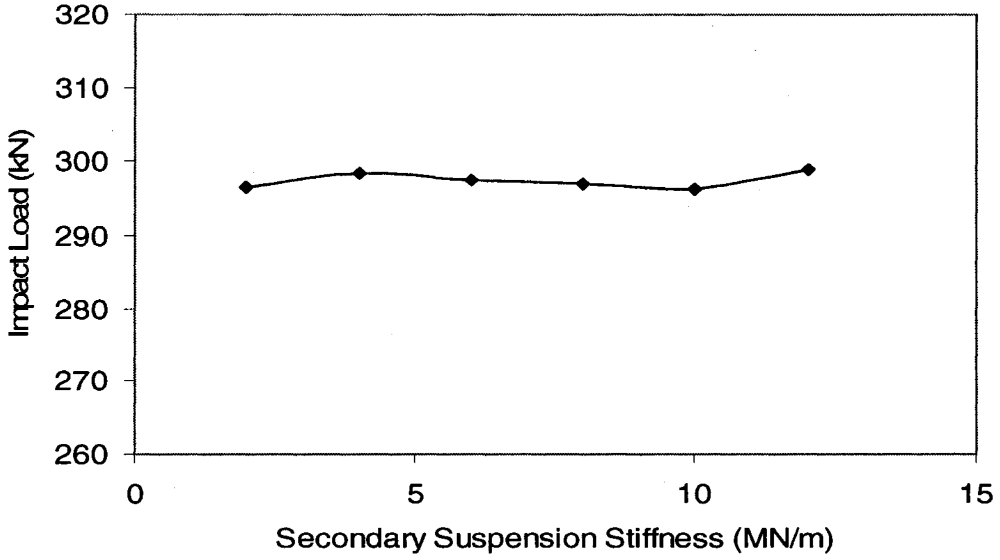

Figure 5.22: Effect of secondary suspension stiffness on wheel-rail impact load

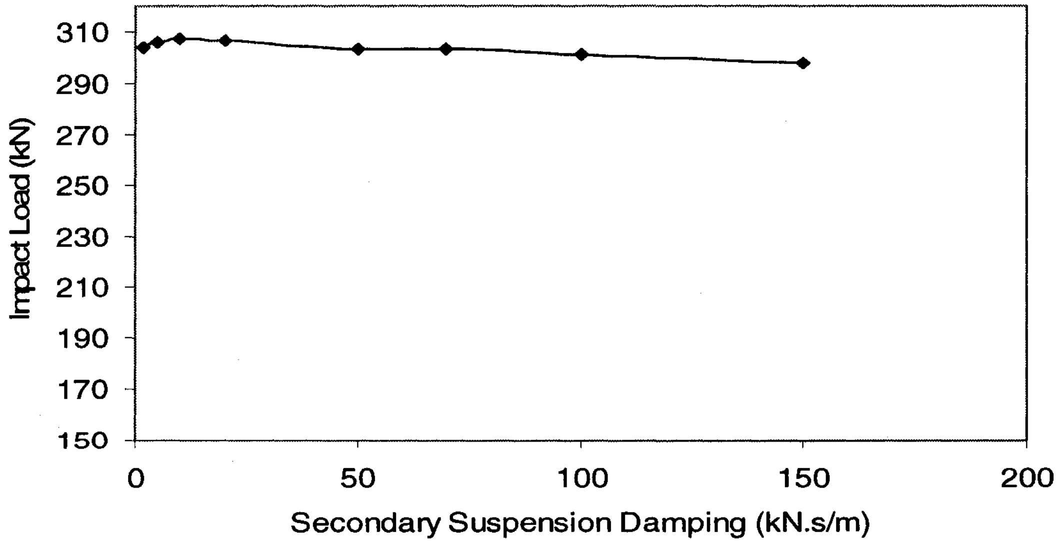

Figure 5.23: Effect of secondary suspension damping on wheel-rail impact load

The resulting impact loads at speed of 70 km/h are presented in Figure 5.24. This figure indicates that for a given depth of flat, there is a critical flat length at which the impact load reaches its maximum value at the given speed. The deeper the flat is, the longer the critical flat length is. Meanwhile, for a given flat length, the deeper the flat is, the larger the impact load is. It also can be seen that the impact load at the given speed is much more sensitive to the flat depth than to the flat length. The industry is in search of threshold for flat that should be used for maintenance and replacement of wheelsets. The result obtained has indicated that the flat length alone is not an adequate indicator and that both length and depth should be taken into account in determining the threshold.

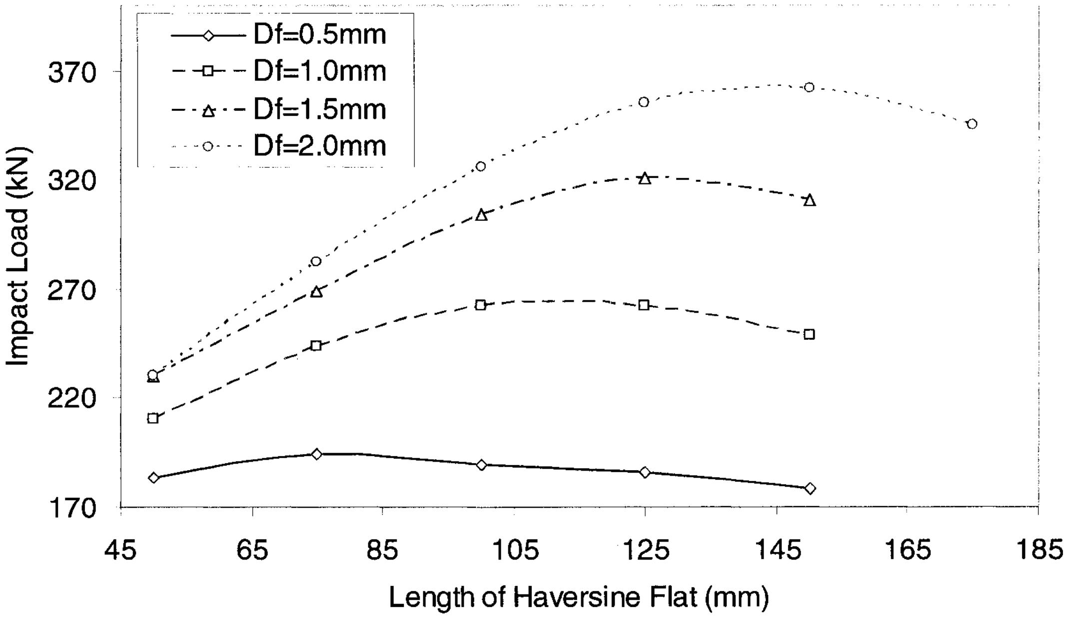

Figure 5.24: Effect of flat size on wheel-rail impact load

5.4.7 Effect of Rail Mass

Rail mass is defined by its mass per unit length and has a nominal value of 67.57 kg/m in this study. Figure 5.25 shows the effect of rail mass on the wheel-rail impact loads due to a 75mm long, 1mm deep wheel flat at 40, 70 and 90 km/h. The results indicate that a reduction in rail mass per unit length generally reduces the impact load. This benefit however, diminishes after a certain reduction. For example, reducing the rail mass below 50 kg/m will not provide any benefit at most speeds. To get a sense of magnitude, it is found that at 70 km/h, a reduction of rail mass by 30% will improve impact load by less than 8%. The trend of increased impact load with increasing rail mass is an important insight since the industry trend to replace previous rail with new heavy rail to accommodate heavier freight train. Both these factors will result in an increase in the impact force from wheel flats.

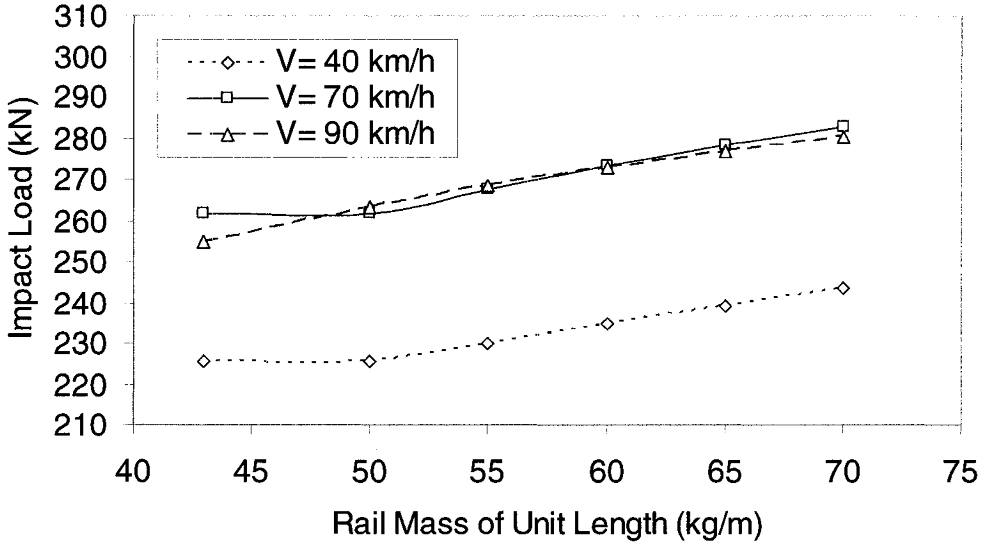

Figure 5.25: Effect of rail mass of unit length on wheel-rail impact load

5.4.8 Effect of Sleeper Mass

Sleeper mass is a parameter that depends on the type of sleeper material (wood or concrete) used in a track system. Figure 5.26 shows the effect of sleeper mass on the wheel-rail impact loads due to a 75 mm long, 1 mm deep wheel flat at 40, 70 and 90 km/h. As the results show, the influence of sleeper mass on the impact load due to wheel flat is not very significant, and the trend is different at low speeds from those at high speeds. At low speeds, the impact load increases slightly as the sleeper mass is increased. The opposite trend is observed at high speeds. Since magnitude of impact force is of concern, it is preferable to opt for heavier sleeper for a track system.

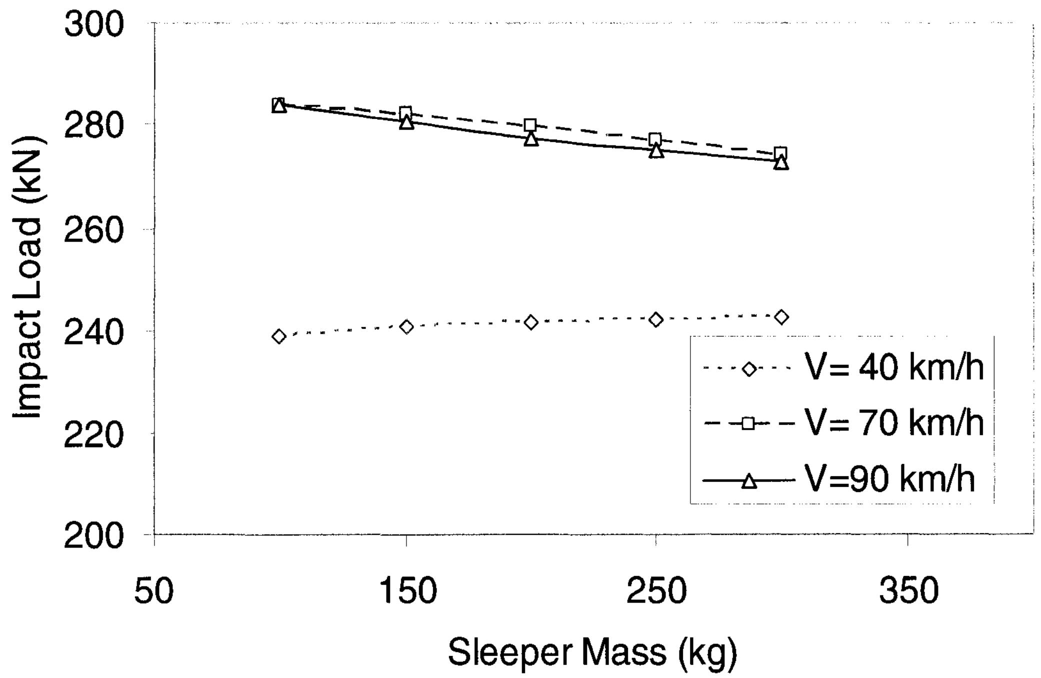

Figure 5.26: Effect of sleeper mass on wheel-rail impact load at different speed

The effect of sleeper mass on the cross wheel is found to be more significant, where the magnitude, however, is much less. Figure 5.27 shows the effect of sleeper mass on the impact load at the cross wheel. As the sleeper mass increased from 100 to 300 kg, the impact load at the cross wheel increases from 112 kN to 138 kN. Such characteristic is expected since sleeper is the primary coupler between the left and right rail of the track system.

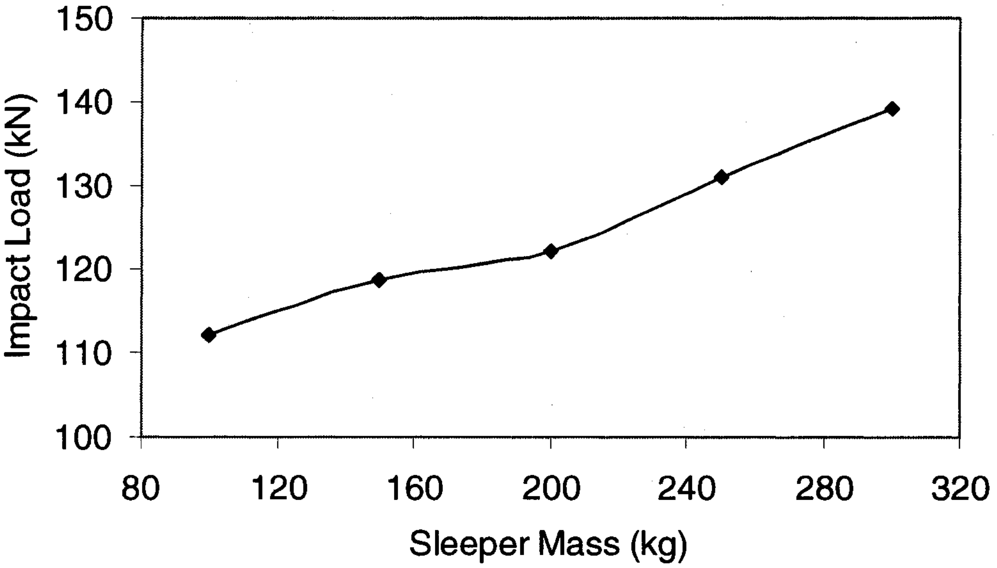

Figure 5.27: Effect of sleeper mass on the impact load at cross wheel (70 km/h)

5.4.9 Effect of Rail-pad Stiffness

Rail-pad is the element used at the interface between rails and sleepers that can provide some isolation of vibration. The effect of rail-pad stiffness on the wheel rail impact loads is investigated at speed of 40, 70 and 90 km/h as shown in Figure 5.28. At low speeds, larger value of rail-pad stiffness leads to slight increase in the resulting impact load. For the lower values of pad stiffness considered, it appears that there exits an optimal pad stiffness that may minimize the impact load. This will, however, require a multi objective optimization including other operating parameters such as vehicle loads and flat sizes.

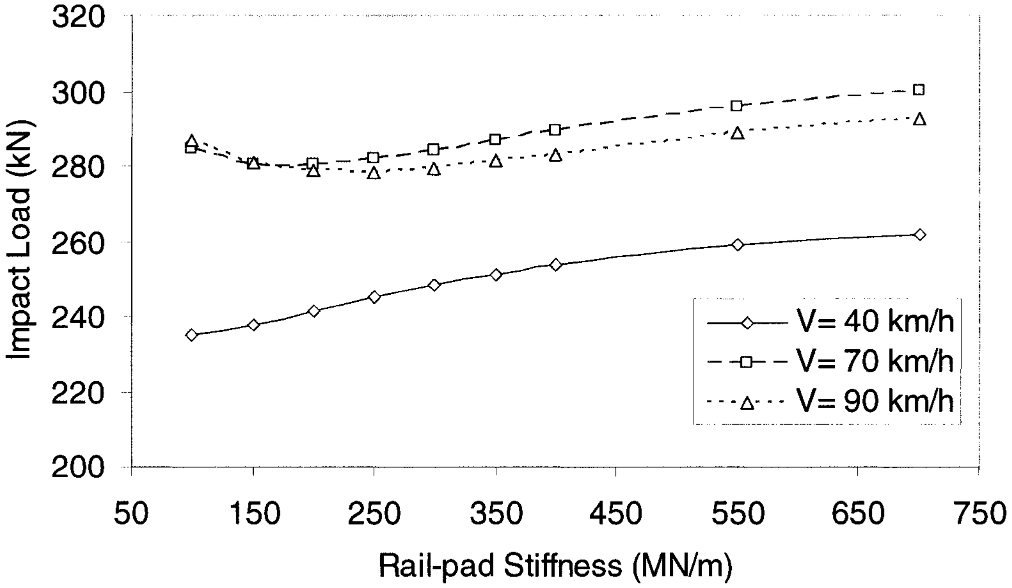

Figure 5.28: Effect of rail-pad stiffness on wheel rail impact load

5.4.10 Effect of Ballast Stiffness

The final parameter investigated is the ballast stiffness or softness of the ballast over which the sleepers are supported in a track system. Figure 5.29 shows the effect of ballast stiffness on wheel-rail impact load due to wheel flat at three different speeds. Impact load is more sensitive to ballast stiffness at low speeds than at higher speeds. In all cases, however, an increase in ballast stiffness reduces the impact load to certain degree. Further more, the improvement saturates as the ballast stiffness approaches high value. In general, stiffer ballast layer is preferable for improved impact load performance.

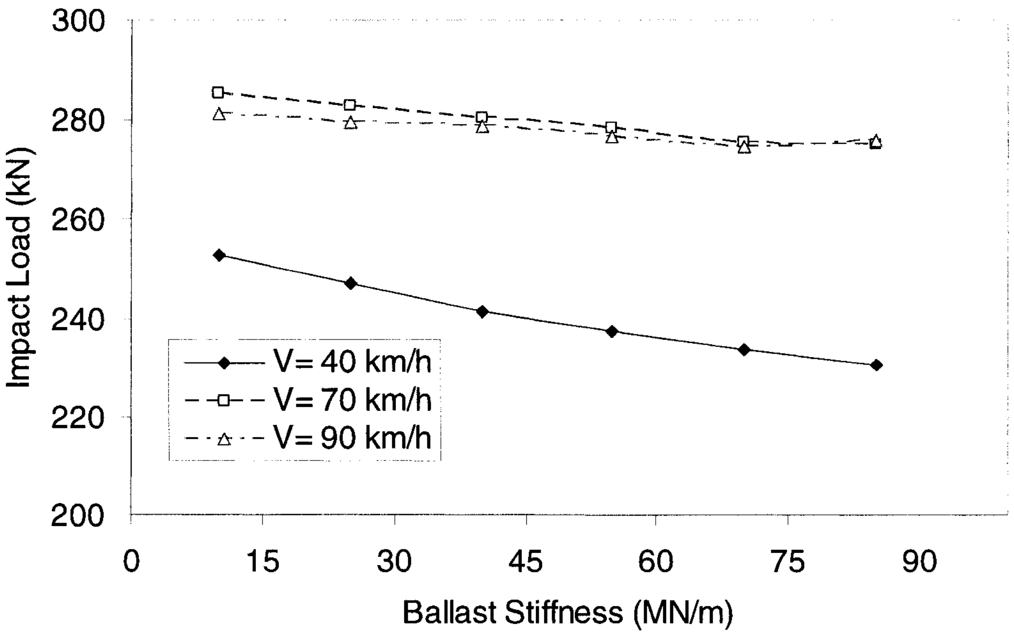

Figure 5.29: Effect of ballast stiffness on wheel rail impact load

5.5 SUMMARY

The adaptive contact model, roll-plane vehicle model and two layers 3D track model are combined to study the wheel-rail impact load due to single flat in this chapter. The response to the geometry excitation at vehicle track interface is examined. Results are compared with reported experimental and computational data in time domain to examine the effectiveness of the adaptive contact model and roll plane vehicle model together with 3D track model. The effects of vehicle and track system on the impact load due to a single wheel flat are thoroughly investigated for both defective wheel and the cross wheel.

The results demonstrate that adaptive contact model is more realistic for accurate representation of the contact between wheel and rail. The comparative study shows that the proposed model, although simplified in terms of vehicle and track systems, can predict wheel-rail impact load better than nonlinear Hertzian point contact model.

This study shows that wheel flat can cause wheel-rail impact load not only between the defective wheel and rail, but also between the rail and cross wheel. The impact loads due to a flat is strongly influenced by vehicle loading (axle load), speed and defect size. Vehicle suspension properties have little effect on the wheel-rail impact load, while primary stiffness has noticeable influence on the interaction force between wheelset and sidefame (bearing force). Impact position with respect to sleeper support has slight effect on the magnitude of impact force.

The resonance phenomena observed in several previous investigation of wheel flat response was not observed in this investigation and is also not apparent in any field test data available. Based on the studies presented in the previous and current chapters, the following is concluded. When perfect wheel travels on rail, the vehicle track system move up and down due to sleepers and spans of the track system, and one can identify an increase in the contact force at some speeds related to resonance. However, when there is a major defect on the wheel, such as a flat, the impact forces are significantly higher than those contact force variation. Therefore, it is likely that when the impact force due to a flat is examined there will be negligible influence of any resonance behavior.

The present study also showed that a flat on one side of the wheelset have considerable influence on the cross wheel contact force, although its magnitude is significantly less than that of the wheel with flat. The cross wheel force is also found to be function of wheelset and sleeper parameters.

CHAPTER 6

IMPACT LOAD DUE TO MULTIPLE WHEEL FLATS

6.1 INTRODUCTION

Multiple wheel flats within a wheel or axle of a freight car is commonly found. Due to locking of brake system, flats may be developed at the same position of both wheels within an axle. On the other hand, the wheel of one side may have several flats because of the failure of brake system. The number of flats and their location with respect to each other may play a roll on the peak impact load developed due to multiple flats as compared to a single flat. If two flats are very close to each other, they may act as a single flat of larger length while the depth of the flat is small. On the other hand, for a given phase between two flats, speed may play further role, as the time between each flat entering the contact patch is affected by the speed.

Over the years, railway industry has been trying to establish a threshold of flat size as an indication of requirement for maintenance or replacement. Establishment of a reliable threshold is essential to ensure safety of operation while cost of maintenance is minimized. Most wheel removal criteria are based on single or multiple adjoining flats within a wheel.

According to current practice, Transport Canada requires replacement of the wheel if two adjoining flats are more than 2 inches (50.80 mm) [25] each. In U.S.A, AAR Rule 41-Section A [13] does not allow a wheel with two or more adjoining flats each 1½ inch (38.1mm) or over in length to continue to be in service. The possible existence of flat on both wheels within the axle is not dealt with by any of the requirements.

As far as the impact load and damage due to multiple flats are concerned, there is not much that can be found in the literature. Furthermore, the effects of flats on each wheel requiring a roll plane vehicle model and 3D track system model has not been investigated. Multiple flats on same wheel will cause multiple wheel-rail impact forces in every revolution of wheel. The resulting sequence of multiple impact loadings within one cycle of wheel rolling is not clear by far. Moreover, the effect of phase angle between two flats in combination with forward speed may exhibit response of interest.

In this chapter, the combination of adaptive contact model, 2D roll plane vehicle model and 3D track model are employed to investigate the wheel-rail impact load due to multiple flats. Two scenarios of multiple flats are considered in this investigation. One deals with two same or different size flats within a wheel defined by their size and the angle between them. The other one deals with single flat on each wheel of the same axle. In each case, the results are compared with those of a single flat simulations presented in Chapter 5.

6.2 MODEL OF MULTIPLE FLATS

As discussed in Chapters 1 and 2, when a new flat is developed on a railway wheel, it takes the form of a chord. With use, the edges of the flat soon become rounded and it is more appropriate to describe them by a sinusoidal function. In this work, commonly used haversine model is utilized to study the multiple flats as was the case for single flat considered in Chapter 5. Description of two flats within the same wheel and single flat on each wheel of the axle is presented in the following subsections.

6.2.1 Model of Two Flats on Same Wheel

The contact model developed in Chapter 2 is extended to included two flats within the same wheel. Figure 6.1 shows the wheel profile with two flats located at angle α_{o1} and α_{o2} from the vertical centerline. The length of the flats which can be different is defined by angle φ. Similar to equation (2.10), the instantaneous radius of the wheel at an arbitrary point can be expressed by:

$$R_i = \begin{cases} R_w & 0 < \alpha \le \alpha_{01} - \varphi_1 \\ R_w - f_1 & \alpha_{01} - \varphi_1 < \alpha \le \alpha_{01} + \varphi_1 \\ R_w & \alpha_{01} + \varphi_1 < \alpha \le \alpha_{02} - \varphi_2 \\ R_w - f_2 & \alpha_{02} - \varphi_2 < \alpha \le \alpha_{02} + \varphi_2 \\ R_w & \alpha > \alpha_{02} + \varphi_2 \end{cases} \tag{6.1}$$

Where f_1 and f_2 are the variations of the wheel radius due to wheel flats, and can be determined by equation (2.14), (2.15) and (2.16) for haversine flats.

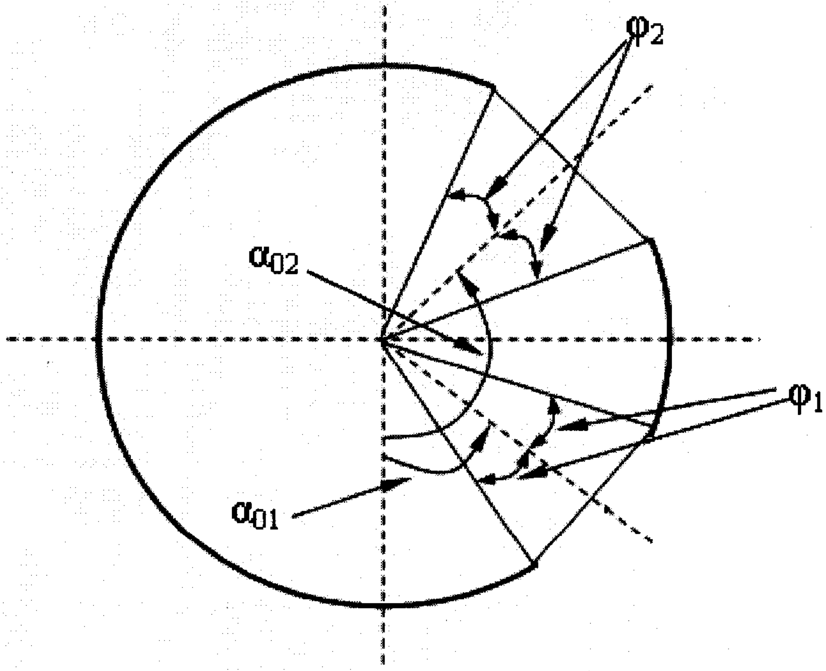

Figure 6.1: Wheel profile with two flats

The position of one flat with respect to the other is a variable of interest in this investigation which is defined by (α_{o2}-α_{o1}), and is referred to as the position phase angle.

6.2.2 Model of Two Flats on Opposite Wheels

From practical point of view, when a flat is formed due to locked brake system for an axle, two very similar flats at the same location of both wheels are common.

Figure 6.2 presents an axle with two wheels where identical or different flat may be formed on each wheel at same location with respect to a vertical centerline. Since only one flat is considered per wheel, the formulation is identical to those presented in Chapter 2. The instantaneous radius for each wheel can be formulated using equation (2.10) in combination with (2.14), (2.15) and (2.16).

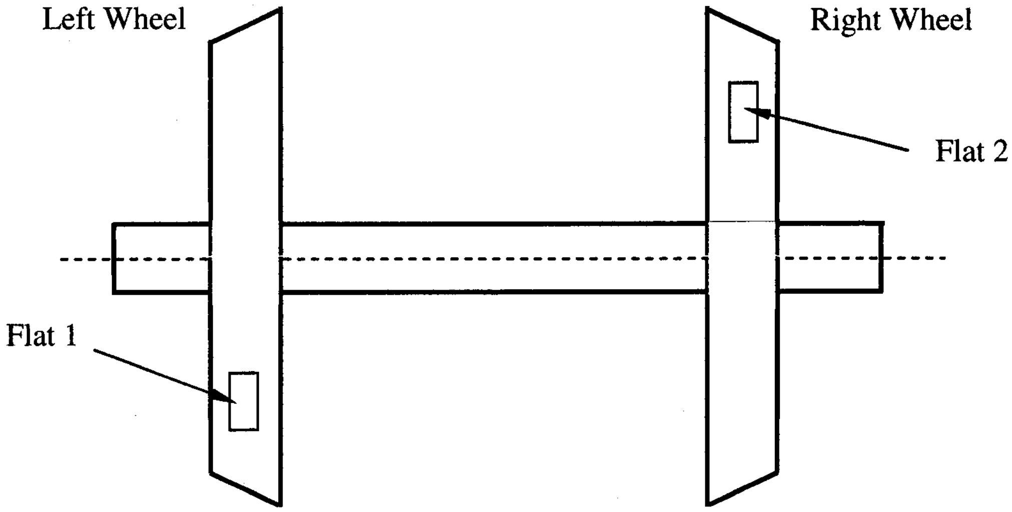

Figure 6.2: Two flats on two opposite respective wheels

6.3 DYNAMIC RESPONSE DUE TO TWO FLATS ON ONE WHEEL

Two different flats are defined for the analysis of dynamic response due to multiple flats. Flat 1 is a 75 mm long flat with depth of 1 mm. Flat 2 is a 60 mm long flat with depth of 0.8 mm. The flats are defined such that flat 1 comes into contact first with the rail followed by flat 2 which enters the contact after a defined phase angle. The nominal value for the phase angle between these two flats is taken as 90°. The variation in radius of the wheel as a function of wheel position angle is illustrated in Figure 6.3. The position angle domain is $-180^{\circ}\sim180^{\circ}$, which is consistent with the definition of the coordinate described in Chapter 2 in calculating wheel-rail contact force by the proposed adaptive contact model.

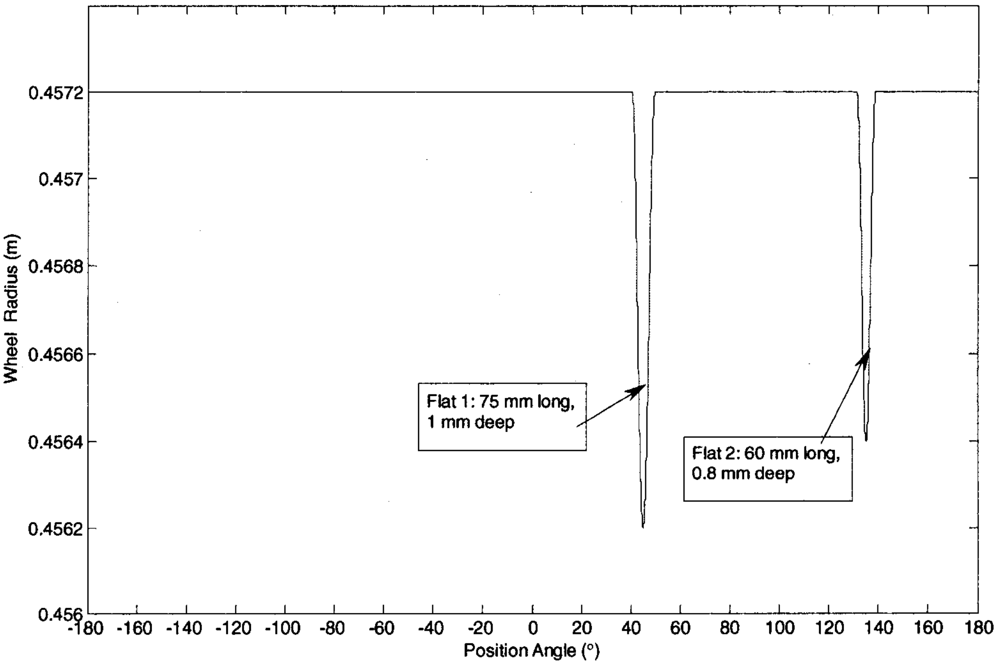

Flat 1: 75 mm long, 1 mm deep

Flat 2: 60 mm long, 0.8 mm deep

Figure 6.3: Profile of wheel with two flats in phase

The simulation is carried out for multiple flats on the left wheel at a forward speed of 50 km/h. The time history of contact forces at the left and right wheel-rail interface is shown in Figure 6.4. It can be seen that the wheel impacts rail twice every revolution. For the speed and phase angle considered, there is no noticeable influence of the first impact due to Flat 1 on the second impact due to Flat 2. The impact force due to single flat predicted earlier for same size flat is very similar to that predicted here for multiple flats that are far apart.

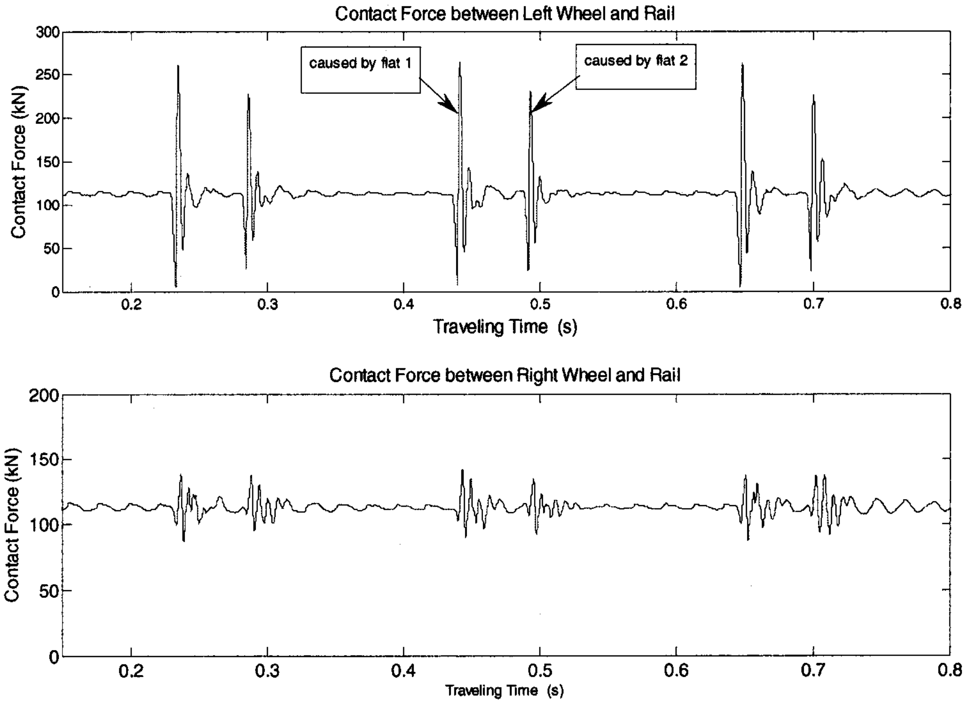

Figure 6.4: Time history of wheel rail contact force due to two flats

It can be further noticed that there is some variations in the impact magnitude from cycle to cycle, and is due to the variation of the location of impact with respect of sleepers. As the left wheel-rail impact due to flats, the right or cross wheel-rail interface also develops impact contact force similar to the left wheel but of significantly less magnitude. The corresponding wheel and rail displacements at the left side are shown in Figure 6.5. For the speed and flats considered, there is no lift-off of wheel from the rail.

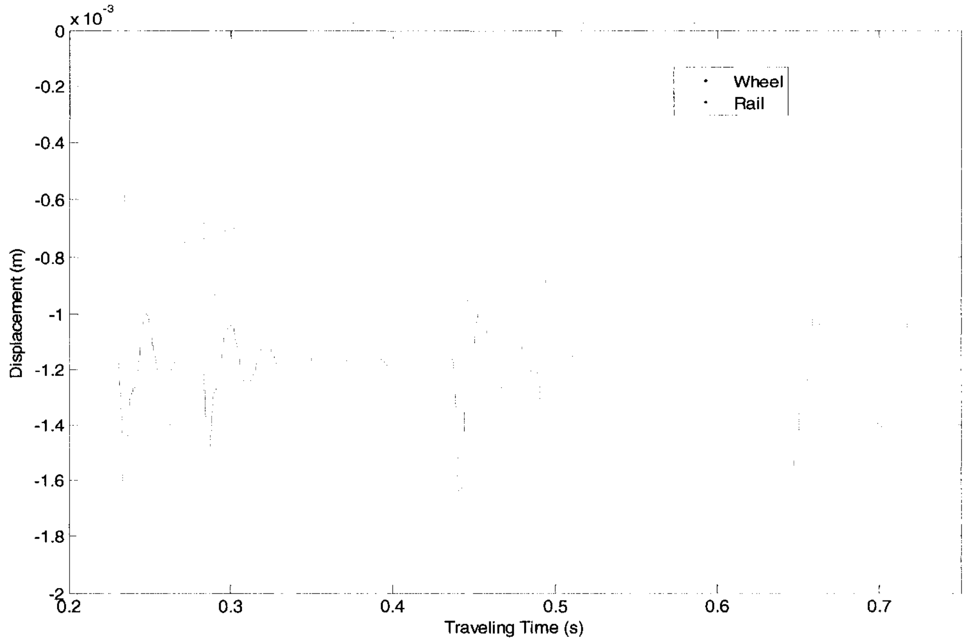

Figure 6.5: Time history of wheel rail displacement due to two flats

Although the results show that there is no influence of multiple flats on the magnitude of impact load due to a flat when they are far apart. The number of impact per revolution is a function of the number of flats. Multiple flats thus can contribute to fatigue damage to the components.

In a study of impact loads due to multiple flats, the obvious parameters that may have influence are the speed and phase angle. The effects of these two parameters are thus next examined in more details. In each case, the magnitude of the impact due to multiple flats is compared with those predicted due to single flat of same size.

Effect of Speed

The effect of speed on impact load due to multiple flats is investigated for two flats with position phase angle 90° (as shown in Figure 6.3). Flat 1 is 75 mm long and 1 mm deep. Flat 2 is 60 mm long and 0.8 mm deep. As discussed previously, Flat 1 comes into contact ahead of Flat 2. Figure 6.6 presents the peak impact load corresponding to Flat 1 and Flat 2 for speeds in the range of 10 to 150 km/h. The Figure also presents the impact loads due to same size single flat at different vehicle speed.

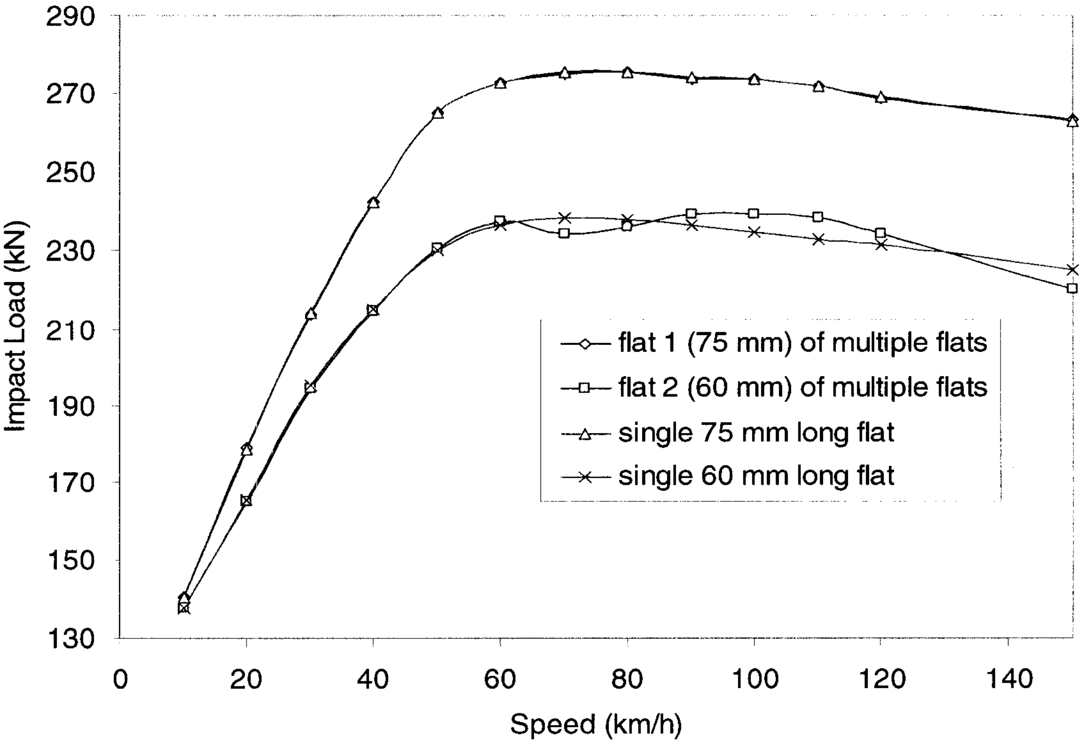

Figure 6.6: Effect of speed on impact load caused by two flats on one wheel (Phase angle between two flats is 90°)

The results show that the first of the multiple flats coming into contact with rail exhibits same impact force as those predicted by a single flat simulation of same size. For Flat 2 which is 90° apart from Flat 1, it also shown that there is no influence of multiple flats for speeds up to 60 km/h, as indicated in Figure 6.6. The results as shown further indicate that when operating at speeds above 60 km/h, the impact load due to Flat 2 following Flat 1 may be affected by the existence of Flat 1. The nature of the effect does not follow a definite trend and is difficult to explain as a combination between speeds and phase in combination with coupled vehicle track dynamics may have a contribution for such variation. It can, however, be concluded that under certain circumstances the impact load due to multiple flats can be slightly larger than those estimated from simulation of a same size single flat.

Effect of Phase Angle

The effect of relative position (phase angle) on impact load due to multiple flats is examined at vehicle speed of 40, 70 and 100 km/h. The impact loads corresponding to first and second flat with different position phase angle are predicated and compared with the impact load caused by same size single flat at same speed.

Figure 6.7 illustrates the effect of position phase angle on impact load corresponding to Flat 1 of multiple flat at 3 different speeds. The dash lines represent the impact loads due to the same size single flat at the given speeds. The effect of speed on impact load was discussed in Chapter 5, where it was shown that the impact load increases with speed and then drops slightly as speed reaches high value.

Figure 6.7 shows that multiple flats on a wheel have no effect on the impact load corresponding to first flat at any speeds as long as the phase angle between flats is greater than 20°. The impact load is almost same as that due to same size single flat. When two flats are very close (phase angle is 10°), the impact loads corresponding to first flat at medium and high speed are smaller than that caused by same size single flat at the same speed. This is consistent with the conclusion about the effect of flat size on impact. Increasing flat length reduces the impact load for certain flat depth when flat length is larger than the critical length, as discussed in Chapter 5. When two flats are very close, second flat effectively increases the equivalent length of first flat while the depth does not change.

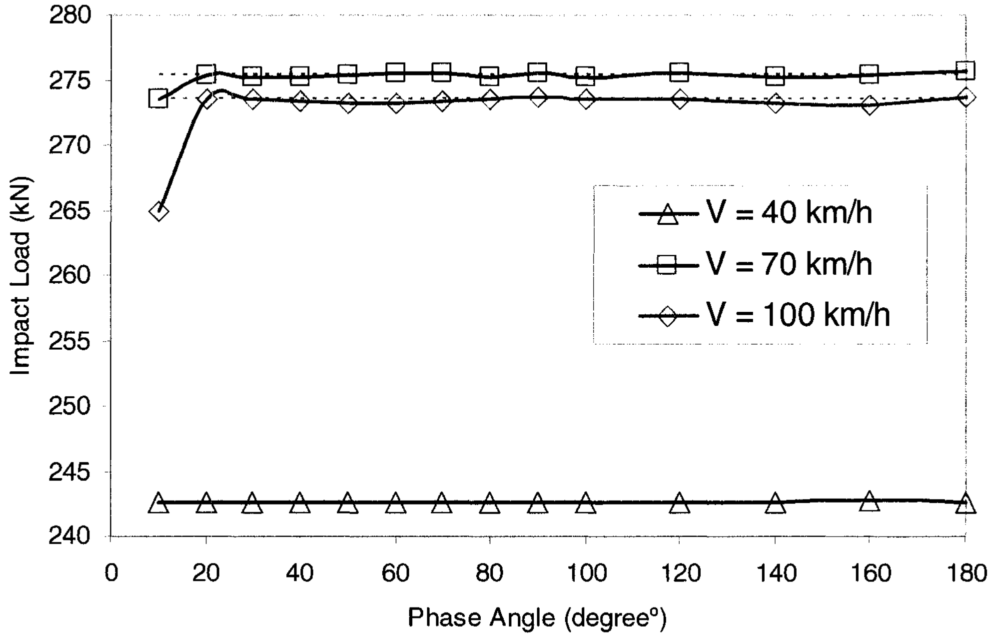

Figure 6.7: Effect of position angle on impact load caused by Flat 1 on a wheel with multiple flat (Flat 1: 75 mm long and 1 mm deep)

In Figure 6.6, it was shown that under certain condition, the second flat of multiple flats may generate different impact force from those of a single flat case. Figure 6.8 shows effect of phase angle on the impact load corresponding to second flat which enters the contact region after Flat 1.

The results show complex relationship between speed, phase angle as well as number of impacts within a sleeper span. In general, the impact due to the second flat on a multiple-flat wheel is significantly affected by the phase angle, when the phase angle is small. A critical phase angle can be defined as the value of phase angle until which the impact load due to second flat is affected. At 40 km/h this can be clearly identified as 60°

as shown in Figure 6.8. Beyond this value of phase angle, the impact due to the second flat is same as that predicted by simulation of single flat of same size.

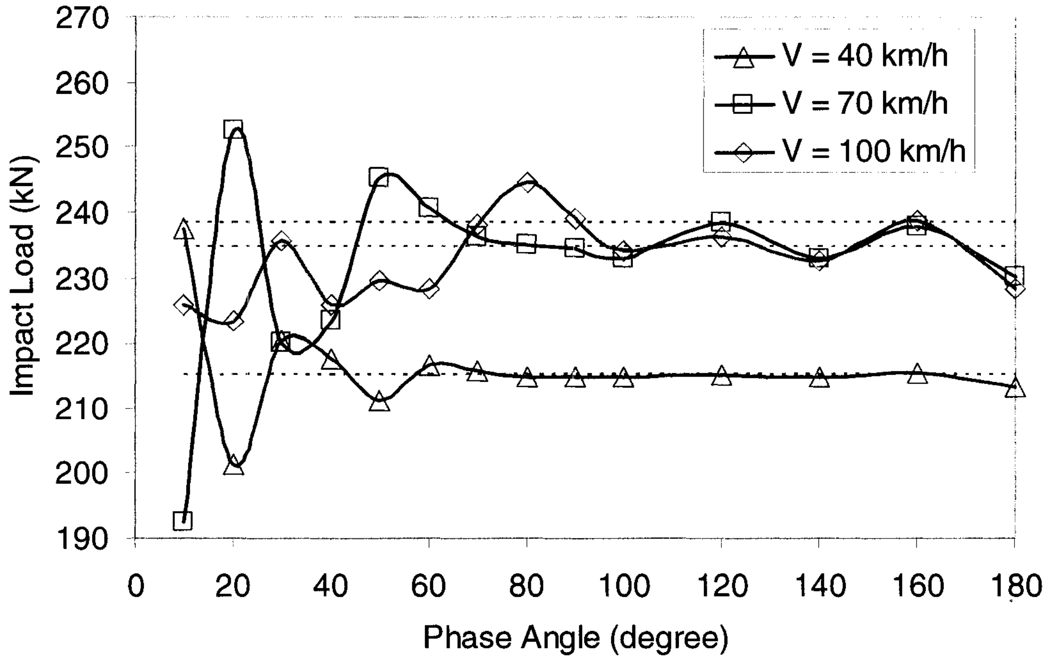

Figure 6.8: Effect of position angle on impact load caused by Flat 2 on a wheel with multiple flat (Flat 2: 60 mm long and 0.8 mm deep)

With an increase in operating speed, the critical phase angle increases as was established for 70 and 100 km/h presented in Figure 6.8. The results further show that for the pair of the flat considered, there is a value of phase angle where largest impact due to second flat is generated. This phase angle corresponding to largest impact load is also function of speed, and is found to increase as the operating speed is increased. It is likely that the results generated in Figure 6.8 cannot clearly identify the largest impact and corresponding phase angle since simulation was carried out at discrete phase angle at steps of 10°.

This study, however, shows that two or more flats on same wheel maybe cause wheel-rail impact load larger than that due to a same size single flat. AAR Rule-41A and

Transport Canada require the wheel with "adjoining flat each of which is bigger" than threshold should be removed from service. But there is no definition for "adjoining flats". Based on the preliminary results generated here, it appears that the phase between adjoining flats should also be included in the criteria for removal of wheels from service.

6.4 DYNAMIC RESPONSE DUE TO SINGLE FLAT ON BOTH WHEELS

A more commonly occurred case of multiple-flat on railway wheel is where one flat is formed on each wheel of an axle. These flats will typically occur at same location, however, may be different in size. This section is devoted to the investigation of impact load due to above defects, as well as possible phase between the flat at the left and right wheels. In each case the results are compared with those generated from same size single flat at one wheel only.

6.4.1 Two Same Size Flats on Opposite Wheels at Same position

When the wheel flats are caused by the sliding of locked wheelset, it is common that one wheel flat is accompanied by another one on opposite wheel at same position. In this subsection, the impact loads due to two same size flats on opposite wheels at same position are investigated. The flat considered is 60 mm long and 0.8 mm deep. The profile of these two opposite wheels is illustrated in Figure 6.9.

Figure 6.10 presents the corresponding impact loads at the left and right wheel-rail interface for speed of 50 km/h. As the results show, the wheelset develops identical impact contact force at both wheels due to symmetric flats. At this speed, the magnitude and trend of the contact force on each wheel is very similar to those predicted by single flat on that wheel only. Figure 6.11 presents the corresponding wheel and rail displacements at the left and right side. These results further show that, at this speed, there is no separation of the wheel from rail for the flat size considered.

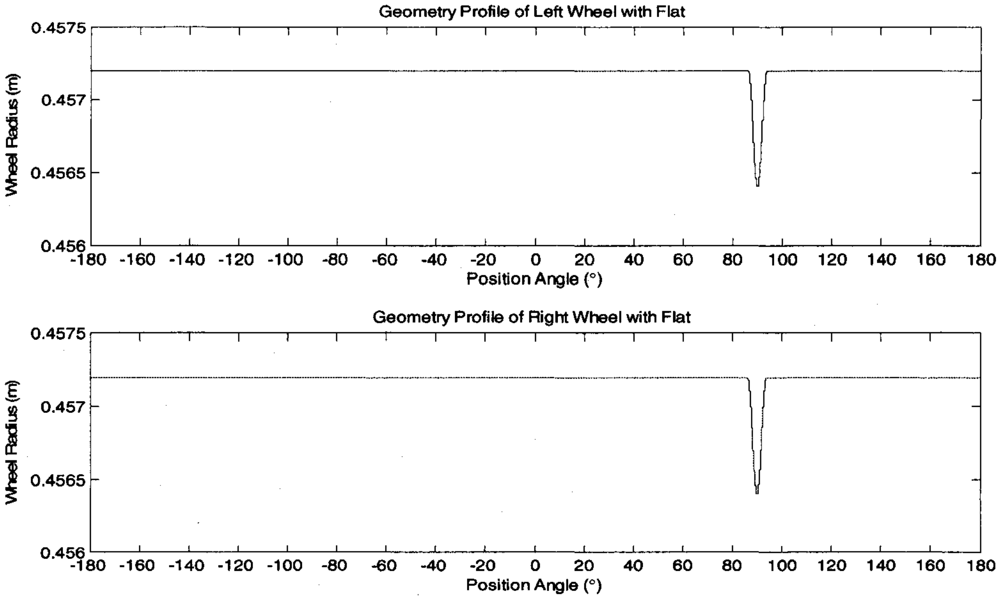

Figure 6.9: Profile of two opposite wheels with same size flat at same position

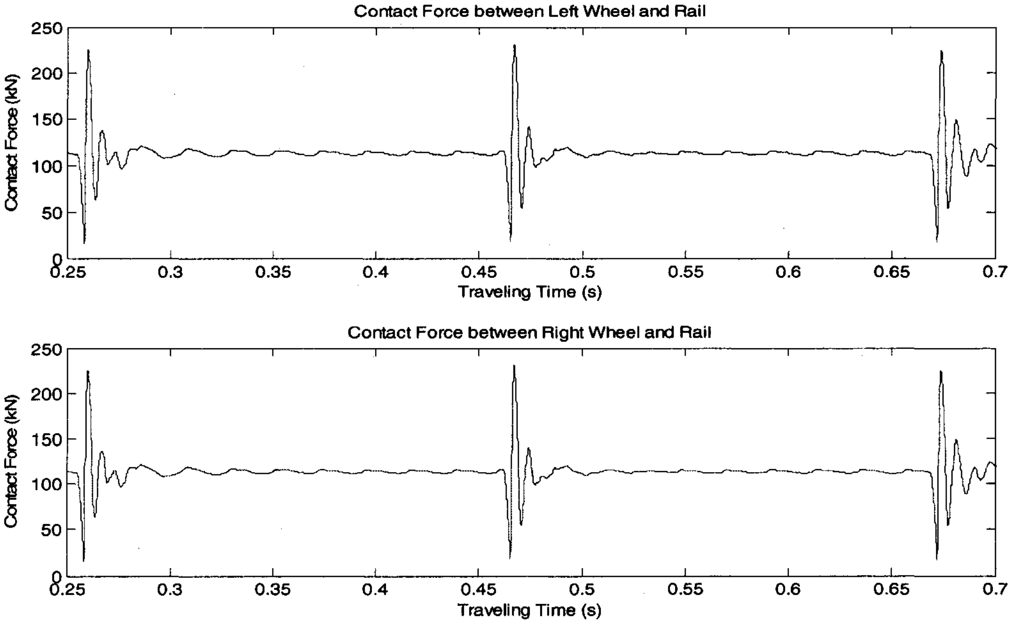

Figure 6.10: Time history of wheel-rail contact force due to 60 mm long, 0.8 mm deep flat on each wheel

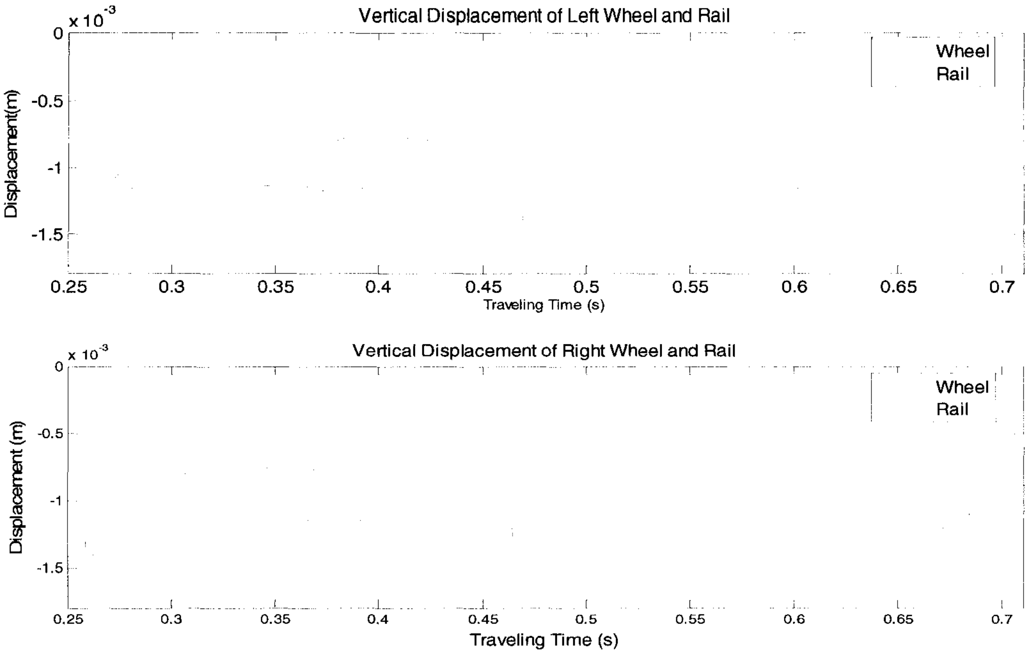

Figure 6.11: Time history of wheel-rail vertical displacements due to 60 mm long, 0.8 mm deep flat on each wheel

Simulations are next carried out for three different flat sizes in the speed range of 10 to 150 km/h. The sizes selected are: 75 mm long and 1 mm deep; 60 mm long and 0.8 mm deep; and 50 mm long and 0.5 mm deep. These sizes referred to as size 1, size 2 and size 3 are assigned to each wheel of the axle at the identical location. Simulated peak impact force for each size as speed is varied is presented in Figure 6.12. The figure also presents by dash line the results that were predicted by a single wheel having same flat size while the opposite wheel has perfect profile.

The results show a general trend that symmetric flats on each wheel lead to slightly larger impact force at low speeds when compared to those of single flat on one wheel only. The trend is reversed as the speed is increased beyond 50 km/h. the difference, however, is negligible unless the flat size is relatively large. For large flat size, the impact load due to one wheel having single flat will generate slightly larger impact than those generated by same size flat at each wheel, when speeds are moderate to high.

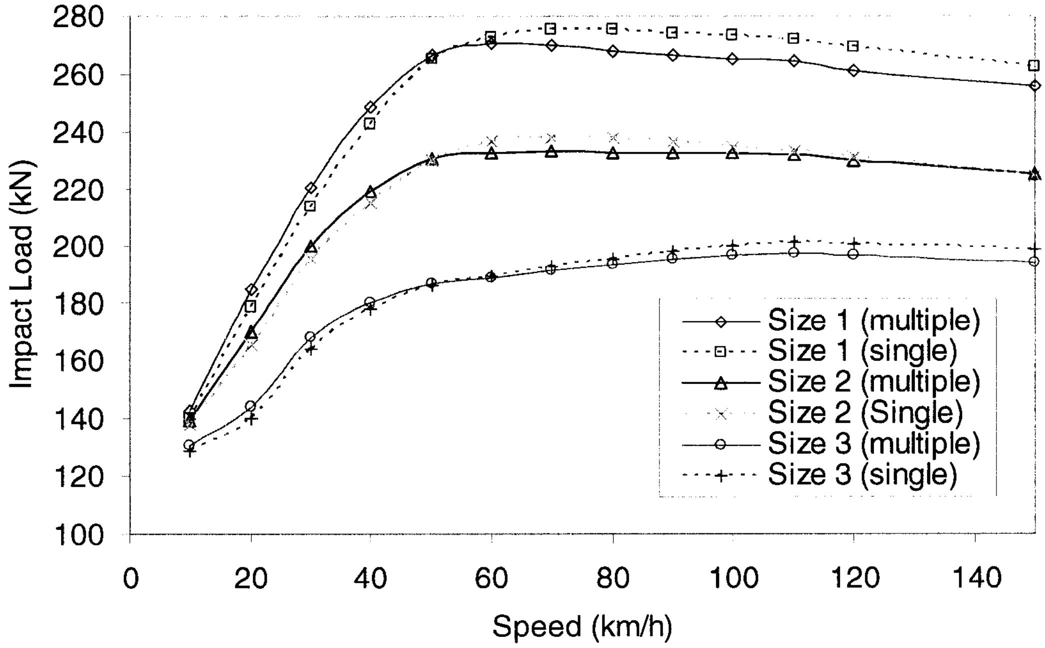

Figure 6.12: Effect of speed on impact load due to symmetric flats

The study is next extended by considering two different size flats on opposite wheels, but at the same position.

6.4.2 Two Different Size Flats on Opposite Wheels at Same Position

In practice, two flats on two opposite wheels symmetric about the wheelset centerline may be of different size. In this subsection, flats of different size are assigned to left and right wheels, the profiles of which are shown in Figure 6.13. The flat on left wheel is 60 mm long and 0.8 mm deep while the right wheel is assigned a 50 mm long and 0.5 mm deep flat. The center of each flat is at 90° from reference, as shown in Figure 6.13.

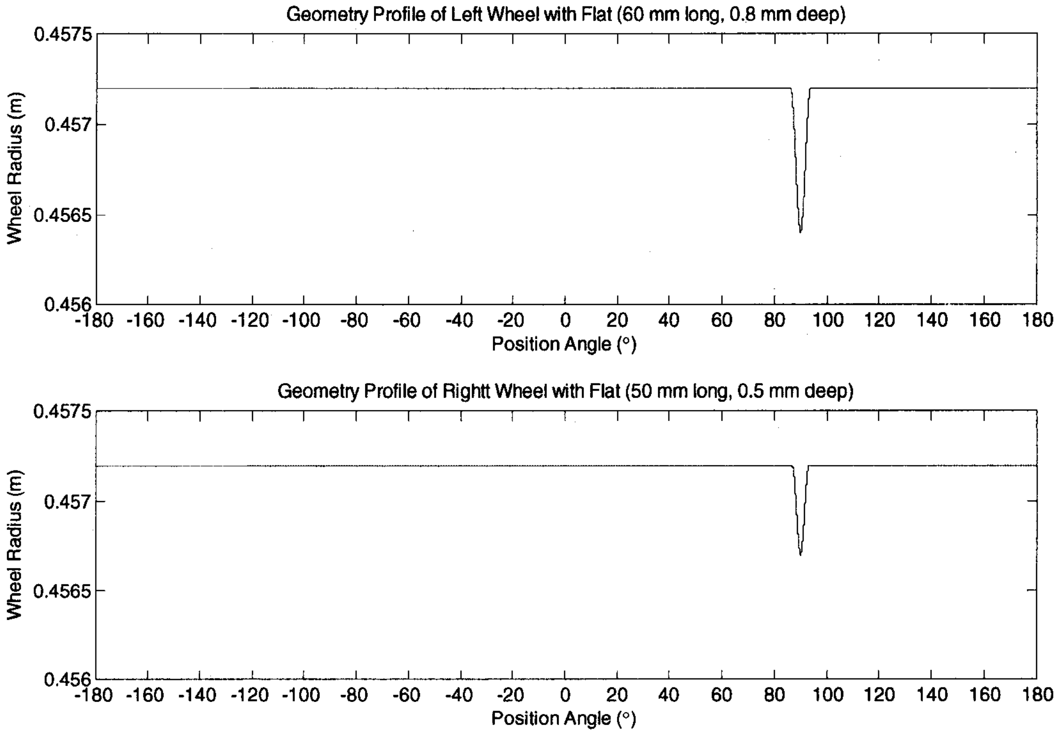
Geometry Profile of Left Wheel with Flat (60 mm long, 0.8 mm deep)

Geometry Profile of Rightt Wheel with Flat (50 mm long, 0.5 mm deep)

Figure 6.13: Profile of two opposite wheels with different size flat at same position

The time history of wheel rail contact forces between two wheels and rails at forward speed of 50 km/h is plotted in Figure 6.14. The results again show very little effect of one wheel flat on the impact force generated at the other wheel when they both have flats. The wheel with larger flat generates larger impact load than the wheel with smaller flat.

The wheel and rail peak impact loads due to these two flats and due to same size single flat in the speed range 10 ~ 150 km/h are generated as shown in Figure 6.15. The solid line presents the impact load in multiple flats case and the dash line stands for the impact load due to same size single flat. It can be seen that same as the case of two same size flats, the impact load due to a single flat is smaller than that due to multiple flats at low speed, while the single flat causes larger impact load at high speed. The difference however, is very small.

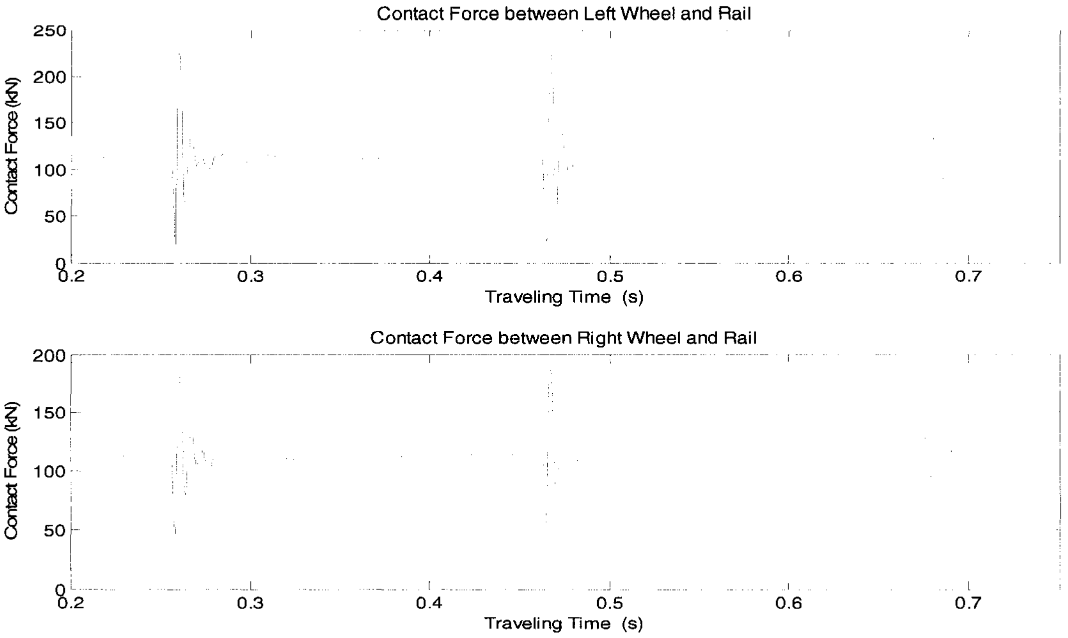

Figure 6.14: Time history of wheel-rail contact force due to different size flats on left and right wheels

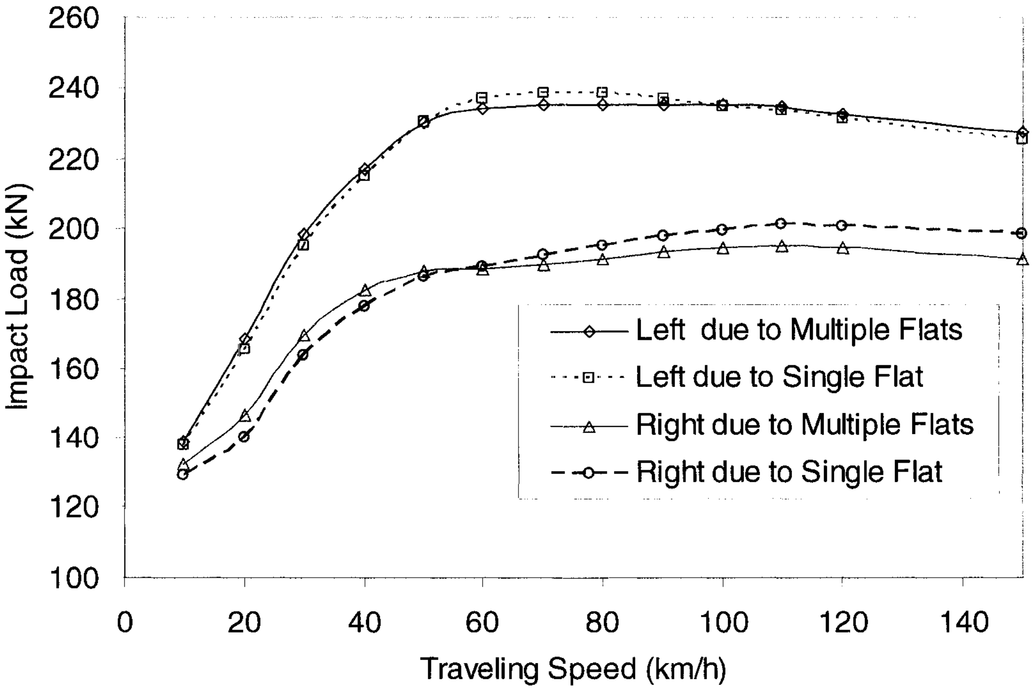

Figure 6.15: Effect of speed on impact load due to different size flat on same wheel position Note: the flat on left wheel is 60 mm long and 0.8 mm deep; the flat on right side is 50 mm long and 0.5 mm deep.

Based on the results in this subsection, it can be concluded that the impact loads in two sides of an axle are quite independent to a great extent. Regardless of same or different size symmetric flat, the impact load of each wheel can be predicted by considering a single flat of same size on one wheel.

6.4.3 Two Flats on Opposite Wheels at Asymmetric Position

Previous section examined the influence of multiple flats within a wheelset when the flats are symmetric. In order to examine the influence of asymmetry, a phase may be introduced between the flats at the left and right wheels. The wheel-rail impact load due to these asymmetrically positioning flats may be influenced by their relative position, i.e. position phase angle. The left and right wheel profiles are thus redefined as shown in Figure 6.16.

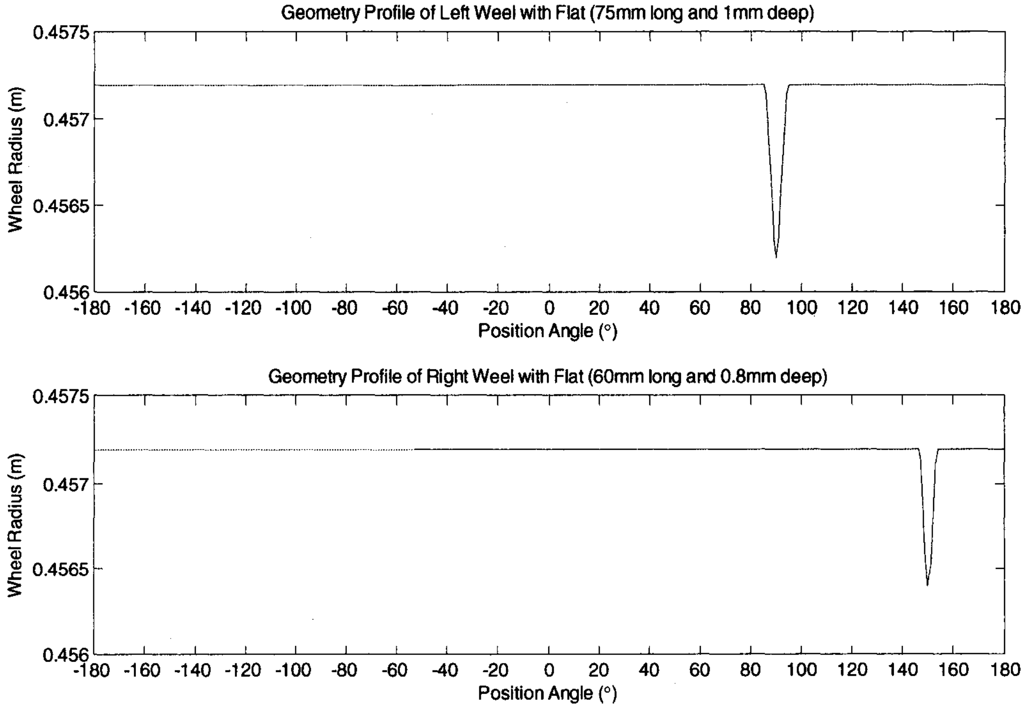

Figure 6.16: Profile of two opposite wheels with different size flat (60° out of phase)

As shown, the left wheel is assigned a 75 mm long flat which is 1 mm deep with flat center at 90° from the reference. The right wheel flat is 60 mm long and 0.8 mm deep with center at 150° from the reference. The nominal phase for this set of analysis is thus 60°.

Figure 6.17 shows the resulting contact force time history for the left and right wheel at a forward speed of 50 km/h. The results show distinct peak corresponding to their respective flats where there is no effect of cross wheel response for the phase angle at 60°.

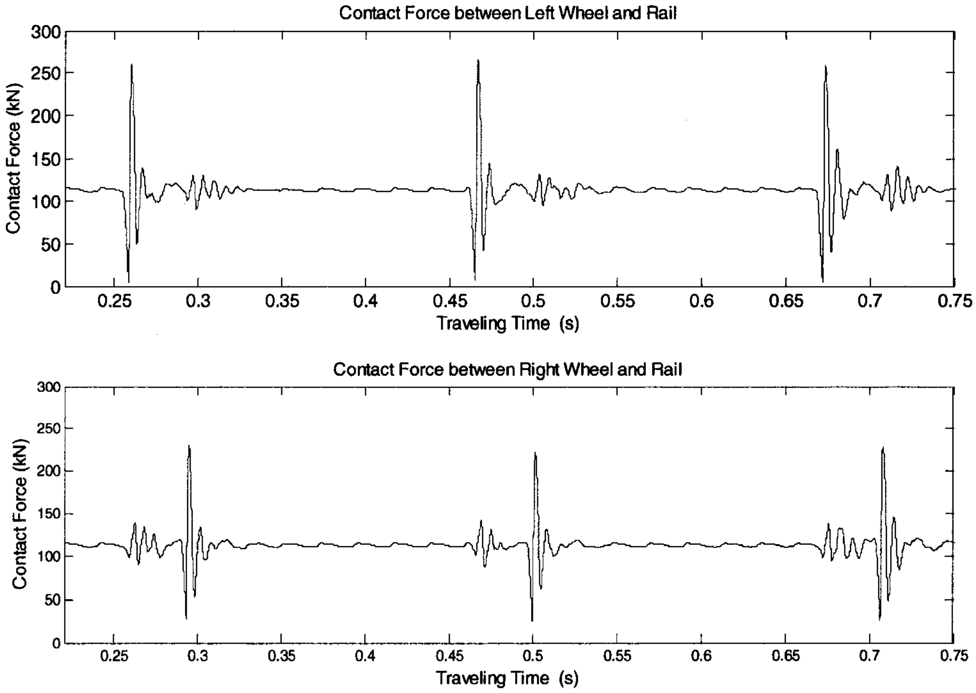

Figure 6.17: Time history of wheel rail contact force

The effect of position phase angle on impact load due to multiple flats is examined at speed of 40, 70 and 100 km/h. In this investigation, the position of the flat on left wheel at the beginning of simulation is fixed; meanwhile the phase angle for the position of the flat on right wheel is varied from 0° to 180°. The wheel-rail impact loads in the left side and right side as a function of phase angle are illustrated in Figure 6.18 and 6.19, respectively.

Figure 6.18 shows that the impact force due to the flat on the left wheel which enters contact first is unaffected by the flat on the right wheel, which enters the contact region after the phase angle. This is consistent at all phase angles except at zero when both the left and right wheel flats are in phase. For symmetric case (phase angle = 0°), the multiple flats may give slightly larger or smaller impact load than those predicted by single flat depending of speed. This is consistent with the results obtained earlier for symmetric flat cases as shown in Figure 6.15.

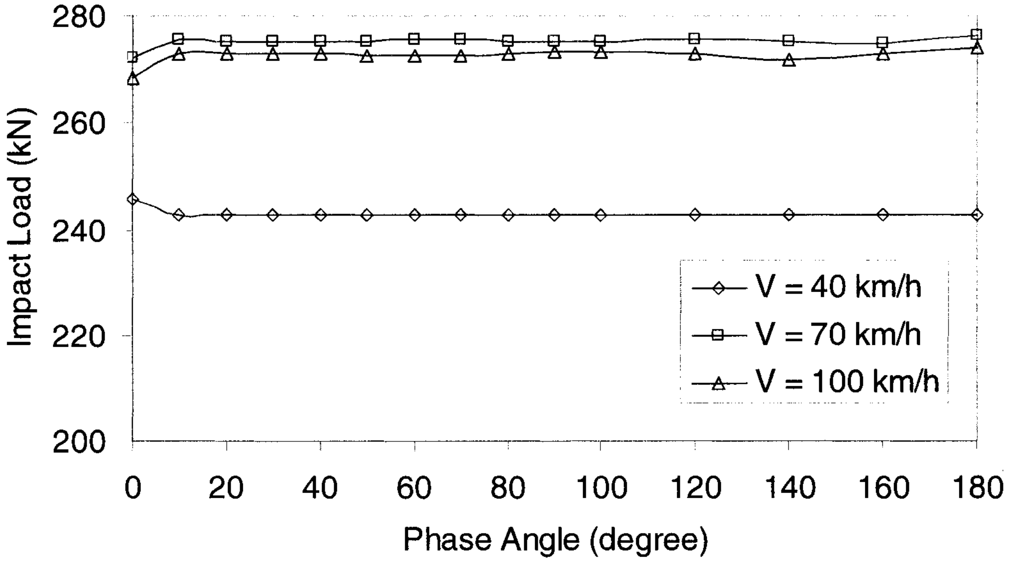

Figure 6.18: Effect of flat position phase angle on impact load of left side where the flat is 75 mm long and 1 mm deep

The flat on the right wheel of the axle enter the contact region immediately following the left wheel impact. The right wheel impact load is thus expected to be strongly influenced by the phase angle and speed. Figure 6.19 presented the peak impact force at the right wheel as a function of phase angle. At zero phase angle, again the results are consistent with those obtained before for symmetric flat of given size. The results further show significant influence of phase angle and speed on the impact load developed at the right wheel. When the speed is low, the impact load increases or decreases from that of single flat simulation for low values of phase angle. At low speed (40 km/h) as the phase angle approaches 80°, there is no further effect due to the flat on the left wheel. Similar trend to a greater extent is observed for higher speeds as shown in Figure 6.19.

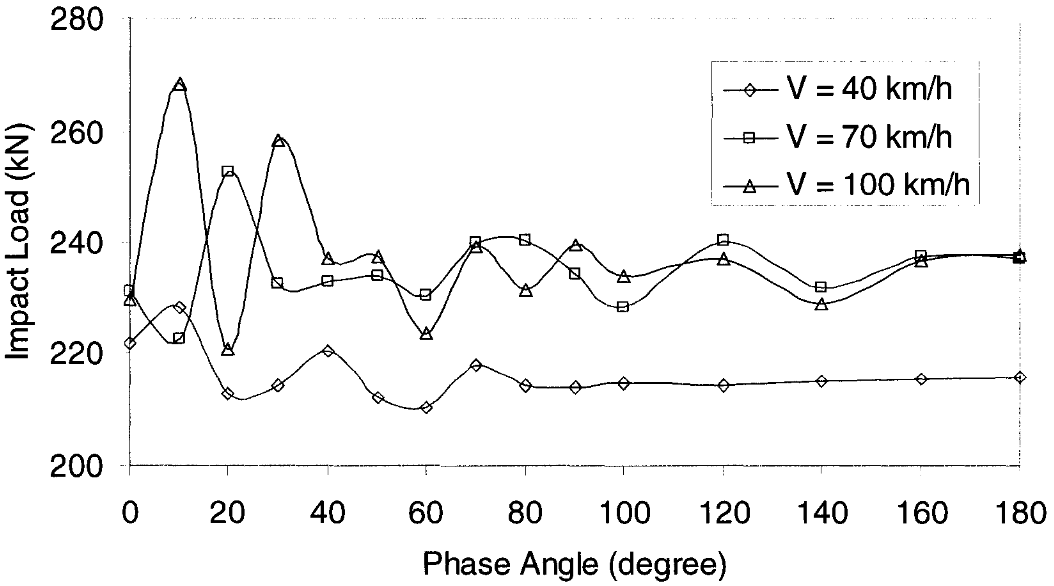

Figure 6.19: Effect of flat position phase angle on impact load of right side where the flat is 60 mm long and 0.8 mm deep

As stated earlier, this behavior is attributed to complex interaction and coupling between speed, phase angle, location of sleeper support, as well as bounce motions of the track and roll motions of the wheelset. In Chapter 5, it was shown that the flat on one side of wheel can generate motion and contact load variation at the other wheel. In the event that a flat is introduced at the other wheel while the load variation exists, the combined load or motion could be more or less than if there was no variation.

The results clearly demonstrate the possibility of significantly larger impact load corresponding to a flat if the other wheel has experienced a flat prior to it. Form the case study presented, one can say that at 100 km/h, a wheel with a single 60 mm long and 0.8 mm deep flat will generate a peak impact load of 235 kN. If the other wheel, however, also experiences a similar flat 10° prior to this flat the peak impact load may be as high as 270 kN. Multiple flats on an axle at this phase angle is not a criteria currently considered by Transport Canada or AAR for removal of defective wheels. From the results of this study, it is apparent that the length of a flat on a wheel alone is not adequate to determine the possible maximum impact load that may be created by the flat.

Further studies are recommended to study the issue of multiple flats with focus on the impact due to the second flat, regardless of other flat on the same wheel or at the cross wheel.

6.5 SUMMARY

In this study, the proposed adaptive contact model and coupled vehicle-track model are employed to study the wheel-rail impact load caused by multiple flats which are located on one wheel and two opposite wheels. The flats are modeled as haversine flat which can be described by sinusoidal function, as discussed in chapter 2. The wheel-rail impact load due to multiple flat is investigated and compared with that due to the same size single flat.

Transport Canada and AAR regulation for removal of defective wheel from service as discussed is based on the length of a single flat and adjacent flats without any regard to the existence of other flats that may be present away from each other on the same wheel or on other wheels.

The systematic study of multiple flats using roll plane vehicle model shows that regardless of the multiple flats on the same wheel or cross wheel, the impact load due to first flat is same as those can be predicted by single flat simulation study of a single wheel. The first flat is referred to the one that enters the contact region when there is no residual effect of any other flat within the axle. The second flat will thus experience residual effects of first flat if the phase is not too large. This in turn may lead to larger or smaller peak impact load by the second flat compared to the one that would be developed for single flat of same size.

Since this is due to complex interaction and coupling among speed, phase, flat size, impact position with respect to sleepers, as well as motion of the wheelset and tracks, further study is recommended to establish clear guideline that may be used by industry for maintenance and removal of wheels due to multiple flats.

CHAPTER 7

CONCLUSIONS AND RECOMMENDATIONS

7.1 GENERAL

As set out in chapter 1, the overall objective of this work is to study the wheel-rail impact load caused by wheel flats. The specific objectives include: develop an adaptive wheel-rail contact model based on the radial spring contact theory; develop a vehicle-track interaction model comprising of roll plane vehicle model and two layers 3D track mode based on Timoshenko beam theory; carry out simulations to determine wheel-rail contact forces for various scenarios in wheel defect due to wheel flat. Central finite difference method (CFDM) was applied to solve the coupled partial differential equations and ordinary differential equations. The method provides greater flexibility than those of FE commonly used for such analyses. The Steady-state dynamic interaction between wheel and rail was studied. A thorough investigation of wheel-rail impact load due to a single flat was conducted and compared with reported computational and experimental data. A comprehensive parametric study was carried out to find main factors that affect the impact load. Wheel-rail impact loads due to multiple flats was predicted and compared with that due to same size single flat. Based on the results some general and specific conclusions are drawn and a direction for future investigations is established.

7.2 HIGHTLIGHT OF CONTRIBUTION

From the review of literature, it was concluded that wheel-rail contact model and vehicle-track model are crucial to simulate the vehicle track dynamic interaction. The most common contact model used in such studies is the Hertzian nonlinear point contact theory. Such model in simulating peak contact force due to defect such as a wheel flat ignores the fact that partial and asymmetric contact is inevitable as the flat enters and leaves the contact region. It is also well known that the existing theory trends to underestimate the impact load due to a flat at low speeds while overestimate at high speeds. This study thus focused on formulating an adaptive contact model with continuous and asymmetric contact features. The results showed that even with simple vehicle and track system model, the contact force predicted by this model is more in trend with that observed in field tests. This study further showed that wheel flat on one side have influence on the wheel rail interaction of other side, and the presence of multiple flats either on one wheel or on two wheels of one wheelset may cause larger impact load under some circumstances compared with the same size single flat. Further studies are proposed on the aspect of multiple flats to identify parameters that have influence, so that constructive conclusions can be drawn for wheel removal criteria when multiple flats are present.

7.3 CONCLUSIONS

The major conclusions drawn from the present research work are summarized below:

- Adaptive wheel-rail contact model can effectively simulate the wheel-rail contact forces and can accommodate partial contact in the presence of wheel or rail defect. The developed model has been shown to provide best force response trend at all speeds when compared with available theories and field test data.

- The adaptive contact model performance is highly sensitive to the radial spring parameter (K_w) over the entire speed range. It is thus necessary to establish this parameter accurately and perhaps through experiments.
- Coupled discrete and continuous systems describe the dynamics of vehicle-track system. It was thus necessary to explore innovative ways for numerical simulations. Central finite difference method (CFDM) was proposed and applied in this investigation. It was demonstrated that CFDM is an efficient as well as importantly flexible approach for simulation of such system, where a change in the system can be incorporated easily.
- In applying CFDM for simulation, the effect of both grid length step and time step on the convergence and accuracy of solution was examined in detail. The results showed that there exists a critical time step for a given set of track parameters and grid length step used. Although a reduction in grid length results in smother rail responses, a grid length equal to half the sleeper span was found adequate for predicting peak forces.
- Simulation result for perfect wheel-rail profile (without defect) exhibits cyclic variation in the contact force as the vehicle passes over sleepers and spans. The contact force is slightly larger at the sleeper middle span than those on the sleepers. This is expected due to vertical dynamics of the vehicle and corresponding larger motion in middle span. As the speed is increased this

contact force also increases. The trend also show resonance behavior at around 50 and 100 km/h, which is also reported in other studies.

- The simulation results showed that rail length equal to 20 sleeper-spans is adequate to simulate the infinite long track at all practical speeds. The results also showed that the rail deflection under a wheel of a bogie will be affected by the other wheel load. A one-axle roll-plane vehicle model thus may slightly underestimate the rail deflection.
- Dynamic wheel-rail interaction due to a wheel flat was examined extensively and compared with other analytical work and field test data. It was shown that the proposed adaptive contact model with simplified vehicle model and track model can predict the impact force better than other existing models over a wide speed range.
- The roll plane vehicle model further exhibits that there is a distinct effect of a flat at one wheel on the contact force at the cross wheel and rail. The impact force at the defective wheel is significantly higher than at the non-defective wheel. Consequently when defective wheel is considered, the weak resonance phenomenon with speed variation exhibited for perfect wheel is no longer identifiable. This is also true for all field test data examined.
- The impact load due to a flat is strongly influenced by vehicle loading, speed and defect size. Vehicle suspension properties have little effect on the impact load, while primary suspension stiffness has noticeable influence on the bearing force. The impact position with respect to sleeper location is found to have slight effect on the peak magnitude of the impact load.

- When multiple flats are present, regardless of on the same wheel or cross wheel, there may be significant effect of first flat on the peak impact force developed due to the second flat. When two flats are present with a phase difference, the first flat is referred to the one that enters the contact region when there is no residual effect of any other flat within the axle. The second flat will thus experience residual effects of first flat if the phase is not too large. This in turn may lead to larger or smaller peak impact load by the second flat compared to the one that would be developed for single flat of same size. Based on this finding, the current rule established by Transport Canada and AAR for removal of wheel with flat may not be adequate when multiple flats are present.

7.4 RECOMMENDATION FOR FUTURE WORK

The present work provided a significant tool and insight on the problems associated with the impact load between wheel and rail due to wheel flats. In view of the potential benefits of the present study, further thorough investigations are essential for improved accuracy in predicting contact force and to establish clear guidelines for removal or maintenance of wheel to ensure safe operation. A list of further studies that can be undertaken along with recommendation for research improvement is presented in the following:

- Other approaches to determine radial spring stiffness in the proposed adaptive contact model may be developed. As discussed in the thesis, the accuracy of the predicted contact force results is largely dependent on the value of radial spring stiffness. Lab measurement of the relation between wheel rail interpenetration and applied wheel load may be the best way to establish the radial spring stiffness.

- 3D half vehicle model should be developed to improve the 2D roll plane vehicle model proposed in this study. As summarized in chapter 4, a wheel load within the pitch plane of a bogie will influence the rail deflection due to other wheel to some extent. Since the wheel base for a bogie is small, it is necessary that a 3D model of a bogie is utilized for refinement of such study.
- The study showed that the sleeper under certain loading exhibit the tendency to lift off the ballast. The track model can thus be further enhanced by including nonlinearities associated with sleepers and ballast. The lumped mass model of the sleepers may also be extended to treat them as continuous members in the 3D track system model.
- In this study, only reported data were employed to validate present simulation results. Dedicated experiment to validate the present work especially for multiple flats will enhance the study.
- As discussed in Chapter 6, the multiple flat within a wheel or cross wheel may yield larger impact force under certain condition. Further studies should address the issue that give rise to such trend so that constructive conclusions can be drawn to aid in establishing rules for service and removal of wheels in the case of multiple flats.
- The impact shear force and the bending moment of rail, and impact acceleration of vehicle track components can be studied in the future work by

the method discussed in chapter 3, to determinate the effect of wheel flats on fatigue cracks, final fracture and deterioration of vehicle track system.

REFERENCE

1. R. G. Dong, "Vertical Dynamics of Railway Vehicle-track System", Ph.D. Thesis, Concordia University 1994.

2. T. X. Wu and D.J. Thompson, "A hybrid model for the noise generation due to railway wheel flats", Journal of Sound and Vibration (2002) 251(1) 115-139.

3. R. Kovalev, *et al.*, "Railway vehicle dynamics: some aspects of wheel-rail contact modeling and optimization of running gears", Mechanics based design of structures and machines, Vol. 31, No. 3, pp.315-334, 2003.

4. S. Iwnicki, "Simulation of wheel-rail contact forces", Fatigue Fract Engnr Mater Strut 26, 887-900, 2003 Blackwell Publishing Ltd.

5. E. Deutschl, *et al.*, "Defect Detection on Rail Surfaces by a Vision based system", 2004 IEEE Intelligent Vehicles Symposium, University of Parma, Parma, Italy June 14-17, 2004.

6. D. E. Hackenberger, "Initial feasibility study to develop a wayside cracked railroad wheel detector", Proceedings of the IEEE/ASME Joint Railroad Conference, 1998, p 65-77.

7. V. Belotti, *et al.*, "Wheel-flat diagnostic tool via wavelet transform", Mechanical Systems and Signal Processing 20 (2006) 1953–1966.

8. T. Maly, *et al.*, "New development of an overall train inspection system for increased operational safety", Proceedings of the 8th International IEEE Conference on Intelligent Transportation Systems, Vienna, Austria, September 13-16, 2005.

9. A. Johansson and J. C. O. Nielsen, "Out-of-round railway wheels - Wheel-rail contact forces and track response derived from field tests and numerical simulations", Proceedings of the Institution of Mechanical Engineers, Part F: Journal of Rail and Rapid Transit, 2003, Vol: 217 Iss: 2 Page: 135.

10. J. C. O. Nielsen and A. Johansson: "Out-of-round railway wheels - a literature survey", Proceedings of the Institution of Mechanical Engineers, Part F: Journal of Rail and Rapid Transit, v214, n2, 2000, p79-91.

11. D. Stone, C. Lonsdale and S. Kalay, "Effect of wheel impact loading on shattered rims", down load from: http://www.standardsteel.com.

12. R. V. Dukkipati and R. G. Dong: "Impact of wheel flats and shells", Vehicle System Dynamics, 31 (1999), p1-22.

13. AAR, "Association of American Railroads Rule 41-Section A".

14. M. Guagliano and L. Vergani, "Experimental and numerical analysis of sub-surface cracks in railway wheels", Engineering Fracture Mechanics, v72, n2, January, 2005, p255-269.

15. J. C. O. Nielsen, *et al.*, "Train-track interaction and mechanisms of irregular wear on wheel and rail structure", Journal of Vehicle System Dynamics 2003, Vol. 40, Nos.1-3, pp3-54.

16. Y. Sato, A. Matsumoto and K. Knothe, "Review of rail corrugation studies", Wear 253 (2002), p130-139.

17. Q. Y. Liu, B. Zhang and Z. R. Zhou, "An experimental study of rail corrugation", Wear 255 (2003) p1121–1126.

18. B. Morys, "Enlargement of out-of-round wheel profiles on high speed train", Journal of Sound and Vibration, (1999) 227(5), p963-978.

19. M. Petersson," Noise-related roughness of railway wheel treads---full-scale testing of brake blocks", IMechE 2000, Proc Instn Mech Engrs, Vol 214, Part F.

20. M. Ishida , T. Moto and M. Takikawa, "The effect of lateral creepage force on rail corrugation on low rail at sharp curves", Wear 253 (2002) p172–177.

21. A. hardy and R. Jones, "Rail and wheel roughness-implications for noise mapping based on the calculation of railway noise procedure", A report produced for Defra. AEATR-PC&E-2003-002, March 2004.

22. T. Snyder and D. H. Stone, "Wheel flat and out-of round formation and growth", Proceedings of the 2003 IEEE/ASME Joint Rail Conference, April 22-24 2003, Chicago, Illinois.

23. J. Jergeus, *et al.*, “Full-scale railway wheel flat experience”. Proc Instn Mech Engrs, Journal of Mechanical Engineering science, 1999, Vol. 213, Part F.

24. Z. Q. Cai, “Modeling of rail track dynamics and wheel/rail interaction”, Ph.D. Thesis, Queen’s University 1992.

25. 2001 Transport Canada, “Railway Freight Car Inspection & Safety Rules”, Obtain from the website: http://www.tc.gc.ca/railway/Rules/TC_0-06-1.htm.

26. Chinese Railway Ministry, “Chinese Railway Freight Can Repair Requirement”.

27. British Railways Board, “Geometric Interfaces between Railway Wheelsets and Tracks”, Group Standard, Gm/TT0089, Revision A.

28. Standards Australia, “Code of practice for the defined interstate rail network”, Volume 5, Rolling stock Part 2—common, requirements, Section 3: Inspection and maintenance.

29. W. M. Zhai, “Dynamics of vehicle-track coupling (Chinese version)”, Chinese Railway Publisher, 03-1997, Beijing, China.

30. A. Tajaddini, S.F. Kalay, “Time to revise wheel-removal rules? ”, Association of American Railroads regulations”, Railway Age, Sept, 1995.

31. M. Ishida and T. Ban, “Modeling of wheel flats for track dynamics”. XXX Convegno Nazionale AIAS ---Alghero (SS), 12-15 settembre 2001.

32. K. Hou, J. Kalousek and R.G. Dong, “A dynamic model for an asymmetrical vehicle/track system”. Journal of Sound and Vibration 296 (2003) 591-604

33. T. X. Wu and D. J. Thompson, “The effects of track non-linearity on wheel/rail impact”, Proc. Instn Mech Engrs. Vol. 218, Part F: J. Rail and Rapid Transit 2004.

34. Y. Q. Sun, M. Hanasekar and D. Roach, “A three-dimensional model for the lateral and vertical dynamics of wagon-track system”. Proc. Instn Mech Engrs. Vol. 2178, Part F: J. Rail and Rapid Transit 2003.

35. W. M. Zhai, *et al.*, "Dynamic effects of vehicle on tracks in the case of raising train speeds", Proc. Instn Mech Engrs. Vol. 215, Part F, 2001.

36. Ahmed A. Shabana and Jalil R. Sany, "A Survey of Rail Vehicle Track simulations and Flexible Multibody Dynamics", Nonlinear Dynamics 26, 179–210, 2001.

37. J.C.O. Nielsen and A. Igeland, "Vertical dynamic interaction between train and track—influence of wheel and track imperfections", Journal of Sound and Vibration (1995) 187(5) 825-839.

38. X. Jin, *et al.*,"Effect of a scratch on courved rail on initiation and evolution of rail corrugation", Tribology Internation 37 (2004) 383-394.

39. B. Morys and H. Kuntze, "Simulation analysis and active compensation of the out-of-round phenomena at wheels of high speed trains", Obtained from the web site: http://www.iitb.fraunhofer.de/servlet/is/1618/florenz_121197.pdf.

40. C. Andersson and T. Abrahamsson, "Simulation of interaction between a train in general motion and a track", Vehicle dynamics, 2002 Vol.38, No.6, pp.433-455.

41. J.C.O. Nielsen, and J. Oscarsson, "Simulation of dynamic train-track interaction with state-dependent track properties", Journal of sound and vibration, 275(2004), 515-532.

42. A. Castellani, "Vibrations generated by rail vehicles: A mathematical model in the frequency domain", Vehicle system dynamics, 34 (2000), pp.153-173.

43. C. Andersson and J. Oscarsson, "Dynamic train/track interaction including state-depent track properties and flexible vehicle components", Vehicle system dynamics 33, 47-58, 1999.

44. K. Popp, I. Kaiser and H. Kruse, "System dynamics of railway vehicles and track", Archive of Applied Mechanics, 72 (2003) 949-961.

45. G. Schupp, "Simulation of railway vehicles: Necessities and applications", Mechanics based design of structures and machines, Vol. 31, No. 3, pp.297-314, 2003.

46. T. Dahlberg, "Railway track dynamics - a survey". RAILTRDY.DOC/2003-11-06/TD, Solid Mechanics/IKP, Linköping University, SE-581 83 Linköping, Sweden.

47. A. D. Kerr, "Continuously supported beams and plates subjected to moving loads---a survey", SM Archives, 1981, 6(4), 401-449.

48. F. Birmann, "Track parameters, static and dynamic, interaction between vehicle and track", Proc. I. Mech. E., Part 3F, 1965-1966, 180,73-85.

49. D. X. Tong, "Railway Track (text book, Chinese version)", Chinese Railway Publisher. 1986, Beijing, China.

50. F. W. Carter, "On the action of a locomotive driving wheel", Proceedings Royal Society London, A 112, 1926, 151–157.

51. V. K. Garg and R. V. Dukkipati, "Dynamics of Railway Vehicle System", Academic Press Canada, 1984.

52. W. Ahmed, "Lateral stability and steady –state curving behavior of railway freight car system with elasto-damper coupled wheelset", Ph.D. Thesis, Concordia University 1986.

53. J.F. Cordier, P. Fodiman, "Experimental characterization of wheel and rail surface roughness". Journal of Sound and Vibration, v 231, n 3, Mar, 2000, p 667-672

54. D. F. Cannon, *et al.*,"Rail defects: an overview". Journal of Fatigue Fracture Engineering Master Structure 26, 2003, 865-887.

55. S.G. Newton, and R.A. Clark, "An investigation into the dynamic effects on the track of wheel flats on railway vehicle". J. of Mech. Eng. Science, 1979, 21 (4), 287-297.

56. Kun Wang, "Dynamic analysis of a tracked snowplowing vehicle and assessment of ride quality", M.sc. Thesis, Concordia University 1998.

57. D. Lyon, "The calculation of track forces due to dipped rail joints, wheel flats and rail welds". Paper presented at the Second ORE Colloquium on Technical Computer Programs, May 1972.

58. S. G. Newton and R. A. Clark, "An investigation into the dynamic effects on the track of wheel flats on railway vehicles". Journal of Mechanical Engineering Science 21, 287-297. 1979

59. S. W. Weaver, *et al.*, "Vibration problems in engineering", 5th ed. Wiley, New York c1990.

60. Myung-Kwan Song, *et al.*, "A new three-dimensional finite element analysis model of high-speed train–bridge interactions". Engineering Structures 25 (2003) 1611–1626

61. X. Lei, "Dynamic analysis of the track structure of a high speed railway using finite elements". Proc Instn Mech Engrs Vol 215 Part F, 2001.

62. X. Y. Lei, L. J. Mao, "Dynamic response analyses of vehicle and track coupled system on track transition of conventional high speed railway". Journal of Sound and Vibration 271 (2004) 1133–1146.

63. H. William *et al.*, "Numerical recipes in FORTRAN". Cambridge University Press, 1992.

64. C. Bajer and R. Bogacz, "Dynamics of Y-type track". XXISYMPOSIUM---Vibrations in Physical Systems---Poznan-Kiekrz 2004.

65. A. Tajaddini and S. F. Kalay, "Time to revise wheel-removal rules?" Railway Age, Sep 1995; 169, 9; ABI/INFORM Global. p. 93.

66. M. Fermer and J. C. O Nielsen, "Vertical interaction between train and track with soft and stiff railpads---full scale experiments and theory". Proc. Instn Mech.Engrs, Part F: J. Rail and Rapid Transit, 1995, 209(F1), 39~47.

67. R. V. Dukkipati and R.G. Dong, "Idealized steady state interaction between railway vehicle and track". Proc. Instn Mech Engrs Vol 213 Part F, IMechE 1999.

68. M. K. Song, *et al.*, "A new three-dimensional finite element analysis model of high-speed train–bridge interactions. Engineering Structures 25 (2003) 1611–1626.